UC Santa Cruz
UC Santa Cruz Electronic Theses and Dissertations

Title

Water Ice Clouds on Mars: Exploring Processes Through Modeling and Laboratory Work

Permalink

https://escholarship.org/uc/item/8tf8r60q

Author

Santiago-Materese, Delia Liza

Publication Date

2016

Copyright Information

Peer reviewed|Thesis/dissertation

UNIVERSITY OF CALIFORNIA

SANTA CRUZ

WATER ICE CLOUDS ON MARS: EXPLORING PROCESSES THROUGH MODELING AND LABORATORY WORK

A dissertation submitted in partial satisfaction of the
requirements for the degree of

DOCTOR OF PHILOSOPHY

in

EARTH SCIENCES

by

Delia Liza Santiago-Materese

December 2016

The Dissertation of Delia Liza Santiago-Materese
is approved:

Professor Patrick Chuang, Chair

Professor Francis Nimmo

Misha Kreslavsky, Ph.D.

Anthony Colaprete, Ph.D.

Dean Tyrus Miller
Vice Provost and Dean of Graduate Studies

Contents

List of Figures

vii

List of Tables

Abstract

WATER ICE CLOUDS ON MARS: EXPLORING PROCESSES THROUGH
MODELING AND LABORATORY WORK

by

Delia Liza Santiago-Materese

Water ice clouds on Mars are an important component of the hydrologic cycle as well
as the overall climate system of the planet. The goal of this research is to better under-
stand water ice cloud formation and behavior on Mars. We use modeling and laboratory
experiments to explore different processes related to water ice cloud formation and evo-
lution.

The first goal of this work is to examine how well the Martian water cycle is simulated
by the NASA Ames Mars General Circulation Model. The simulation predicts atmo-
spheric water vapor amounts approximately half of those observed, globally. We iden-
tify water ice clouds as being a major contributor to this discrepancy. The model closely
reproduces the convective aphelion cloud belt at the equator, but deviates substantially
from observations over the North Polar Cap region. Modifying the nucleation scheme
within the cloud microphysical model brings model results closer to observations and
affects the surface radiative balance, which affects the annual cycle of sublimation and
deposition of water ice at the residual North Polar Cap. The most realistic global water
vapor and cloud patterns come from limiting the nucleation rate of particles at the poles.
Our simulations show that the North Polar Cap region exhibits atmospheric dynamics
where stratiform clouds form. We hypothesize that the modified nucleation scheme
compensates for biases in the radiative properties of the stratiform clouds expected
over the North Polar Cap. More broadly, this study illustrates the strong sensitivity of
the Martian global water cycle to clouds over the North Polar Cap region.

The second goal of this work is to assess the ability of various salts to serve as water
ice cloud condensation nuclei under Martian conditions. We use a vacuum chamber

to simulate the cold, lower pressure atmospheric conditions on Mars and find the critical saturation ratios at which the substrates nucleate water ice. We find no significant difference between sodium chloride nucleation and that of the control of a bare silicon wafer. In contrast, sodium perchlorate nucleates at significantly lower saturation ratios than the control, suggesting that some atmospheric salts could serve as effective cloud condensation nuclei on Mars. All substrates examined demonstrate an exponential temperature-dependence for the critical saturation ratio, indicating that at colder temperatures, nucleation requires increasingly higher saturation ratios. Our results suggest that airborne sodium perchlorate may enable water ice cloud formation at partial pressures lower than would otherwise be required in its absence. For example, at 155 K, sodium perchlorate could nucleate water ice at a partial pressure 40 percent lower than other cloud substrates.

The third goal of this work is understand the impacts of temperature-dependent optical parameters on the radiative effects of water ice clouds on Mars. The optical properties of water ice vary with temperature, however, past Mars climate modeling have used optical properties based on water ice refractive indices relevant to Earth's atmospheric temperatures. In this chapter we use water ice refractive indices at temperatures relevant to the Martian atmosphere with Mie scattering code to provide input into the NASA Ames Mars General Circulation Model. We compare the instantaneous effects of using these optical parameters, versus values that have been traditionally used, on daytime and nighttime radiative fluxes. We find that the updated optical properties amplify existing radiative flux trends over most of the planet, which would lead to increased energy fluxes at the North Polar cap during the Northern hemisphere summer as well as increased atmospheric warming at equatorial clouds. Atmospheric warming is increased at night with more relevant optical parameters and could result in temperatures differences of several Kelvin a day.

For Christopher and Ruby.

Thank you for being my light.

Acknowledgments

This thesis has been a long journey, and I am grateful for my advisor, Patrick, for being there the whole way, first as a committee member and for the past few years as my primary academic advisor. I appreciate your helpful and detailed scientific guidance, your pragmatism mixed with enthusiasm, and for the fact that you were dedicated to helping me succeed, no matter how I became your student. I am extremely grateful to my unofficial NASA advisor, Laura Iraci, for hours of scientific conversation, guidance in the lab, and being supportive of my work even when faced with her own challenges. I am grateful for both Patrick and Laura of being supportive of my venture into parenthood while in the final leg of graduate school.

Thank you to my committee members who gave their time to consider my work. Thank you to Anthony Colaprete for your guidance with modeling and always delving into the messy details with gusto. I am also grateful for your support in me returning to my graduate studies. Thank you to Francis Nimmo for sharing your breadth of planetary knowledge while on my committee and your feedback on my work. Finally, thank you to Misha Kreslavsky for your thoughtful and detailed feedback on my climate modeling work, and your dedication towards helping me make my work better. I also want to thank Erik Asphaug, my former advisor, for supporting my return to school and offering thought-provoking questions and guidance related to my science, graduate experience, and career in general.

Much gratitude goes to the members of Laura Iraci's lab before me. In particular, Bruce Phebus and Brendan Mar were of particular help when developing my experimental procedures. Thank you to earlier members who provided documentation and equipment development. I am grateful to Emmett Quigley, Lisa Hildebrand, and Jim Eilers for their technical assistance in the lab, which included updating equipment, fixing broken things when I was freaking out, and providing excellent company. Many thanks for the NASA Ames Mars Climate Modeling group. Specifically, many thanks to Melinda Kahre for sharing her expansive knowledge about the model and Mars in general, Jeffrey Hollingsworth for support as group lead and Branch Chief, Amanda

Brecht for hours of conversation about work and life while walking around the Ames perimeter, and finally Jim Schaeffer, whose patience, kindness, and endless helpfulness will be remembered always; you are greatly missed, Jim.

Special acknowledgements are due to those who have contributed substantially to the development of my thesis chapters, as follows. Chapter 2 was written closely with Patrick Chuang, with modeling advised by Anthony Colaprete, with substantial edits on the manuscript by Misha Kreslavsky. The NASA Ames Mars Climate Modeling group, with special thanks for Jim Schaeffer, greatly supported this work. Chapter 3 was co-authored by Laura Iraci, Patrick Chuang, and Matthew Clapham. Laura provided overall scientific and laboratory guidance, Patrick provided scientific guidance and manuscript feedback, and Matthew Clapham provided statistical analyses of the results. Thanks also to Sanaz Vahidinia and Cristina Dalle Ore for helpful conversations in interpreting the data. Chapter 4 was inspired by discussions with Patrick and Laura and enabled by support from Melinda Kahre. We thank Julie Dequaire for her computer code which enabled making new cloud optical properties use Mie scattering code.

In addition to everyone that has supported me in making this thesis be realized, I am ever grateful to many good friends, at school, work, and beyond who have supported me in this journey. Thank you to my parents for always believing in me, even when I didn't. Thank you to my original graduate cohort, my new 'older student' cohort of Heidi Stauffer, the original Paleoclimate lab, the Planetary group at UCSC, cloud lab mates Dione Rossiter and Mikael Witte, Jennifer Fish, NASA 'cubie' Kim Mjaseth, Hartree-Fock, Carol Johnson, angel Barbara Dahl, and many lifelong friends who kept me sane. And last but not least, thank you to all the people who came before me to pave the way.

Chapter 1

Introduction

1.1 Background

As one of Earth's closest neighbors, Mars has long been an object of human fascination and wonder. When 19th century astronomers observed the surface of Mars, they saw features that were originally thought to be canals or other unnatural structures. Years later the first orbiter sent to Mars, Mariner 9, returned data that decisively countered that perspective [*Sagan and Fox*, 1975]. Mars differs from Earth in a myriad of ways including the current lack of plate tectonics, thin atmosphere, minimal magnetosphere, and no discernible lifeforms. However, Mars does show evidence of fluvial features on the surface and an active climate system. On Mars, two major volatiles change phase and are subject to exchange between the surface and atmosphere: carbon dioxide and water. Clouds on Mars were first identified as being composed of water ice the 1970s (first observations described in *Curran et al.* [1973]). We have long understood that water clouds on Earth are a key component of the planet's climate, and affect water transport, air quality, and the planetary energy budget. It is believed that clouds on Mars also play a key role in the climate and this work will explore that topic.

The goal of this dissertation is to further our understanding water ice clouds on Mars, including what influences their formation and how they influence climate. Specif-

ically, this work examines factors that affect cloud formation on a global scale, cloud nucleation events as being substrate-dependent, and the optical properties of clouds as they change with temperature. This research was accomplished through a combination of theoretical and experimental effort including use of a Mars Global Climate Model (MGCM), a 1-dimensional Mars climate model, and laboratory experiments involving a high-vacuum chamber.

1.1.1 Mars climate

Present-day Mars is cold and dry relative to Earth. Unlike Earth, Mars has two volatiles that change between solid and gas phases (and possibly a liquid phase): carbon dioxide and water. The triple point of carbon dioxide is 5.2 bar at 216.55 K [*Angus et al.*, 1976], and the triple point of water is 6.1 mbar at 273.15 K [*Guildner et al.*, 1976]. The surface pressure varies just below 7 mbar to slightly over 10 mbar depending on the location and time of year [*Leovy et al.*, 1985], with variations due to the fact that the major atmospheric constituent, carbon dioxide, condenses out of the atmosphere, in addition to orographic and dynamical effects [*Hourdin et al.*, 1993]. The pressure cycle of Mars is seen in Fig. 1.1. Carbon dioxide comprises 96% of the atmosphere by mass [*Mahaffy et al.*, 2013] and condenses out of the atmosphere both on the surface as well as in the form of clouds. Water also condenses out at both the surface and in clouds on Mars, with mixed water-carbon dioxide clouds believed to exist [*Gooding*, 1986]. Water is far less abundant on Mars compared to Earth, and comprises less than 1% of the atmosphere by mass [*Owen et al.*, 1977].

The most dramatic example of Martian volatile activity at the surface can be observed at the poles. Early evidence of seasonal variation at the poles was detected by famed astronomer William Herschel. Subsequent ground based observations [*Iwasaki et al.*, 1979] followed later by Hubble images provided a much more detailed understanding of the seasonal variations in the Mars polar cap [*James et al.*, 1994]. In 2008, the Phoenix lander's robotic arm excavated soil to reveal water ice that sublimed within days [*Smith*, 2009], demonstrating that water ice was present in the regolith at lower
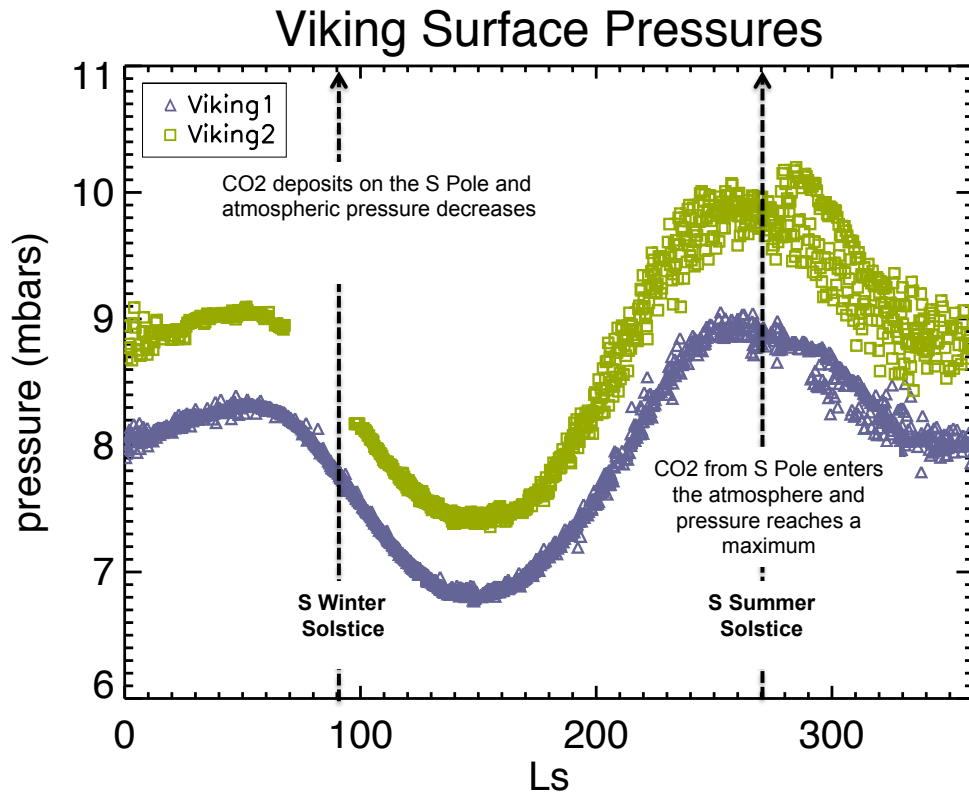
Figure 1.1: The seasonal cycle of surface pressure as measured by the Viking landers. The values are daily average pressure values from the duration of the mission [*Leovy et al.*, 1985].

latitudes. This finding was of particular interest because of the ongoing search for life on Mars. Recently, geomorphology from volatile sources has been observed, with both water and carbon dioxide being attributed to causing fluvial-like features such as recurring slope lineae and debris flows [*Ojha et al.*, 2015; *Pilorget and Forget*, 2015].

The evolution of climate, and water, on Mars is best understood through the context of Martian geologic history, which is divided into three major epochs that are determined by crater counting [*Hartmann and Neukum*, 2001]. The current epoch, the Amazonian, began ~2.9-3.3 Gyr and is characterized by having low impact activity and a climate similar to that of today. The previous epoch, the Hesperian, lasted from ~3.0-3.7 Gyr and is characterized by significant volcanic activity, with fluvial activity dominated by outflow channels. The climate was likely similar today but possibly punctuated by extreme climatic activity [*Carr and Head*, 2010]. The Noachian occurred prior to 3.5-3.7 Gyr, until Mars' formation ~4.65 Gyr, with a pre-Noachian period sometimes distinguished as occurring from the formation of the planet until the formation of Hellas ~3.8-4.1 Gyr and as a time when the planet still had a magnetic field [*Carr and Head*, 2010]. The Noachian is when many of the fluvial features, such as valley networks, canyons, and other erosional features, formed, and when impacts were still a common occurrence for the planet. Some hypothesize that fluvial features are evidence that an early, Noachian Mars was warm and wet, with Earth-analog providing a driving force for many of the theories about Noachian features on Mars as reviewed in *Chapman* [2007].

The history of the Martian climate may be captured in the layered deposits at both poles of the planet. These deposits capture the orbital evolution patterns of Mars with alternating volatile and dust layers that follow orbital climate forcing [*Laskar et al.*, 2002]. The inventory of water in the polar caps may even have been largely in the atmosphere or on the surface at low latitudes (and not at the poles) during certain points in history [*Jakosky and Carr*, 1985; *Milkovich and Head*, 2005]. The poles of Mars have been shown to be critical to understanding the climate of Mars, particularly when it comes to water.
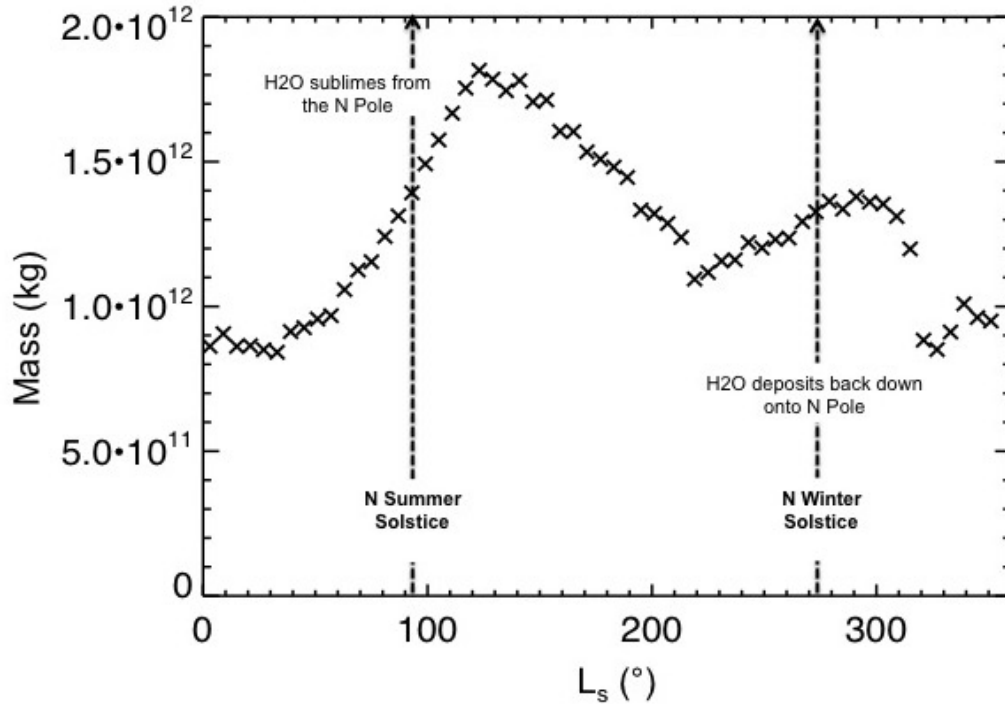
Figure 1.2: The annual, seasonal cycle of the global sum of water vapor mass in the Martian atmosphere. Measurements taken at 2 PM local time with the MGS TES instrument [*Smith*, 2002, 2004, 2008].

1.1.2 Mars water cycle

The global atmospheric water budget is primarily driven by sublimation from the North Polar Cap during aphelion, which is the Northern hemisphere summer solstice, as seen in Fig. 1.2. Both the North [*Kieffer and Titus*, 2001] and South [*Bibring et al.*, 2004] poles have perennial water ice at the surface. Peak levels of global atmospheric mass are observed for the summer solstices for both Northern and Southern hemispheres, with the larger water ice cap at the North Pole dominating the seasonal atmospheric water cycle. In the Northern hemisphere spring and summer, water ice clouds are seen at the poles and at the equator, with the equatorial aphelion cloud belt containing water ice particles with radii of 3-4 μm and the polar hood cloud particles

5

with radii reaching about 1-2 µm [*Clancy et al.*, 2003]. Water ice cloud precipitation was only recently directly observed on Mars [*Whiteway et al.*, 2009]. Particle sizes have been extracted from these observations and they are thought to be large enough to be able to hit the ground. However, the nature of these particles (size, structure, phase, optical properties, etc.) is not yet fully understood and is an ongoing area for investigation.

Water ice clouds affect the present Martian climate in a variety of ways. While the clouds may scavenge dust, they largely affect dust layers via strengthened circulation that lofts dust upwards [*Navarro et al.*, 2014; *Kahre et al.*, 2015]. On a local level, dust can be redistributed to lower altitudes by water ice clouds, leading to radiative warming from the dust closer to the surface [*Colaprete and Toon*, 2000]. Dust feedbacks also enhance polar warming from water ice clouds [*Kahre et al.*, 2015]. Water ice clouds also warm the atmosphere in the tropics [*Wilson et al.*, 2008] and drive circulation there [*Heavens et al.*, 2010, 2011]. On a global level, warming from water ice clouds can result in large scale circulatory changes [*Madeleine et al.*, 2012].

Water ice clouds are also believed to have a profound effect on the long-term water cycle of Mars. The "Clancy effect" [*Clancy et al.*, 1996] suggests that water ice clouds allow for water to migrate to the north pole under the current orbital configuration. This is due to the fact that aphelion summer hemisphere, currently the Northern hemisphere, facilitates cloud formation at low altitudes, which in turn reduces meridional water transport towards the Southern hemisphere. Modeling confirms the role of clouds in this theory [*Navarro et al.*, 2014].

1.1.3   Water physical processes on Mars

Processes relevant to water ice clouds include sublimation/ deposition, efflorescence/ deliquescence, and adsorption. At warmer temperatures on Earth, condensation/ evaporation also play a role. Although these are not all probed by this work, they may contribute to water ice cloud formation and evolution on Mars and are thus discussed here.

Deliquescence occurs when a crystalline solid takes up solvent vapor from the atmosphere to become a solution. Following deliquescence, the water and salt can remain in the liquid phase even beyond the original temperature of deliquescence. In contrast to deliquescence, efflorescence is a process in which a salt precipitates out of the liquid phase as the partial pressure of the solvent liquid is decreased. Overall, the inclusion of salts can have significant effects on the thermodynamic properties of water when in solution. It has been suggested that salt may even allow liquid water to exist on the surface of Mars under conditions where it would otherwise be frozen or sublime [*Chevrier et al.*, 2009].

Adsorption is thought to be an important process to consider on short, cloud microphysical time scales, but less important in terms of long-term surface processes such as movement of water between the subsurface regolith and the atmosphere [*Schorghofer and Aharonson*, 2005]. For adsorption the specific surface area is what determines the adsorption behavior, not the material [*Zent and Quinn*, 1997]. It is not clear if we can differentiate adsorption processes, but we should be able to observe a distinction of the following processes: deliquescence, adsorption, and possible ice nucleation.

Another potential process of interest is the formation of thin liquid films (modeling by *Boxe et al.* [2012], surface conditions). The liquid water comes from adsorbed water vapor and would be several molecules deep (with film thickness on a nanometer scale). It should, however, be noted that this work was not completed under conditions specifically relevant to the Martian atmosphere, and therefore may not be fully applicable.

Finally, the cooling rate is an extremely important factor for ice nucleation, as the critical saturation for the onset of nucleation is lower when cooling is slow [*Cziczo et al.*, 2013]. Slow cooling may also lead to perchlorate glasses instead of crystals [*Toner et al.*, 2014]. Differences in the water structure could lead to large differences in cloud optical properties and affect how surface water deposits reflect sunlight.

1.2 Past (and ongoing) studies of Mars

1.2.1 Observations of Mars

Although a significant portion of the scientific body of knowledge related to the Martian climate has emerged from theoretical models and laboratory experiments, they are fundamentally grounded in observations of Mars itself. Ground-based telescopes have been observing Mars since the 1800s. The modern era of Mars planetary exploration began in the 1960s, with successful orbiting missions established in 1971 by a successful launch of Mariner 9 by NASA. The following discussion of missions to Mars is not exhaustive but highlights those that contributed to science most related to this work.

The Mariner 9 Orbiter mission [*Steinbacher*, 1972] from 1971-1972 was launched by NASA and included the Infrared Interferometer Spectrometer (IRIS), which provided the first observations of dust storms on Mars. This mission proved to be instrumental to the understanding of the importance of dust to the Martian climate [*Hanel et al.*, 1972]. NASA's Viking orbiters and landers [*Soffen and Young*, 1972] surveyed the planet from the late 1970's to the early 1980's. The Viking Orbiters 1 and 2, which were based on the Mariner 9 spacecraft, mapped water vapor and other trace gases on Mars via the Mars Atmospheric Water Detector (MAWD) and measured atmospheric temperatures as well as water ice cloud and dust optical depths using the Infrared Radiometers for Thermal Mapping (IRTM). The Viking Landers 1 and 2 provided pressure profiles, wind and temperature data, as well as images from the surfaces at their landing sites in Western Chryse Planitia and Utopia Planitia, respectively.

Two decades after the last successful mission to Mars, NASA returned to the planet with an orbiter and rover in quick succession. The Mars Global Surveyor (MGS) [*Albee et al.*, 1998], an orbiter active 1997-2006, provided a wealth of information from the Thermal Emission Spectrometer (TES), which elucidated global profiles of atmospheric temperatures, water vapor abundance, and dust and water ice cloud optical depths. Additional atmospheric temperature profiles were obtained with the Radio

Science Subsystem. Dust and water ice optical depth values were also captured with the Mars Orbital Camera (MOC), which also captured planetary surface images and most famously the 2001 dust storm. The Mars Pathfinder rover [*Golombek*, 1997], active in 1996-1997, measured temperatures, wind speeds, and captured images from the surface.

Less than a decade after the successful MGS and Mars Pathfinder missions, a plethora of missions to Mars began, with several continuing to this day. NASA's Mars Odyssey orbiter [*Saunders et al.*, 2004], whose mission began in 2001 and continues today, has collected additional temperature and mineralogy data via the Thermal Emission Imaging System (THEMIS). The Mars Express Orbiter [*Chicarro et al.*, 2004], operated by the European Space Agency, began its mission in 2003 and included payloads OMEGA, PFS (Planetary Fourier Spectrometer), and SPICAM (Ultraviolet and Infrared Atmospheric Spectrometer).

The Mars Exploration Rovers Spirit [*Arvidson et al.*, 2006] and Opportunity [*Squyres et al.*, 2006], from NASA, began their mission in 2004. Contact with Spirit was lost in 2011, while Opportunity continues to explore the Martian surface. In addition to providing a wealth of surface images, the rovers took spectroscopic measurements, used an instrument called the rock abrasion tool to sample the the interiors of surface rocks so their compositions could be analyzed, and took atmospheric measurements with cameras and a mini-TES instrument that complements MGS TES measurements [*Lemmon et al.*, 2004].

NASA's Mars Reconnaissance Orbiter [*Zurek and Smrekar*, 2007] began orbiting Mars in 2006 and continues observing Mars to this day. The Compact Reconnaissance Imaging Spectrometer for Mars (CRISM) payload observes in the visible and near-infrared wavelengths, allowing for mineralogical analyses of the surface. The Mars Climate Sounder (MCS) payload takes measurements in the visible and infrared wavelengths to extract profiles of temperature, pressure, water vapor, abundance, and dust optical depth. The MARCI (Mars Color Imager) payload takes images of the surface and relates information on water ice optical depth. Mars Global Surveyor,

Mars Odyssey, and Mars Reconnaissance Orbiter provide complimentary and continuous spectroscopic measurements of the planet over time.

The most recent surface mission to Mars is the Curiosity rover, also known as the Mars Science Laboratory (MSL) [*Grotzinger et al.*, 2012], which landed in Gale Crater in 2012. Curiosity has numerous cameras for detailed imaging and is equipped with various instruments to observe the atmosphere as well as collect and analyze samples from the surface. Finally, the Mars Atmosphere and Volatile EvolutioN Mission (MAVEN) [*Jakosky et al.*, 2015] inserted into Mars' atmosphere in 2014 and continues with its mission of observing the upper atmosphere to this day, with the goal of understanding the atmosphere's evolution over time.

1.2.2   Mars climate modeling

With an abundance of data acquired through observations of and missions to the red planet, many important questions remain about the Martian climate, both past and present. To address these questions, models which incorporate these data and draw upon concepts established from terrestrial climate modeling, have been developed to simulate the Martian climate . Models of the Martian climate can help to understand water ice cloud processes that are not currently directly observable. 1-dimensional models have been used to establish dust distribution and radiative effects in water ice clouds for comparison to Viking and Pathfinder data [*Colaprete and Toon*, 2000; *Montmessin et al.*, 2002]. 3-dimensional models have explored microphysics, radiative effects, and dynamical implications of water ice clouds (for example, *Haberle et al.* [1993]; *Kahre et al.* [2008]; *Nelli et al.* [2009, 2010]; *Haberle* [2013]; *Navarro et al.* [2014]; *Kahre et al.* [2015]) in combination with mission data.

This work uses the NASA Ames Mars General Circulation Model (MGCM). An important aspect of the cloud microphysical scheme used in this work is the radiative transfer scheme, with relevant processes shown in Fig. 1.3. For each level of the atmosphere, the radiative properties of the clouds are calculated in both visible and infrared wavelengths: extinction efficiency, single scattering efficiency, and an asymmetry pa-
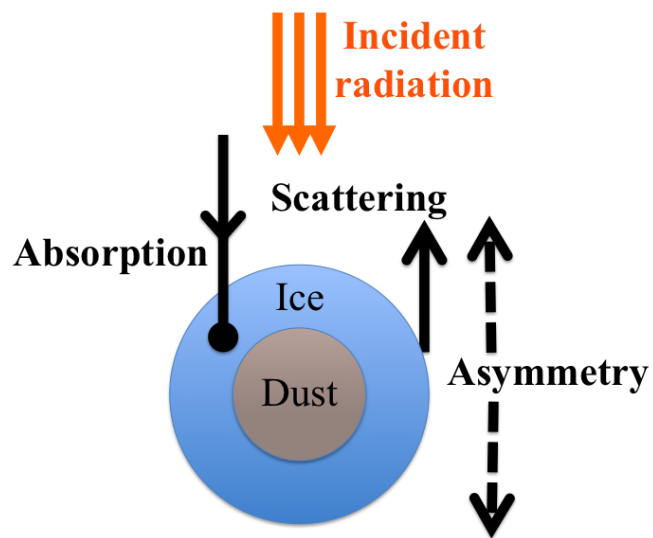
Figure 1.3: Radiative processes that are represented in the model. Values for these optical properties are a function of the ice-to-dust ratio, the effective radius of the particle for a given layer in the model, and wavelengths of light. Asymmetry determines the amount of single scattering that is upward or downwards.

Visible wavelengths

	Wavelength interval (microns)		Wavenumber interval (cm-1)	
bin # (model)	start	end	start	end
1	3.24	4.50	2,222	3,086
2	2.48	3.24	3,086	4,032
3	1.86	2.48	4,032	5,376
4	1.31	1.86	5,376	7,634
5	0.80	1.31	7,634	12,500
6	0.40	0.80	12,500	25,000
7	0.24	0.40	25,000	41,667

Infrared wavelengths

	Wavelength interval (microns)		Wavenumber (cm-1)	
bin # (model)	start	end	start	end
1	60.0	1000	10	167
2	24.0	60.0	167	417
3	12.0	24.0	417	833
4	8.0	12.0	833	1,250
5	4.5	8.0	1,250	2,222

Table 1.1: Spectral intervals in the MGCM for radiation calculations

rameter (for a total of six calculated properties at each layer). The extinction efficiency represents absorption of light by the particle, the scattering efficiency represents reflection of light, and asymmetry reflects what fraction of light is scattered upward or downward. The values of the three radiative properties are each a function of the core-to-mantle (i.e. dust-to-water ice) ratio, the effective radius of the total particle, and the wavelength of interest. The specific wavelengths over which the radiative properties of the water ice clouds are calculated are in Table 1.1 .
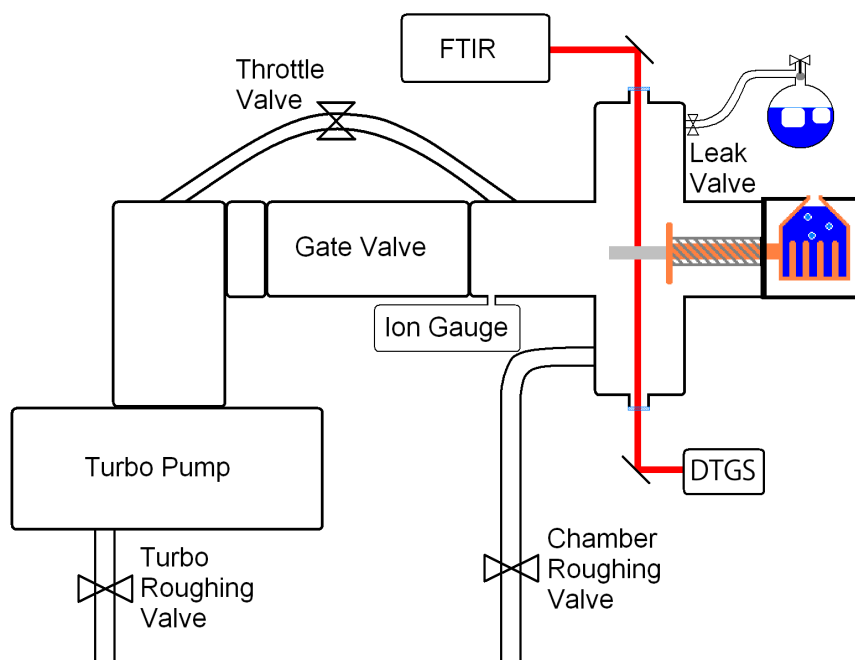
Figure 1.4: Diagram of laboratory equipment used in experiments. *FTIR* is the Fourier Transform Infrared Spectrometer and *DTGS* is the deuterated triglycine sulfate detector.

1.2.3 Experimental studies of Mars

Laboratory experiments have studied volatile behavior at surface and atmospheric conditions on Mars. This work continues Mars atmospheric studies by *Iraci et al.* [2010] and *Phebus et al.* [2011], using the laboratory set-up outlined in Fig. 1.4. This configuration uses a vacuum chamber, which reduces pressures to the low 10^{-8} Torr, and a liquid nitrogen dewar that cools a copper rod that holds the sample, shown in Fig. 1.5. A silicon wafer is mounted onto the copper and heaters control the temperature near the wafer.

Past Mars cloud laboratory work has focused on silicon and a variety of mineral analogs that may represent lofted dust on the planet. Martian mineral analogs that have been studied for Mars cloud formation in the past include JSC Mars-1, Mojave Mars Simulant (MMS), and Arizona Test Dust (ATD) [*Iraci et al.*, 2010; *Phebus et al.*, 2011;
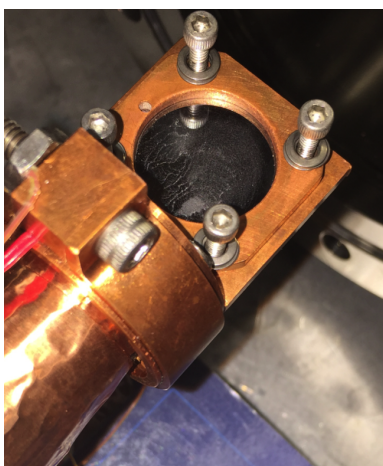
Figure 1.5: Silicon wafer on copper mount that is used in these laboratory experiments. Wafer has a dust substrate applied to it. Wafer is 25 mm in diameter, with approximately 1 mm overlap by copper mount around the outer edge.

Cziczo et al., 2013]. JSC Mars-1 is made from glassy volcanic ash (palagonitic tephra) originating from cinder cones between the Mauna Loa and Mauna Kea volcanoes in Hawaii [*Allen et al.*, 1997]. It is mainly composed of oxides and has particles mainly around 10-1000 microns in diameter [*Allen et al.*, 1997; *Allen et al.*, 1998]. MMS is made of Saddleback Basalt from the Mojave Desert. MMS is mainly composed of oxides, as well as other trace minerals, and has particles mainly 10-100 microns in diameter [*Peters et al.*, 2008]. ATD is dust that settles out of the air in the Salt River Valley, AZ[1]. It is mainly composed of oxides and has particles up to around 60 microns, with various grades available to purchase[2] [3].

Many Mars laboratory studies have also examined phase changes of water in the presence of salt. This topic receives much attention because of the implications for life on Mars. Salts may allow for the existence of liquid water on the surface of Mars under

---

[1]http://www.powdertechnologyinc.com/test-dust-contaminants/test-dust-history/. Accessed: 2016-03-09.

[2]http://www.powdertechnologyinc.com/product/0-specified-test-dust-grades/. Accessed: 2016-03-09.

[3]http://www.powdertechnologyinc.com/wp-content/uploads/2012/08/MSDS.01.Arizona-Test-Dust.4-April-2012.pdf. Accessed: 2016-03-09.

conditions where it would otherwise sublime or be frozen. Laboratory studies have examined phase changes of water in the presence of salt under Mars surface conditions with the goal of seeing how salts might lower the freezing point of liquid water on the surface. Brines that have been studied include chlorates, perchlorates, sulfates, and chlorides. Perchlorates in particular have been of interest because of their capability for deliquescence on the surface of Mars, as seen with transient brine predictions at Curiosity rover in Gale Crater linked with observed water activity [*Martin-Torres et al.*, 2015] as well as hydrated salt spectra linked with recurring slope linae on Mars [*Ojha et al.*, 2015].

1.3   Summary: Models and laboratory to examine clouds under Martian conditions

The more the scientific community has learned about Mars through missions, the more in-depth questions arise about clouds on the planet. Martian clouds have been the topic of much scientific investigation in the forms of climate modeling, laboratory work, and missions to Mars. Water ice clouds, in particular, have been examined using these methods, as these clouds are an important part of the Martian water cycle and the overall climate cycle. We examine the following questions in this work:

- What processes influence water ice cloud formation and evolution?

- How do source materials influence water ice cloud formation?

- Do clouds on Mars behave, from a radiative forcing perspective, as we might expect?

1.3.1 Water Ice Cloud Processes on Mars using a Mars General Circulation Model

Chapter 2 examines how well the Martian water cycle is simulated by the NASA Ames Mars General Circulation Model. We compare model results to observations of Mars, primarily from MGS TES, and we identify water ice clouds as playing a central role in the discrepancy between the model and observations. Modifications to the water ice cloud microphysics, specifically the nucleation scheme, are made in an attempt to bring model results closer to observations. The role of water ice clouds at the residual North Polar Cap is of particular interest, and this study illustrates the strong sensitivity of the Martian global water cycle to clouds over the North Polar Cap region.

1.3.2 Laboratory studies of salts as condensation nuclei for water ice clouds under Martian conditions

Chapter 3 details laboratory experiments of water ice nucleation onto salt substrates. This research builds on previous laboratory studies of water cloud formation under Martian atmospheric conditions, which are colder, lower pressure, and drier than those experienced on Earth. In recent years, observations of the Martian surface have indicated the presence of chlorine salts, such as chloride-bearing minerals plentiful in the Southern Hemisphere, as shown in Fig. 1.6, and perchlorates observed by the Phoenix lander in the Northern Hemisphere [*Hecht et al.*, 2009]. These salt-bearing minerals would potentially be source material for dust lofted from the surface into the Martian atmosphere, providing potential nucleation sites for water ice clouds. Considering that salts play an important role in cloud formation on Earth, it is important to have a better understanding of how salt may affect nucleation processes under Mars-like conditions. We use a vacuum chamber that simulates the temperatures and pressures observed of the Martian atmosphere. Using infrared spectroscopy we measure the onset of nucleation and calculate the temperature-dependent critical saturation ratio (S_{crit}) and resulting contact parameters for water ice nucleation onto salts, specifically sodium chloride and
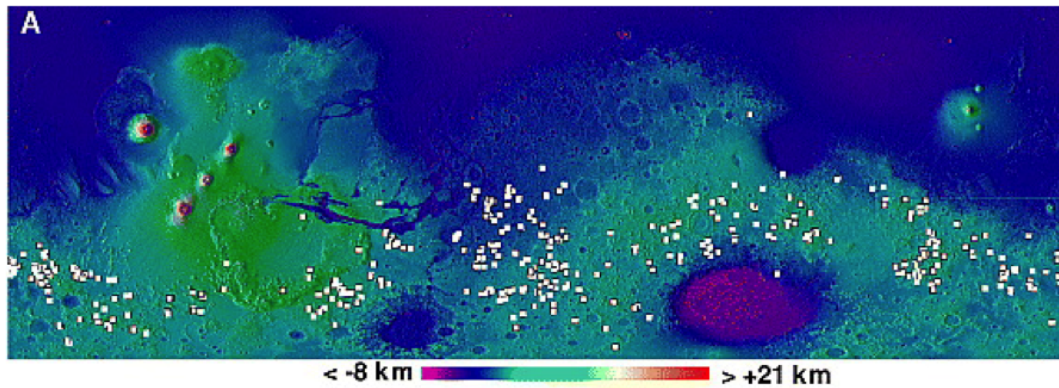
Figure 1.6: Areas of proposed chloride-bearing minerals on Mars marked by white boxes, on top of MOLA elevation relief. Coordinates are from 60°N to 60°S and 180°W to 180°E. (From *Osterloo et al.* [2010], Figure 9a.) The map is a simple cylindrical projection and the map height is 7100 km.

sodium perchlorate.

1.3.3 Temperature-dependent radiative transfer modeling of Martian water ice clouds

Chapter 4 examines how the energy budget in the Martian atmosphere is affected by temperature-dependent optical properties in Martian water ice clouds. This work was based on laboratory investigations showing a variety of water ice spectral profiles. These spectral profiles were previously explained in part by the work of *Clapp et al.* [1995] and their consideration may be important for Mars climate modeling because some water ice spectra are indicative of increased scattering, which would have an effect on radiative properties. This work uses laboratory derived measurements within a 3D MGCM to calculate the instantaneous changes in radiative fluxes in the atmosphere in response to using different, temperature-dependent optical parameters.

Chapter 2

Examining Water Ice Cloud Processes on Mars using a Mars General Circulation Model

2.1 Introduction

The Martian climate has captivated peoples' imaginations almost as long as the planet itself has. While the present Martian climate is characterized as cold and dry, there are many geologic signatures that suggest fluvial processes on the surface (see[*Baker*, 2001], for a review), suggesting the possibility of a warmer and wetter climate in the past. The water cycle on Mars is of particular interest not only because of the observed fluvial features, but also because of the possible implications for life and because it is the dominant condensable volatile on Earth's surface.

Clouds have been observed on Mars since telescopes first focused upon the planet centuries ago, and have been observed in every Martian mission to date. Water clouds are an essential element of any Mars climate model, and impact the global energy budget and how water is transported globally. The representation of clouds in Mars climate models is sensitive to a variety of parameters, which this work will address. We aim to

better understand the role of water ice clouds on the Martian climate, with a focus on how processes are currently represented in a three-dimensional Mars General Circulation Model (MGCM) versus how the actual processes occur in real life, as inferred by observations.

2.1.1 Mars Climate Overview

On Earth, water is the only major constituent of the atmosphere that is condensable. In contrast, on Mars both water and CO_2 (the most abundant component in the atmosphere) exist as condensable volatiles. Water has a triple point of 273.15 K at 6.1 mbar [*Guildner et al.*, 1976], above which point it will either evaporate or sublime. CO_2 has a lower triple point of 216.55 K at 5.2 mbar [*Angus et al.*, 1976]. At a given temperature, the saturation vapor pressure for water is lower than that of CO_2, causing water to condense out of the atmosphere before CO_2. Thus, as temperatures decrease, water deposits on the surface first, with CO_2 potentially depositing on top. Both poles have seasonal CO_2 caps which are the main drivers of the seasonal pressure fluctuations on the planet and as much as a third of the CO_2 in the atmosphere is exchanged with the surface [*Smith*, 2001]. At the North Polar Cap (NPC), which is also the primary reservoir of water on Mars that influences climate, CO_2 is deposited annually in a thin layer over the water ice as temperatures decline in the Northern hemisphere fall [*Smith*, 2001]. This layer of CO_2 persists until temperatures begin to rise again, eventually exceeding the condensation temperature in the summer, causing it to completely sublime [*Farmer et al.*, 1976; *Kieffer et al.*, 1976]. In contrast, the South Polar Cap (SPC) is situated at approximately 6 km higher altitude relative to the NPC, making the conditions colder and the atmosphere more rarified. Under these conditions, CO_2 at the SPC never fully sublimes, even during the summer months.

The surface pressure varies below 6 mbar to over 10 mbar depending on the location and time of year [*Leovy et al.*, 1985]. The annual pressure cycle on Mars is dominated by CO_2, which makes up 95% of the atmosphere [*Owen et al.*, 1977]. The seasons can be defined using Solar longitude (L_s) as a reference. As measured from the Northern

Hemisphere, $L_s = 0°$ corresponds to the spring equinox, $L_s = 90°$ corresponds to the summer solstice, $L_s = 180°$ corresponds to the fall equinox and $L_s = 270°$ corresponds to the winter solstice. During the Southern summer, at perihelion $L_s = 270°$, the CO_2 cap on the South Pole sublimes and enters the atmosphere, increasing the atmospheric pressure. Measurements from the Viking Landers, back in the late 1970s and early 1980s [*Leovy et al.*, 1985], and more recently from the Mars Science Laboratory (MSL) mission [*Harri et al.*, 2014] have provided seasonal pressure data for several Mars years.

Water vapor is less than 1% of the atmosphere but has important radiative effects, particularly because of the low overall atmospheric mass. Water ice clouds also have strong radiative effects on the climate, even though there is less water condensed into clouds than as water vapor in the atmosphere. The NPC is mainly water and releases most its water around aphelion ($L_s = 90°$), which is the start of the Northern hemisphere summer. The NPC sublimes and forms visible water ice clouds that are observed at the poles and equator. Halfway through the Martian year, during the Northern hemisphere summer, a single Hadley cell leads to the formation of the Aphelion Cloud Belt, made of strongly forward and side-scattering particles with an effective radius of 3-4 µm [*Clancy et al.*, 2003], which demonstrate variability both seasonally and as temperatures change over the course of the day [*Smith*, 2009, 2004; *McCleese et al.*, 2010]. In particular, the Aphelion Cloud Belt is formed because there are fewer dust storms leading up to the Northern hemisphere summer, leading to cooler atmospheric temperatures. This results in a lower minimum altitude of water vapor saturation (below 10 km), allowing water ice clouds to form easily where water vapor is lifted around the equator [*Clancy et al.*, 1996]. These water ice clouds tend to cap the dust layer *Smith et al.* [2013]. Water ice clouds are also observed over the NPC itself, and tend to peak in the Northern hemisphere winter and dissipate before the Northern hemisphere summer, as observed with the MGS Mars Orbiter Camera [*Wang and Ingersoll*, 2002].

2.1.2   The NASA Ames General Circulation Model

The NASA Ames MGCM, specifically GCM2.1 v. 23, is used to study the sensitivity of water ice clouds on Mars because of its extensive history and use, as well as its sophisticated water ice cloud scheme. The model dynamical core solves the primitive equations (conservation of mass, energy, and momentum). The full physics calculations include atmospheric temperature, radiative transfer calculations, boundary layer properties (including ground heat transfer), carbon dioxide phase changes, and cloud microphysics [*Haberle et al.*, 1999; *Nelli et al.*, 2009].

In the MGCM the atmosphere and surface exchange water and CO_2. As a water reservoir, the NPC does not limit the amount of water that can sublime from it and its location is fixed throughout the year. The other key reservoirs of water include atmospheric vapor, ice clouds, and surface ice outside of the the NPC; the amount of water in these reservoirs is constrained by mass conservation. CO_2 is uniformly present in the atmosphere when the model initiates and exchanges between atmospheric and surface reservoirs as the model runs. The reservoirs for CO_2 are atmospheric vapor and surface ice, and mass conservation applies everywhere. CO_2 clouds are not included in this work. In accordance with physical properties of the volatiles, water will deposit at warmer temperatures than CO_2. The model allows for water vapor to add to a surface water ice reservoir even in the presence of an overlying CO_2 ice layer. However, water is not allowed to sublime from a CO_2 covered surface (the CO_2 must first sublime).

A default surface albedo for each location is specified from an input file and changes based on surface conditions. If there is CO_2 ice on the ground, the albedo is set to a fixed value dependent on whether the location is in the Northern or Southern hemisphere, 0.6 and 0.5 respectively. If there is not CO_2 ice but there is water ice, the albedo is set to a value of 0.4, unless the location is in the NPC defined by the model, in which case the albedo is set to the default value.

Because of the temperatures and pressures observed on Mars, water clouds are assumed to be ice in the MGCM. Fig. 2.1[1] shows longitudinally-averaged atmospheric

---

[1]Phase diagram from: http://www1.lsbu.ac.uk/water/water_phase_diagram.html#r1521. Accessed

temperatures observed by the Mars Global Surveyor Thermal Emission Spectrometer (MGS TES) at $L_s = 90°$, along with a phase diagram with water, which demonstrate that water in the Martian atmosphere will be in either the vapor or solid phase. The cloud microphysical scheme includes calculation of cloud particle concentrations, nucleation, depositional growth, and sedimentation [*Montmessin et al.*, 2002, 2004]. Atmospheric components of dust (mass and number), cloud dust core (mass), and water ice (mass and number) and treated as individual tracers, with a mean value for each component. For the nucleation scheme, the dust tracers are expanded into four size bins (as radii) that water can nucleate on to. These particle size bins are determined by a log-normal function and are constrained via user-defined minimum and maximum nucleation particle radii, r_{min} and r_{max}. After nucleation calculations are complete the model switches back to representing atmospheric components as tracers, at which point particle growth or evaporation rates are calculated.

In the model, water is transported in a variety ways. The first is resolved transport of atmospheric water (vapor and cloud-forming ice particles) by the model's dynamical core, which incorporates vertical and horizontal advection. Sub-grid scale transport of water is parameterized as eddy mixing and diffusion. Convective adjustment transports water and other tracers vertically in the model when the atmosphere is convectively unstable. Sedimentation of water ice is accounted for. Water can exchange between solid and vapor reservoirs via sublimation and deposition.

The various radiative effects of atmospheric water impact the global water and energy budgets. For water vapor and carbon dioxide, gas absorption coefficients, or k-coefficients, are calculated offline and used to determine an optical depth [*Lacis and Oinas*, 1991]. For water ice clouds, Mie theory is used for calculating absorption and scattering across seven visible and five infrared spectral bands (Table 1.1). The radiative effects of dust are prescribed and vary seasonally in this study.

2016-12-01.

(a)

(b)
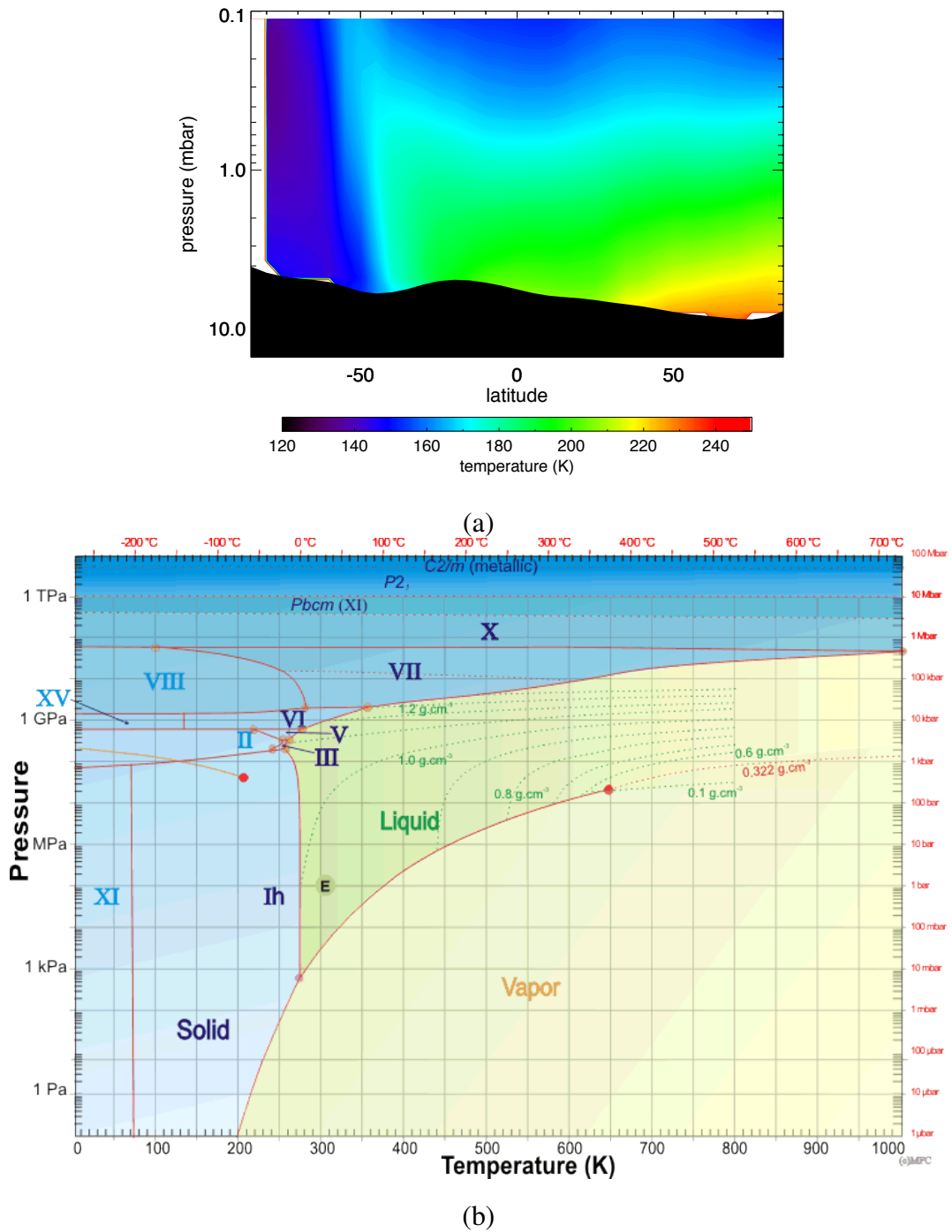
Figure 2.1: (a) Longitudinally-averaged atmospheric temperatures at 2PM local time for a 10-degree average about $L_s = 90°$, observed by MGS TES at Mars Year 26. (b) A phase diagram for water, with pressure in mbar/ bar on the right.

2.1.2.1 Previous studies using the NASA Ames MGCM

Various versions of the MGCM developed at Ames have been used extensively to examine dust and volatile distributions on Mars, e.g., [*Kahre et al.*, 2006, 2008]. The model reproduces temperatures and winds near the surface that are in good agreement with Mars Pathfinder observations [*Haberle et al.*, 1999], and has been used to investigate aspects of past Martian climates [*Haberle et al.*, 2003].

The radiation code in the MGCM has been used to calculate the radiative effects of water vapor and CO_2 and produces results in line with observations from MGS TES [*Nelli et al.*, 2009] as well as properties observed at the Phoenix Landing site [*Nelli et al.*, 2010]. When used in a 1D framework, the water ice cloud microphysics scheme, with radiatively active clouds, produces water ice cloud opacities consistent with Viking observations [*Montmessin et al.*, 2002]. A layered soil model is included, which allows for depth-dependent soil properties to vary down to 100 meters. This was shown to account for heat conduction to the surface, which leads to a CO_2 cycle that more closely matches observations by accounting for heat absorbed and stored in the summer and then released later, reducing CO_2 condensation onto the surface [*Haberle et al.*, 2008].

Radiatively active water ice clouds (RAC) have not been extensively used within the NASA Ames MGCM to investigate their impacts on the water and energy cycles, though it has been used to to investigate the magnitude of the greenhouse effect on Mars [*Haberle*, 2013] and to understand dust cycle feedbacks [*Kahre et al.*, 2015]. Early work suggests that the model does not model the water cycle well as a whole when full water ice cloud microphysics and radiative effects are included. This work aims to better understand the water cycle of Mars using the 3D MGCM by examining the water and energy cycles and how cloud microphysics and radiative feedbacks affect the various water reservoirs on Mars. We will do this by removing radiative effects and modifying the cloud microphysics scheme to understand the climate sensitivity to these factors.

2.2 Approach

The MGCM is run at a spatial resolution of 5° latitude by 6° longitude. A sigma co-ordinate system [*Gates et al.*, 1971] is used for a scaled pressure structure in the vertical dimension. Topography is obtained from the Mars Orbiter Laser Altimeter (MOLA). We use default albedo and thermal inertia maps previously described in *Kahre et al.* [2015], which are derived from Viking and MGS TES observations and mesoscale modeling. We define the water reservoir of the NPC based on the same datasets, specifically defining the NPC as where thermal inertia is 550 J/m^2·K·$s^{1/2}$ and above, as well as all regions northward of 80°N (Fig. 2.2).

Simulations begin with a uniform ground temperature and isothermal atmosphere set to 170 K and wind values set to zero. The model is not initialized with water in the atmosphere, with the NPC as the sole source of water to the model once the simulation begins. While the model dynamics require only 20-30 sols to equilibrate, we initialize each simulation for 7 Martian years to allow for the atmospheric water cycle to equilibrate from year to year; the last year of the simulation is examined in this work. These simulations are run with a dynamical core time step of three minutes. The full physics in the model, including cloud microphysics, are calculated every four time steps, or 12 minutes. The effects of CO_2 ice clouds are not examined in this work.

MGS TES observations from June 2002-August 2004 (spanning Mars years 26-27) are used to compare with model output. Observed atmospheric water abundances are derived from [*Smith*, 2002, 2004, 2008]. TES water ice cloud optical depths are measured at 825 cm^{-1}, or 12.1 μm [*Smith*, 2004, 2008]. These observations are compared with MGCM band 4, which spans a wavelength of 8.0-12.0 μm. The next closest spectral interval in the model is 12.0-24.0 μm. TES water vapor and water ice optical depth data are collected only during the daytime portion of the orbit, nominally 2 PM local time (generally ranging between 1 and 3 PM). Observed atmospheric temperatures are derived from *Conrath et al.* [2000] and *Smith* [2004, 2008], and daytime temperatures are primarily used for analyses in this study.
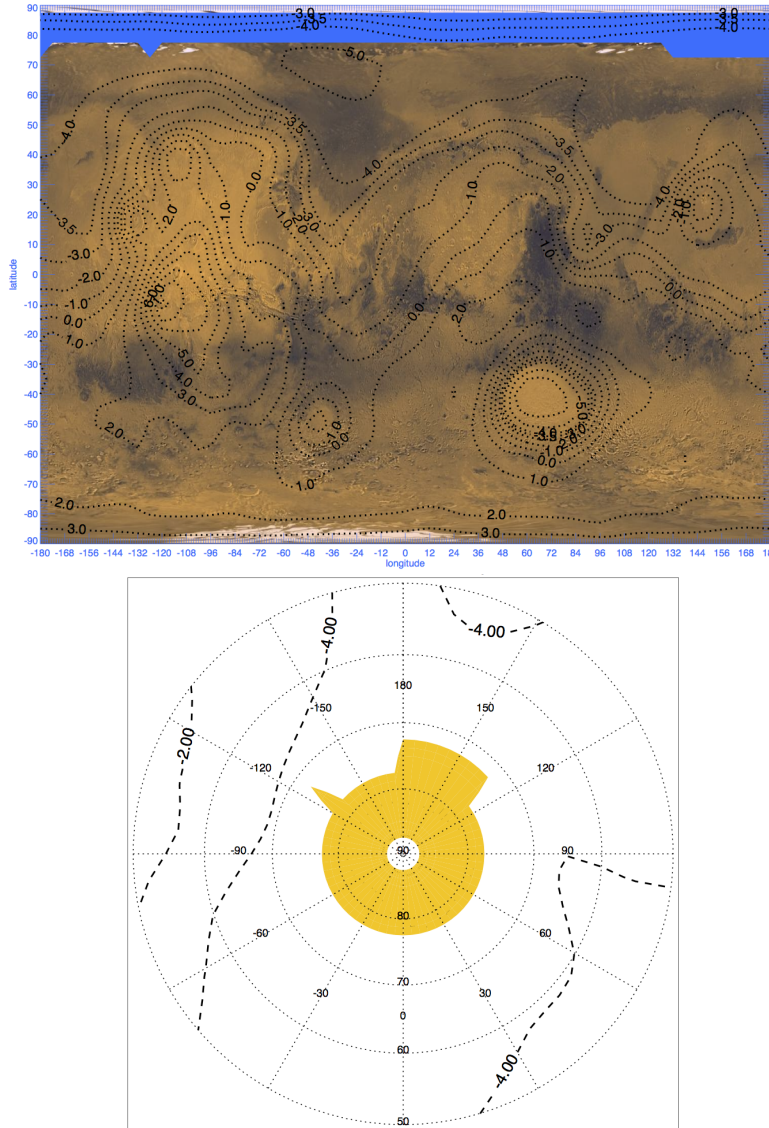
Figure 2.2: NPC defined water source as defined in the model. Dashed lines in both panes represent MOLA topography in km. The top pane shows Viking imagery of the planet with blue denoting the area defined as the residual NPC in the model. The bottom pane shows this same area in yellow on a polar projection of the North Pole, with the dotted lines indicating longitude and latitude.

26

Run name	Description
BASELINE	Radiatively active water vapor (RAV), latent heat effects of water, radiatively active water ice clouds (RAC)
NORAC	RAV, latent heat effects of water, radiatively inert water ice clouds
NUCLIMIT	Starting with the BASELINE case, but limiting the number of cloud particles that can be nucleation with the inverse of pressure
NUCLIMIT_CAPS	The same as NUCLIMIT, but only limiting nucleation +/-70° latitude, over both polar caps
NUCLIMIT_NPC	The same of NUCLIMIT, but only limiting nucleation +70° latitude, over the North Polar Cap
NUCLIMIT_SPC	The same of NUCLIMIT, but only limiting nucleation -70° latitude, over the South Polar Cap

Table 2.1: List of simulations performed in this study.

Table 2.1 lists the simulations performed in this study. The default simulation is referred to as the BASELINE case, which includes the default microphysics package and the radiative effects of water ice clouds and water vapor. The NORAC simulation removes the effects of radiatively active clouds (RAC) in order to explore the importance of RAC on the climate system. We explore various constraints on nucleation processes, including both parameterized and process-limited. This involves altering the microphysics scheme outlined in [*Montmessin et al.*, 2002] and assessing the sensitivity to these changes. In NUCLIMIT, an artificial limit is placed on the number of dust particles available for nucleation to form water ice clouds. This relationship is inverse

with pressure, so that there is a stricter limit on nucleation at lower altitudes where optically thick clouds may be hindering water sublimation off of the cap. This was done to explore the possibility that nucleation was occurring at too high a rate near the surface. NUCLIMIT_CAPS applies this nucleation limitation to only the poles, specifically +/- 70° latitude and poleward, to see how sensitive this parameterization was to latitude. NUCLIMIT_NPC and NUCLIMIT_SPC apply the nucleation limit to +70° and higher and -70° and lower, respectively to understand how these processes would affect the two poles differently.

2.3   Results and Discussion

2.3.1   BASELINE simulations compared with observations

The BASELINE simulation, which includes full physics, predicts an overall atmospheric surface pressure that is a good match to observations from the Viking surface landers (Fig. 2.3). The total mass of atmospheric water vapor is approximately half that observed by TES (Fig. 2.4), following the seasonal increases and decreases in water vapor mass over the course of the year. The overall cloud mass fraction of the total atmospheric water inventory (Fig. 2.5) is consistent with previous cloud fraction patterns seen in other Mars climate models [*Montmessin et al.*, 2004].

One possible reason that the model underestimates water vapor mass is that model clouds over the NPC are too optically thick in the infrared compared to observations. From this we infer that the modeled clouds are also too optically thick in the visible, with this bias reducing solar insolation at the surface ice, therefore reducing water subliming into the atmosphere. Lower daytime surface temperatures in the model, as compared to observations, are consistent with this hypothesis, with simulated ground temperatures poleward of 80°N during the summer lower than observations by upwards of 30 K (Fig. 2.6). Overall, the BASELINE version of the model is cooler than observations, but it is particularly noticeably at the poles and in particular the seasonal polar
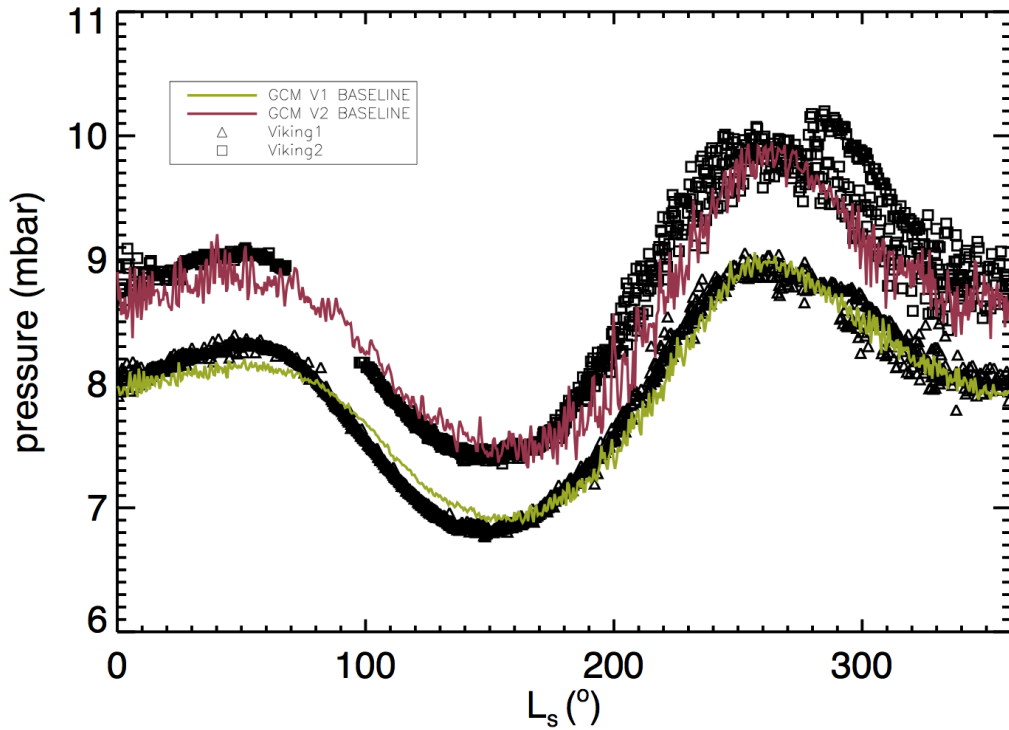
Figure 2.3: The seasonal cycle of surface pressure for the BASELINE simulation as compared to Viking lander data. Daily average pressure values from the duration of the mission are plotted for both Viking landers, with Viking 1 data represented by triangles and Viking 2 data represented by squares. "GCM V1 BASELINE" and "GCM V2 BASELINE" refer to the pressures from the BASELINE simulation at the same location as the Viking 1 and 2 landers, respectively (using data from a single grid cell approximating lander location and adjusted for the elevation of the landers).

Figure 2.4: The seasonal cycle of the global sum of water vapor mass in the atmosphere, measured at 2 PM local time, for the BASELINE and NORAC simulations, in comparison with TES observations taken at 2 PM local time.
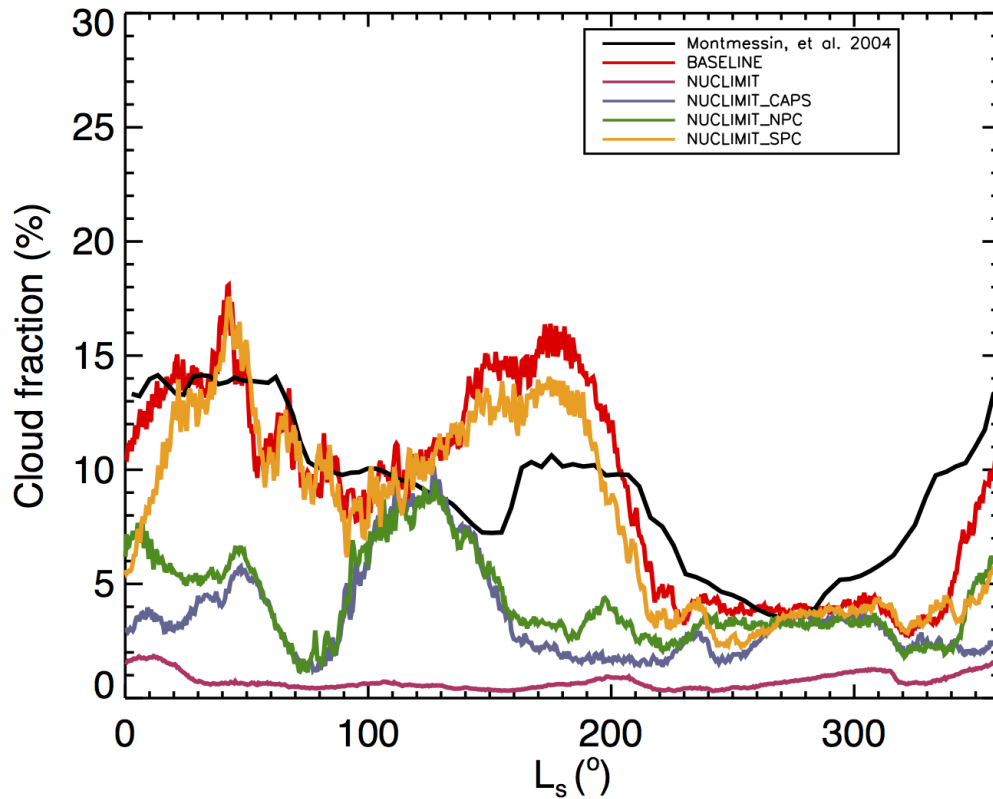
Figure 2.5: The seasonal cycle of the global water ice cloud mass as a percentage of the global water vapor mass for the BASELINE and nucleation limiting simulations, measured at 2 PM local time.

cap edge.

Correspondingly, the water ice cloud optical depth is much higher in the model than observed, particularly during Northern hemisphere summer and fall, when water is subliming from the NPC (Fig. 2.7b). Column water vapor is present in lower amounts in the BASELINE model than observed, particularly at the edge of the NPC (Fig. 2.8). The zonally-averaged temperature profile during Northern hemisphere summer indicates cooler modeled temperatures over the NPC (Fig. 2.9), a time when peak sublimation should be occurring. The connection between atmospheric radiative properties and the water cycle are explored later.

31
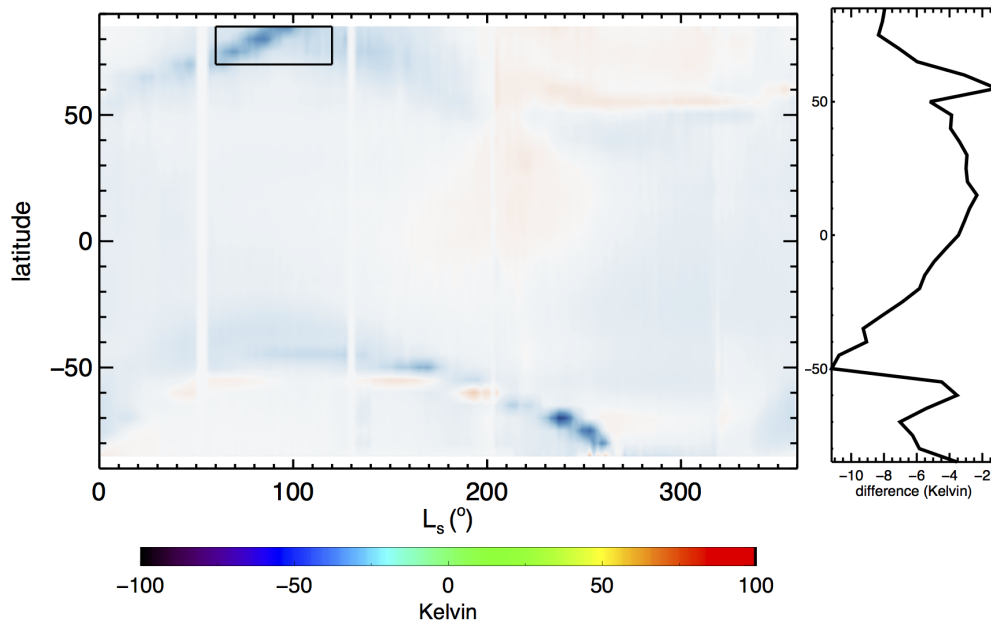
(a)   (b)

Figure 2.6: Ground temperature comparisons between the TES and the BASELINE simulation at 2 PM local time. (a) TES values subtracted from BASELINE, as a function of season and latitude; ground temperatures are averaged across longitudes for 2 PM local time. The outlined box, or "NPC box", indicates a spatial and temporal region particularly sensitive to radiative processes in the model and is examined in more detail in the text. (b) TES values subtracted from BASELINE, as a function of latitude and averaged over one year for 2 PM local time.
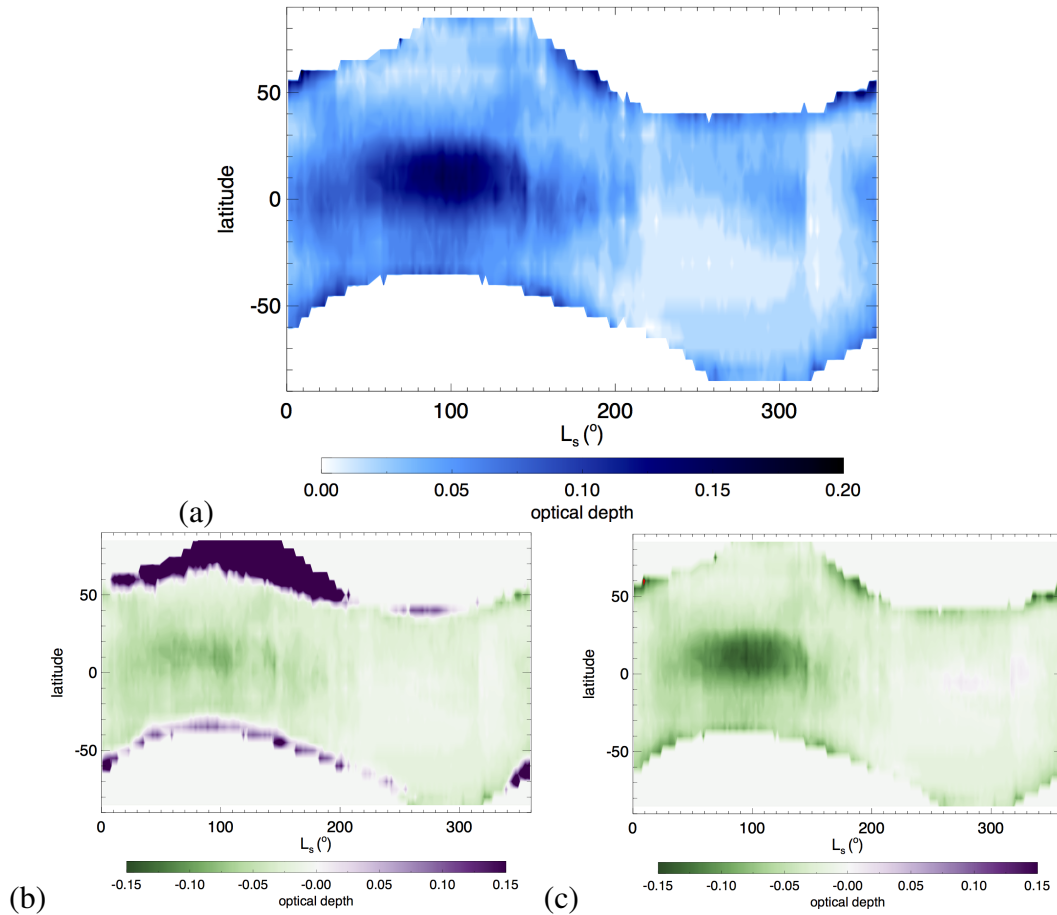
Figure 2.7: Optical depth observations and comparisons as a function of season and latitude, averaged across longitudes for 2 PM local time. (a) Optical depth measured by TES at 825 cm^{-1}. (b) Optical depth values observed by TES subtracted from the BASELINE simulation (833-1250 cm^{-1}). (c) Optical depth values observed by TES subtracted from the NUCLIMIT simulation (833-1250 cm^{-1}). For difference plots, positive values indicate higher values in the simulation and negative values indicate lower values in the simulation as compared with TES.

33
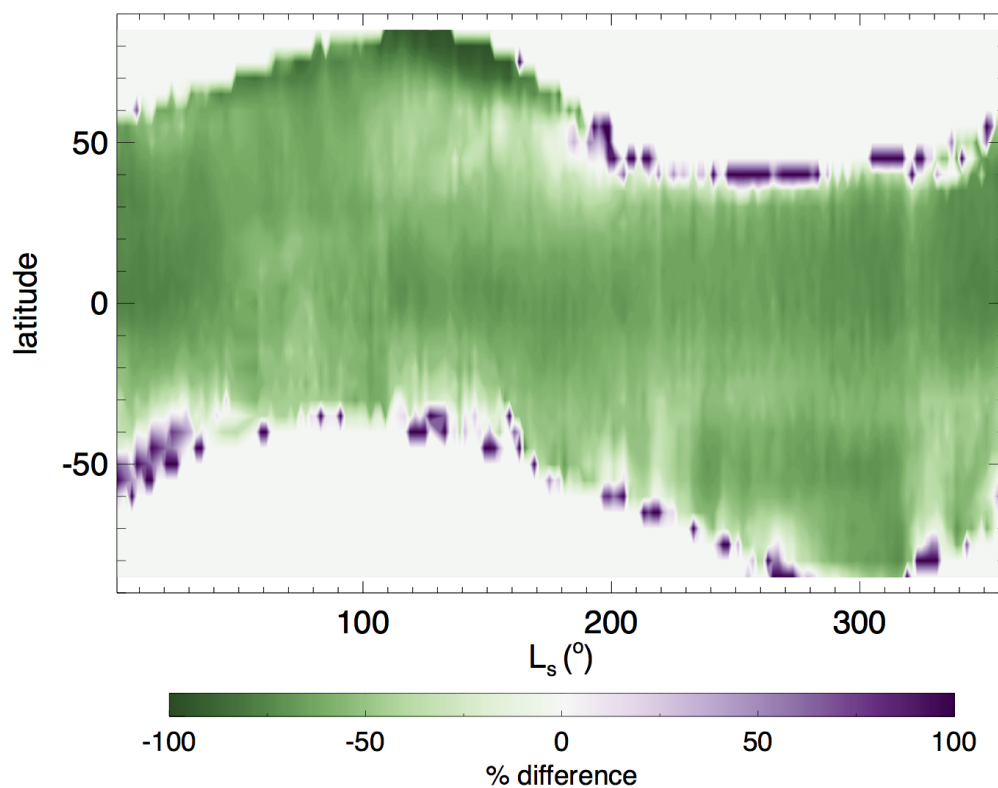
Figure 2.8: A comparison of TES and BASELINE simulation values of column integrated water vapor as a function of season and latitude, averaged across longitudes for 2 PM local time. Differences are calculated as BASELINE minus TES values, divided by TES values and shown as a percent. Positive values indicate BASELINE water vapor levels higher than TES, while negative values indicate values lower than TES.
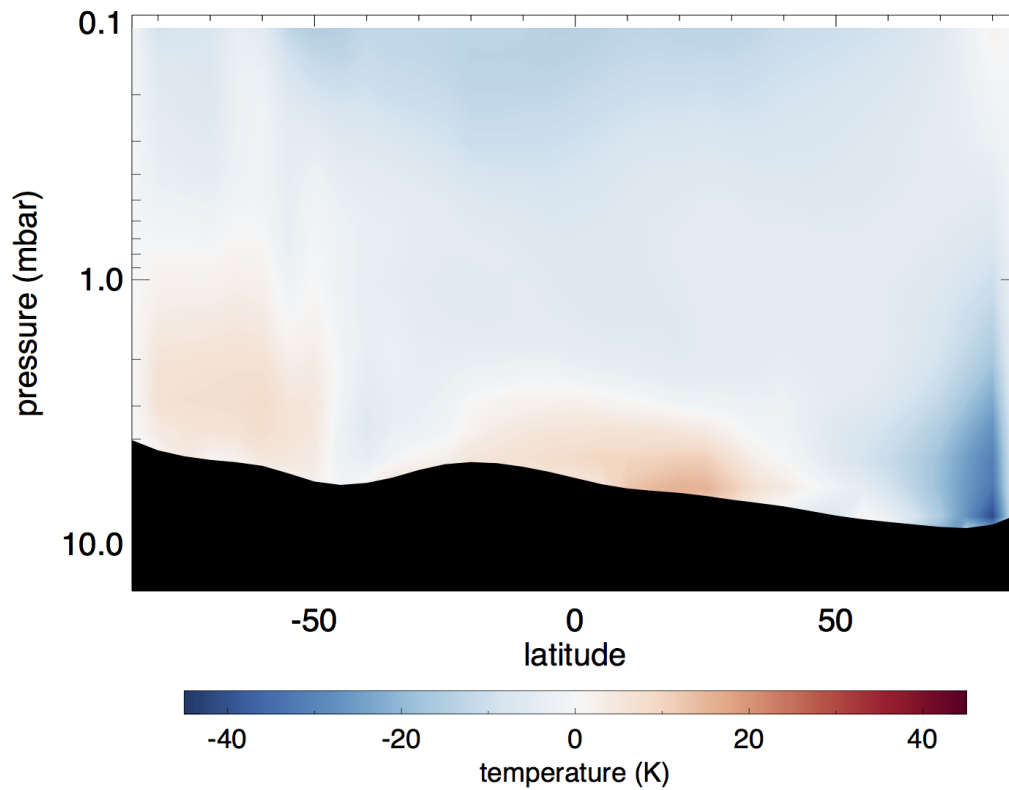
Figure 2.9: A comparison of TES and BASELINE atmospheric temperatures as a function of latitude and pressure, averaged across longitudes for 2 PM local values for a 30-day average about $L_s = 90°$. Differences are calculated as BASELINE minus TES values; positive values indicate a warm bias in the BASELINE simulation, while negative values indicate a cool bias in comparison to TES.

We define a spatial and temporal region of interest in order to quantify how different scenarios represent processes at the NPC. This "NPC box", outlined in Fig. 2.6, is defined as the longitudinally-averaged area poleward of 70°N (up to 85°N, the most poleward point in the model), between L_s 60°-120°, centered around the Northern hemisphere summer solstice. During the time of year when insolation is greatest over the NPC, the model has a greater optical depth than observations and a corresponding lower column water vapor. Where TES observations are available, the NPC box has an average infrared optical depth of 0.028, a water vapor column abundance of 38.5 precipitable μm (pr. μm), and surface temperature of 221 K, while the BASELINE simulation has an average infrared optical depth of 1.28, column water vapor of 8.65 pr. μm, and surface temperature of 193 K.

2.3.2   Radiative properties of the atmosphere

The low bias in total water vapor mass could be due to a low bias in the NPC sublimation flux. The latter is controlled by the surface energy budget of the NPC, which in turn can be affected by both water vapor and water ice clouds. Water vapor exerts a greenhouse warming on the surface, but it is much weaker than forcing from water ice clouds. Water ice clouds cause both surface warming at thermal infrared wavelengths, as well as surface cooling at solar wavelengths. We explore these effects with simulations that independently turn off each mechanism.

In the model, the NPC is most sensitive to the effects of water ice clouds. If the shortwave and longwave radiative effects of water ice clouds are excluded (the NORAC simulation), the global water vapor mass increases from half that of TES observations to more than double observations (Fig. 2.4) during to an increased energy flux in the absence of radiatively active clouds. This corresponds to an increase of a factor of between 4 to 9 relative to BASELINE, depending on the time of year. Global water ice cloud mass also increases over tenfold, particularly during the Northern hemisphere summer (now shown). One-dimensional radiative-convective modeling has also shown that the presence of water ice clouds can lead to infrared cooling close to the surface

[*Colaprete and Toon*, 2000].

Correspondingly, in the NPC box the daytime ground temperature in the NORAC simulation is 216 K, 23 K warmer than the BASELINE simulation and much closer to the TES observations of 221 K in that region. The BASELINE and NORAC simulations also predict different surface albedos in the NPC box, with values of 0.37 and 0.33, respectively. We attribute the surface albedo difference to the difference in temperature, which results in a positive feedback to the areal ice coverage.

Given that the global water cycle is very sensitive to the shortwave properties of water ice clouds over the NPC, we next explore the model processes that govern these properties.

2.3.3 Cloud Nucleation limiting

In order to explore the hypothesis that radiatively active water ice clouds in the model dry the atmosphere by excessively cooling the NPC and suppressing water sublimation, we implement various changes to the cloud formation scheme and evaluate model output sensitivity to these changes. Each of the schemes distributes cloud mass among the predicted nucleated particles, with the number of particles nucleated varying between different scenarios.These tests are all done with radiatively active water vapor and ice clouds. We expect nucleation to modulate cloud particle size and concentration, both of which in turn affect cloud optical depth. All sensitivity simulations reduce the number of nucleated particles at each microphysical timestep of 12 minutes.

One reason the model may overestimate the cloud particle concentration is the assumption that supersaturated conditions are sufficient for particle nucleation. Laboratory studies have shown that at low temperatures similar to those on Mars, a higher saturation ratio is required for nucleation onset, and therefore cloud nucleation is more difficult to achieve relative to classic nucleation theory [*Trainer et al.*, 2009; *Iraci et al.*, 2010; *Phebus et al.*, 2011]. This is consistent with recent observations that have shown water vapor in excess of saturation on Mars [*Maltagliati et al.*, 2011]. We performed a simulation where we use a temperature-dependent critical saturation ratio for nu-

cleation onset, as determined from laboratory experiments [*Iraci et al.*, 2010; *Phebus et al.*, 2011], as opposed to the usual requirement of a saturation ratio simply greater than 1.0. This constraint led to more water vapor in the atmosphere, but the simulation ends due to numerical instabilities. Alternate cloud microphysics schemes may be necessary to incorporate temperature-based critical saturation ratio into the model. In order to circumvent the model instabilities, we perform simulations with modified nucleation schemes that produce the same outcome as temperature-dependent critical saturation ratio, which is to reduce the number of cloud particles nucleated at a given timestep relative to the number of particles nucleated in the BASELINE simulation.

We next implemented a simple scheme of limiting the number of nucleated cloud particles to certain fixed values, such as 500 nucleated particles per kg atmosphere per microphysical timestep. While a greater restriction on the number of nucleated particles does increase the total water vapor mass by sometimes double (approaching observed values), including during the Northern hemisphere fall, total water ice cloud mass decreased by almost 95%, making clouds very scarce in the atmosphere. This was deemed unacceptable and we conclude that simple limits on the number of nucleated particles are not an appropriate method to reduce cloud nucleation to follow temperature-dependent nucleation criteria.

The high bias in simulated cloud optical depths is prominent at higher latitudes, particularly during the Northern hemisphere summer (Fig. 2.7a), with the BASELINE simulation producing optically thick water ice clouds at low altitudes very near to the surface (not shown). To address the high near-surface values of optical depths in the model, we evaluated whether variations in the vertical profile of nucleation rate might affect the atmospheric water mass and surface energy budget. Using pressure as an analog for altitude, we performed a simulation NUCLIMIT, where we lower the number of dust particles nucleated based on the pressure in the atmosphere. The number of nucleated particles per kg air per microphysical timestep is set to 100/log(P), with "P" being pressure in mbar, for pressures greater than 1 mbar. Inversely limiting nucleation with pressure limits new cloud particle formation closer to the ground, which is where opti-

cal depth is overestimated the most. We find that this pressure-based nucleation limit-ing scheme brings the simulated water vapor abundance closer to observations relative to the BASELINE simulation, particularly during the Northern hemisphere summer (Fig. 2.10). The range of values for the atmospheric vapor mass for BASELINE is too small compared to observations, while the range for NUCLIMIT is closer to observa-tions, though it exceeds observations in the Northern hemisphere. The modified nucle-ation scheme also greatly reduces the high bias of water ice cloud optical thickness in the North Polar region. This is clearly depicted by comparison of the near polar region with large high bias of optical depth in Fig. 2.7b with the same region in Fig. 2.7c. We attribute the improvement of the water vapor cycle to the more realistic cloud optical depth in the North Polar region. Relative to the BASELINE simulation, the decrease in cloud optical depth also decreases cloud albedo, increasing surface insolation (by ~3 W/m^2), thus increasing water sublimation from the surface. While reducing nucle-ation improves the high bias of water ice cloud optical depths over the NPC, it leads to more discrepancies between the observations in other areas. The NUCLIMIT simula-tion shows a low bias for water ice cloud optical depth of the aphelion cloud belt over the equator during the Northern hemisphere summer (Fig. 2.5). NUCLIMIT leads to the aphelion cloud belt being reproduced more poorly compared with the BASELINE simulation. The cloud reservoir as a fraction of the total atmospheric water reservoir, seen in Fig. 2.5, is very low relative to values reported by previous studies [*Montmessin et al.*, 2004].

We next explore the sensitivity of the water cycle to clouds only over the polar caps. We perform a simulation where we limit cloud nucleation with pressure only at latitudes where column water vapor was biased low, specifically applying the 100/log(P) nucle-ation limit to poleward of 70°N (NUCLIMIT_NPC), over the NPC. Additionally, we limited cloud nucleation with height only at latitudes where cloud optical depth was biased high, applying the 100/log(P) nucleation limit to both 70° north and south lat-itudes (NUCLIMIT_CAPS). These simulations are performed because the formation mechanisms and evolution of water ice clouds at the caps may differ from those of
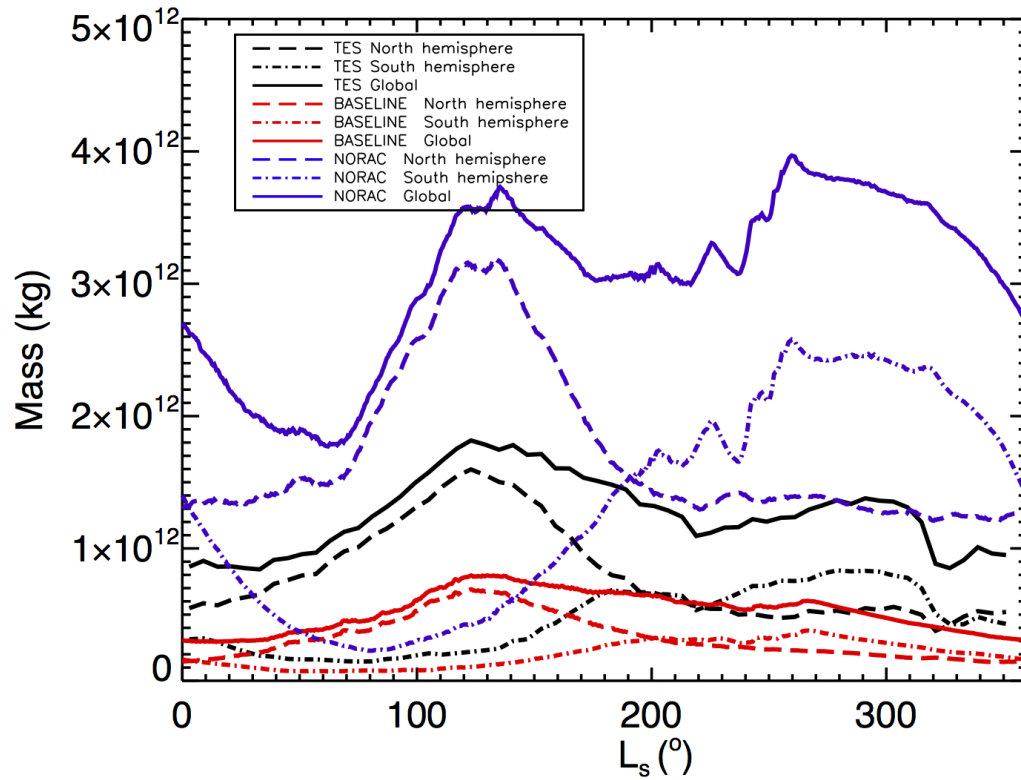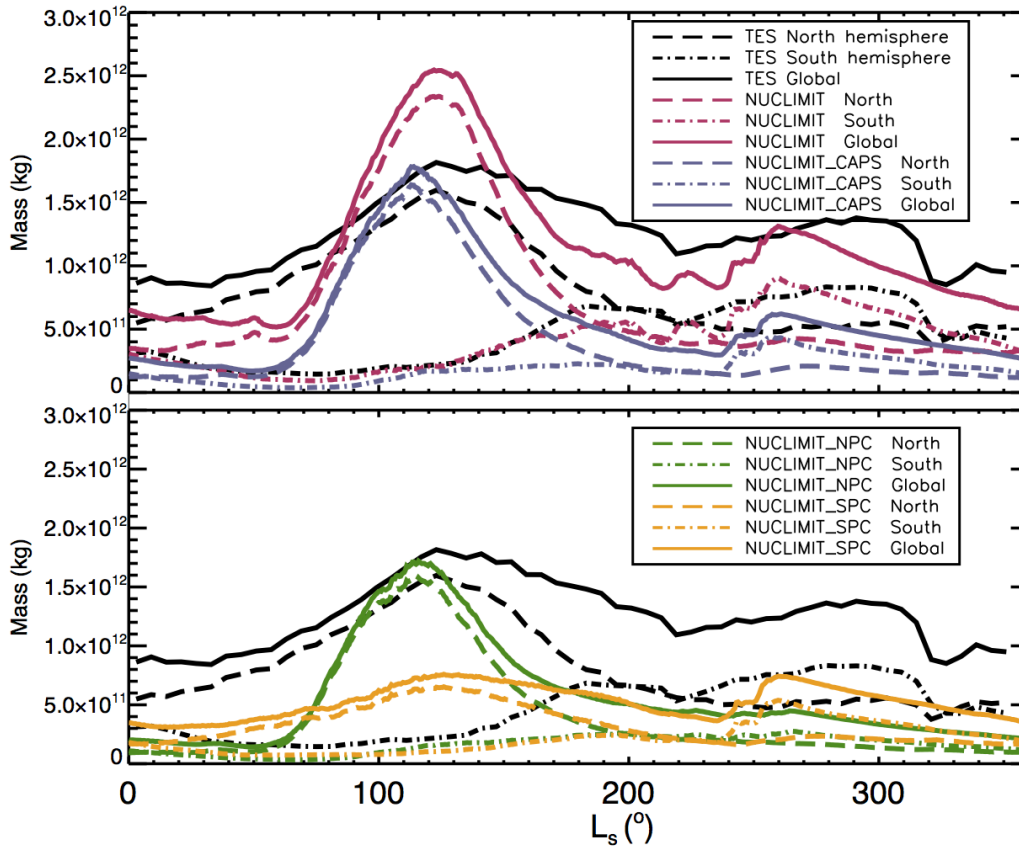
Figure 2.10: The seasonal cycle of the global sum of water vapor mass in the atmosphere, measured at 2 PM local time, for cases where the water ice cloud nucleation rate was limited, in comparison with TES observations taken at 2 PM local time.

clouds at the equator, with equatorial clouds more well-represented in the BASELINE simulation. These differences could be due to dynamics, cloud particle scavenging (collisional growth), or nucleation source material discrepancies not seen in the model. We find that both NUCLIMIT_NPC and NUCLIMIT_CAPS provide similar water cycles that are a closer to observations, in terms of total water vapor mass, and a cloud percent more reasonable than when nucleation is limited globally (Fig. 2.10), though they still underrepresent water vapor observations outside of the Northern summer season. For both of these cases, the water, cloud, and temperature patterns are closer to observations

at the poles as well as the equator, implying that setting this limitation globally, as in NUCLIMIT, alters equatorial clouds which are well-represented in the model already. This scenario also leads to a cloud reservoir fraction similar to those observed in other models, such as *Montmessin et al.* [2004] (Fig. 2.5).

The improvement of simulated cloud optical depth over the caps with the modified nucleation scheme could be due to the cloud regime in this region. In general, at the Northern hemisphere summer solstice vertical velocities over the NPC are negative and weak as compared to positive velocities over the equatorial region with twice the magnitude (as seen in BASELINE and other simulations, not shown). The cold surface of the NPC limits surface heating and convective instability. In addition, a substantial fraction of the incoming radiation results in sublimation rather than a sensible heat flux. Under such conditions on Earth, we would expect stratiform rather than convective clouds, e.g. Arctic stratus [*Curry et al.*, 1996]. Until recently, high resolution Earth climate models have done a poor job of representing such cloud types [*Harrington et al.*, 1999; *Harrington and Olsson*, 2001; *Sednev et al.*, 2009]. Modifying the nucleation scheme could be producing a more realistic water cycle by offsetting difficulties that the Mars climate model may have in reproducing NPC clouds. These difficulties could include nucleation at low vertical velocities, but may also involve dynamics, e.g. entrainment and turbulent transport. Regardless of the mechanism, the sensitivity of the water cycle to cloud properties over the NPC highlights the importance of accurately representing clouds in this region. These weakly forced clouds over the NPC may not be as well represented by the model's nucleation scheme as other clouds modeled for the planet, such as those at aphelion over the equatorial region, which are driven by more vigorous dynamics. Different nucleation schemes may be better suited for different circulation schemes, and that could be one reason that the clouds developing over the NPC are not well represented in the model.

2.4 Conclusions

The NASA Ames MGCM models the Martian water cycle well in terms of overall seasonal patterns, temperature patterns, and overall cloud distribution patterns. The water ice microphysics and radiative effects of the water cycle are robust in many ways but also introduce inconsistencies with observations. In particular, the optical properties of the water ice clouds prove to be a difficult feature to reconcile with observations in the northern high latitudes. In contrast, the MGCM produces an aphelion cloud belt similar to observations. The aphelion cloud belt is believed to be controlled by a lower latitude of water vapor saturation during the aphelion season, suggesting that the temperature and minimum altitude of water vapor saturation are well represented in the model, which are largely controlled by radiative warming of dust and atmospheric dynamics.

While the radiative effects of dust and atmospheric dynamics may be well represented in the model, the boundary layer scheme at the NPC in the Northern hemisphere summer may not be properly represented in the model. The radiative balance at the NPC, particularly at summer solstice, is important to the atmospheric water cycle on Mars, due to the local energy budget and the impact on sublimation of water at the cap, and the behavior of radiatively active water ice clouds has a large effect on this energy balance.

Preliminary work shows that limiting nucleation rates inversely with pressure near the surface may lead to water fractionation patterns more similar to observations than with the BASELINE model. While this approach was chosen because the model has a high bias for optical depth near the surface as compared to observations, overall this suggests that the vertical profile of nucleation matters and that a better understanding is needed of model's vertical sensitivity to nucleation conditions and criteria. One possible physical explanation for how this approach brought results closer to observations is that cloud particle scavenging near the surface may be faster that the model suggests. Additionally, limiting nucleation rates with pressure near the surface specifically over

the polar caps (NUCLIMIT_CAPS and NUCLIMIT_NPC) leads to water release at the Northern summer solstice closer to observations than applying this limit globally (NU-CLIMIT). This may be explained by the fact that clouds over the caps and clouds in the aphelion cloud belt form at different temperatures, and temperature dependent effects on nucleation onset are not accounted for in the model. Aphelion clouds often form at cooler temperatures, and though they are currently well represented in the model, it is possible that including temperature dependent limits on nucleation would improve modeled cloud microphysics at the poles but lead to new problems resolving equatorial clouds. Another possibility is that cloud nuclei source material at the North Pole is not well represented in the model. Additionally, changes in nucleation related to the low vertical velocities at the NPC may not be represented in the model. These different physical explanations for the sensitivity of cloud formation at the NPC may be related to differences in dynamics, and thus cloud formation processes, at the NPC versus other locations on the planet.

The water cycle in the model may also differ from observations because the model does not include all of the physical phenomenon known to exist on Mars. The planet has water ice exposed year-round on the South Polar Cap of Mars [*Titus et al.*, 2003; *Bibring et al.*, 2004] which presents a water source not currently included in the model. Since alterations to the water ice cloud nucleation scheme in the model do not seem to alter the water cycle at the South Pole very much, this is unlikely to have a strong affect on the global water cycle, but it is worth noting regardless. Another reservoir of water not included in the model is atmospheric water that is adsorbed on and desorbed from the regolith. Observations from the Phoenix lander mission show that over 10 pr. μm of water may adsorb onto the surface at night [*Zent et al.*, 2010; *Stillman and Grimm*, 2011]. The regolith may thus be a source of water at latitude lower than the perennial North Polar Cap, which would provide a source of water for the atmosphere that the model does not currently take into account. Additional physics would need to be added to the model in order to test this hypothesis.

We propose that a better understanding of the water ice microphysics above a cold

43

polar cap are required to more properly represent clouds over the NPC in the model. As suggested by modeling stratus cloud formation on Earth, limited convective instability may benefit from different nucleation schemes that used for modeling clouds elsewhere in the Mars climate system. Circulatory regime specific cloud microphysics may be an area of improvement for Mars climate models, which may require more observations over the polar regions, since observations are limited in these regions. Having a more robust understanding of polar clouds will lead to a better understanding of the atmospheric water cycle on Mars as a whole due to the large impacts that radiatively active water ice clouds have on the energy budget of the water-rich NPC.

Chapter 3

Salts as Water Ice Cloud Nuclei on Mars

3.1 Introduction

The history, stability, and physical form of water on Mars over the course of the planet's history is a topic of much scientific investigation in the forms of missions, observations, climate modeling, and laboratory work. Water ice clouds, in particular, have been examined using these methods, as these clouds are an important part of the Martian water cycle and the overall climate cycle. This work examines the role of salt aerosols as atmospheric water nucleation sites and the implications this may have for cloud formation and the climate of Mars. Salts have not yet been examined under Martian atmospheric conditions as possible water ice cloud nuclei.

Interactions between salts and water have been explored under conditions relevant to the planet's surface, but the temperature and pressure ranges examined to date are not representative of conditions in cloud-forming regions of the atmosphere. The research described here builds on previous laboratory studies of water cloud formation under Martian atmospheric conditions, which are colder, drier, and at a lower pressure relative to Earth's atmosphere and the Martian surface. Controlled test chambers have been

used to create Mars atmospheric conditions and observe cloud nucleation processes on various cloud nuclei analogs [*Trainer et al.*, 2009; *Iraci et al.*, 2010; *Phebus et al.*, 2011; *Ladino and Abbatt*, 2013; *Cziczo et al.*, 2013]. These experimental methods have also been used to study regolith-water interactions [*Chevrier et al.*, 2007, 2008; *Pommerol et al.*, 2009; *Beck et al.*, 2010]. Studies of water interactions under Martian surface conditions have used similar materials as used in cloud research, but also included several salts [*Chevrier et al.*, 2009; *Gough et al.*, 2011]. Research efforts have also focused on the characteristics of water ice on and under the surface [*Chevrier et al.*, 2007; *Siegler et al.*, 2012]. While Earth-focused research has studied salts as aerosols (for example, *Tang and Munkelwitz* [1993]), to date, they have not been investigated in laboratory studies as Mars cloud analogs.

3.1.1 Salts as cloud condensation nuclei

The presence of salts as cloud particle nuclei could change the nature of the cloud particle formation compared to dust substrates typically considered as cloud seed nuclei. On Earth, salt aerosols can undergo phase transformation in accordance with known deliquescence properties [*Tang and Munkelwitz*, 1993, 1994], taking up water more easily than other substrates while in the atmosphere. Thus, atmospheric salts on Mars could also provide a more hygroscopic substrate than cloud nuclei considered to date.

We assume that the Martian surface composition is representative of lofted dust that supports cloud particle nucleation. While studies have observed the mineral composition of airborne dust (for example, *Goetz et al.* 2005; *Hamilton et al.* 2005) via infrared and Mössbauer spectroscopy, salt is often not identifiable with these methods, so atmospheric salt may be overlooked by instruments observing atmospheric composition. Salts are observed on the surface in abundance, including chloride-bearing minerals [*Osterloo et al.*, 2008; *Glotch et al.*, 2010; *Osterloo et al.*, 2010] and perchlorates [*Hecht et al.*, 2009; *Leshin et al.*, 2013; *Glavin et al.*, 2013]. It is important to note that some surface composition analyses omit dusty covered regions [*Osterloo et al.*, 2010]

because it is harder to assess the actual surface composition under these conditions. In the absence of observations focused on identifying salts in the atmosphere, we take the surface observations as a proxy for dust composition.

We will examine the nucleation processes of water ice on sodium chloride and sodium perchlorate salt particles under Mars atmospheric conditions to examine cloud formation in various temperature and pressure regimes. Pressures referred to are partial pressures of water vapor, since we are considering water ice cloud nucleation. Perchlorate was chosen as a focus because of the recent observations [*Hecht et al.*, 2009; *Leshin et al.*, 2013; *Glavin et al.*, 2013] and the research done on perchlorate stability to date [*Chevrier et al.*, 2009; *Gough et al.*, 2011], including a possible link to deliquescence on the surface [*Ojha et al.*, 2015]. The formation of perchlorates on Mars could be similar to that on Earth or be from surface sources. For example, ClO radicals can adsorb onto ice to form precursors to perchlorates [*Catling et al.*, 2010]. Sodium perchlorate in particular is one of the possible perchlorates observed on Mars [*Hecht et al.*, 2009; *Ojha et al.*, 2015]. Chlorides were chosen based on emissivity observations integrated with spectral laboratory data and models that suggest that the presence of small chloride salt deposits on Mars [*Jensen and Glotch*, 2011; *Glotch et al.*, 2013]. Note that these salts are often seen in dusty areas with fine particles, conducive to providing cloud nuclei. Sodium was chosen as the cation for both.

3.1.2 Previous Mars cloud studies

The critical saturation ratio (S_{crit}) is the saturation ratio at which water ice begins to nucleate onto a substrate. Note that S_{crit} here refers to the saturation ratio and not the supersaturation value. The temperature-dependent S_{crit} values for Martian cloud analog materials have been previously studied with the same laboratory equipment and methods employed in this work [*Iraci et al.*, 2010; *Phebus et al.*, 2011], by placing martian mineral analogs onto a silicon substrate within a vacuum chamber. These and other studies of water nucleation demonstrated that at temperatures similar to those found on Mars, the observed S_{crit} values were higher than those predicted by classical

nucleation theory [*Trainer et al.*, 2009; *Iraci et al.*, 2010; *Phebus et al.*, 2011]. Recent observations have shown water vapor in excess of saturation on Mars [*Maltagliati et al.*, 2011], consistent with the laboratory findings.

Materials used for Mars cloud nuclei laboratory studies in the past include the Mars dirt simulant JSC Mars-1 [*Phebus et al.*, 2011; *Ladino and Abbatt*, 2013], Mojave Mars Simulant (MMS) [*Cziczo et al.*, 2013; *Ladino and Abbatt*, 2013], Arizona Test Dust (ATD) [*Iraci et al.*, 2010], and silicon wafers [*Iraci et al.*, 2010; *Trainer et al.*, 2009]. Other experimental methods have been used to test Martian surrogates for ice nucleation. *Ladino and Abbatt* [2013] tested nucleation on suspended aerosols (MMS and JSC Mars-1) inside a continuous flow diffusion chamber with a sheath flow of nitrogen. *Cziczo et al.* [2013] tested nucleation on freely suspended particles (MMS) in an inert nitrogen atmosphere. Both studies define S_{crit} as when a 1% of dust particles are nucleated. Because the methodology we use to observe nucleation uses a silicon substrate to hold the sample, it is assumed that our experiments would result in comparatively lower S_{crit} values because of the fact that our procedure identifies the earliest case of ice formation, while the suspended particle method requires 1% (or other fractions, as chosen) as a threshold for declaring nucleation to have occurred [*Ladino and Abbatt*, 2013]. However, this effect may be partially offset because of the fact that suspended particles also have a larger amount of surface area available for nucleation, which could allow for earlier nucleation. Earlier nucleation compared to our methods would have a higher equilibrium vapor pressure because of the higher temperature (since temperature is decreased over time during the experiments), and thus potentially result in lower S_{crit} values from these other experimental methods.

3.2   Methods

The experiments presented here used a methodology that has been previously published [*Iraci et al.*, 2010; *Phebus et al.*, 2011] and is briefly discussed here. Samples were prepared on silicon wafers (Lambda Optics) and installed into a vacuum cham-

ber, which was evacuated with a Pfeiffer TCP 300 turbomolecular pump to achieve chamber pressures in the high 10^{-8} Torr range. The chamber was cooled using liquid nitrogen, and the temperature was controlled by an Omega cNi8A Temperature & Process Controller with Minco flexible heaters. Pressure was adjusted by adding Milli-Q™ (ultrapure) water vapor through a needle valve into the chamber; this water source was freeze-pumped in an ethanol/ dry ice bath at the start of each experimental day to remove volatile impurities. Pressure was measured with an ion gauge (Terranova 934), and temperature data was collected using K-type thermocouples and a thermocouple data logger (TC-08, Pico Technology). Pressure data was collected as a voltage signal using TracerDAQ Pro, and temperature data from the thermocouples was collected using PicoLog Recorder (Pico Technology) software.

Infrared spectra were collected using a Nicolet Nexus 670 Fourier transform infrared (FTIR) spectrometer with a DTGS (deuterated triglycine sulfate) detector and Omnic software. 25 scans were co-added with 4 cm^{-1} resolution and collected every 33 seconds. The background spectrum was collected within 20 K of the anticipated nucleation temperature (with nucleation examined in the range of 150-180 K), at the desired pressure for the experiment. Reductions in temperature of 0.5-1.0 K were made approximately every 10 minutes to determine the temperature at which nucleation occurred for a given water partial pressure. Nucleation was identified by observing the infrared peak area integrated from 3500-3000 cm^{-1} with a 3500-3000 cm^{-1} baseline. The nucleation temperature (T_{nucl}) was assumed to be a value between the last temperature before nucleation and the first temperature after nucleation. In between nucleation events, the temperature was raised to $\sim$213 K and additional water vapor was prevented from entering the chamber for a full hour in order to ensure that all ice was removed from the chamber.

The ion gauge was calibrated for water with a Baratron capacitance manometer (MKS model 127AA). Temperature was calibrated each experimental day by growing ice and adjusting the temperature until the integrated area for the ice feature remained constant. The equilibrium vapor pressure for ice is used to calculate the sample tem-

perature (using equation (7) from *Murphy and Koop* [2005]). The offset between the calculated temperature at equilibrium and the measured temperature was applied to data collected throughout the day in order to achieve a calibrated temperature profile.

We used sodium chloride (NaCl, Redi-Dri™, anhydrous, free-flowing, ACS reagent, $\geq$99% from Sigma-Aldrich, product # 746398) and sodium perchlorate hydrate (NaClO$_4$ • H$_2$O, 99.99% trace metals basis, from Sigma-Aldrich, product # 381225). For each salt, the dry salt was mixed with Milli-Q™ (ultrapure) water and pipetted onto a clean silicon wafer and subsequently dried with a heat gun. A trace amount of salt was left on the wafer (sub-mg). After installing a silicon wafer with salt sample, the chamber was evacuated for at least two days before experiments began in order to achieve $\sim$1.0 x 10^{-7} Torr base pressure.

3.2.1   Data analysis

Data for a typical experiment is shown in Fig. 3.1. Nucleation temperature T$_{nucl}$ was calculated as the average of the temperatures before and after nucleation occurred, T$_{pre}$ and T$_{post}$. T$_{nucl}$ was used to calculate the equilibrium vapor pressure over hexagonal ice using equation 7 of *Murphy and Koop* [2005], which is appropriate for temperatures down to 110 K. S$_{crit}$ with respect to hexagonal ice was calculated using the partial pressure of water vapor prior to nucleation divided by the equilibrium vapor pressure calculated from T$_{nucl}$:

$$S_{crit} = \frac{P_{observed}}{P_{equilibrium}}$$

The partial pressure of water prior to nucleation was used, as opposed to an average of values before and after nucleation, since this measurement may decrease post-nucleation due to water uptake onto the substrate.

Nucleation is identified by observing the growth of water-related infrared features at 3500—3000 cm^{-1} associated with the O—H stretch. Fig. 3.1(a) shows how the saturation ratio changes over time during an experiment, and Fig. 3.1(b) shows spectra

(a)

(b)
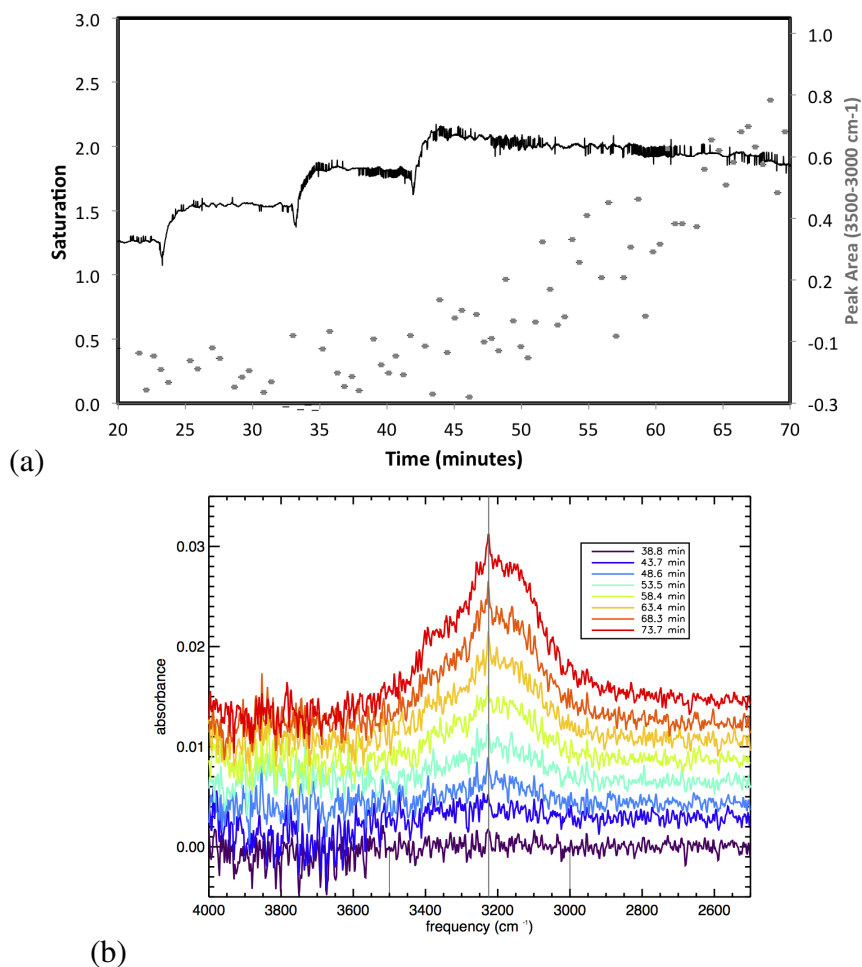
Figure 3.1: Data from a typical nucleation event is shown for a NaClO$_4$ experiment with a partial pressure of water of 3.8E-6 Torr. (a) Temperatures were reduced in approximately half-Kelvin steps, which correspond to increases in the saturation ratio over water ice. The temperature prior to nucleation, from 34-39 minutes, was 165.6 K with a saturation ratio of 1.8. Post-nucleation, the temperature was 164.7 K, with a saturation ratio of 2.1. (b) Spectra from the same experiment at different points in time. Spectra are offset by .002 absorbance units, each, starting from the first time show at 38.8 minutes. The key feature of crystalline water ice is at ∼3 microns, or 3225 wavenumber (cm^{-1}), shown with the vertical grey line. At 38.8 minutes (purple), no feature was visible at these frequencies, while by 48.6 minutes (light blue) water uptake was visible. A clear OH-stretching feature is seen by 63.4 minutes (yellow) which is indicative of crystalline ice. The baseline for the peak area calculations is 3000-3500 cm^{-1}, denoted by the vertical black lines at the bottom of the plot.

that correspond to different points in time during the experiment. Prior to the final temperature decrease (saturation increase) at 41 minutes, there was no observable O—H stretch. Within minutes after the temperature reduction, the O—H stretching feature became observable and continued to grow steadily for the remainder of the experiment. The band position and shape indicate that the O—H stretch was associated with crystalline water ice [*Warren and Brandt*, 2008]. The majority of these spectra had a single sharp peak at 3220 cm^{-1}, but in some spectra the the peak was broadened and right-shifted to $\sim$3000 cm^{-1}, and in others the band at 3500—3000 cm^{-1} was slightly broadened and had a flattened peak at the top from $\sim$3220-3120 cm^{-1}. These varieties of peak shapes were observed occasionally on all substrates, and are consistent with crystalline ice spectra predicted with increased scattering, as discussed in *Clapp et al.* [1995]. Both forms of crystalline ice, hexagonal and cubic, have similar spectra [*Warren*, 1984; *Mastrapa et al.*, 2009].

Error bars for S$_{crit}$ are calculated for each experiment based on the propagation of experimental uncertainties [*Taylor*, 1997]. The two sources of uncertainty come from temperature and pressure measurements. Sources of uncertainty for temperature measurements include error from averaging the temperatures T$_{pre}$ and T$_{post}$, uncertainty due to drift, and uncertainty due to calibration of the thermocouples. These temperature uncertainties are combined to result in uncertainties of vapor pressure, which result in positive and negative uncertainties in S$_{crit}$. Contributions to uncertainty of the partial pressure of water include uncertainty in the gas factor of water, the gas factor of air, base pressure observations, and raw uncertainty of the observed nucleation pressure. The uncertainties in vapor pressure and partial pressure of water are combined to yield a total uncertainty for S$_{crit}$. Temperature error bars are less than a degree on average and not shown.

The importance of temperature and substrate composition on S$_{crit}$ were tested with multiple linear regression, treating temperature as a continuous variable and the three substrate types as categorical levels. Nucleation temperature values were log-transformed to enable fitting of linear models.
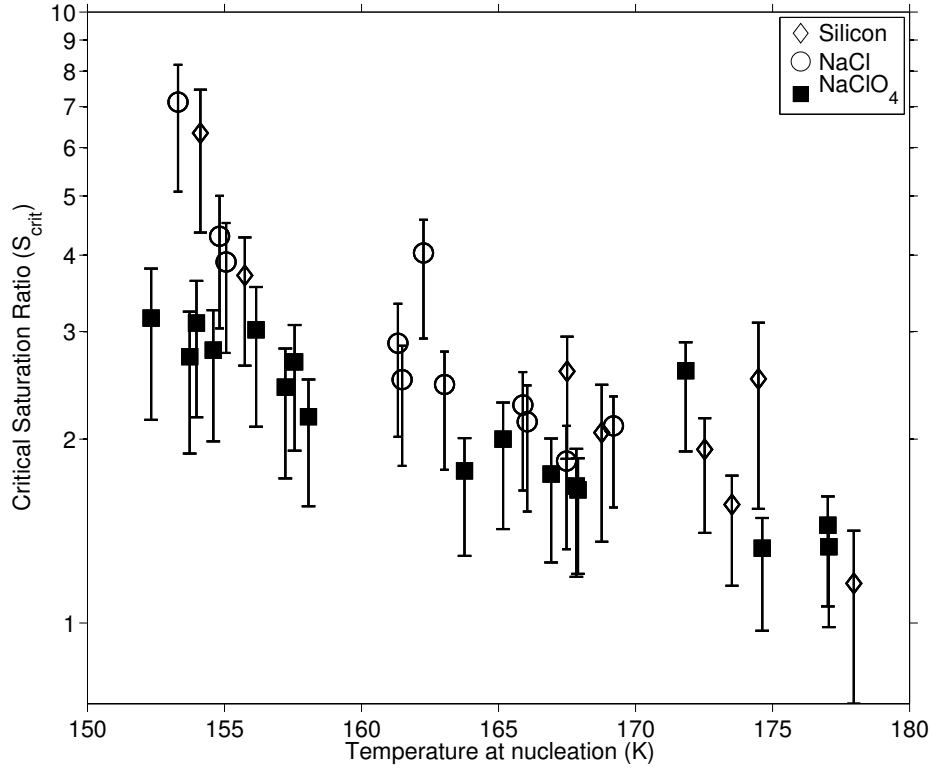
Figure 3.2: Temperature dependence of S_{crit} with respect to hexagonal ice for water ice nucleation on salts in this study; y-axis is a log scale. For bare silicon, $S_{crit} = 2.32E4*e^{-0.055T_{nucl}}$. For NaCl, $S_{crit} = 1.69E5*e^{-0.068T}$. For NaClO4, $S_{crit} = 3.32E2*e^{-0.031T_{nucl}}$.

3.3 Results and Discussion

Experimental data for water ice nucleation experiments on bare silicon and salt substrates are shown in Table 3.1. Each data point is a single nucleation experiment. The temperature dependent nucleation behaviors of water ice on sodium chloride and sodium perchlorate are shown in Fig. 3.2.

The S_{crit} required for nucleation on our salts is temperature dependent, as was previously demonstrated for dust analogs [*Iraci et al.*, 2010; *Phebus et al.*, 2011; *Cziczo et al.*, 2013; *Ladino and Abbatt*, 2013]. Our results also demonstrate different nucle-

T_{nucl} (K)	S_{crit}	P_{nucl} (Torr)	*A* value	Contact parameter *m*
On silicon				
154.1	6.3	8.6E-07	6.9E+14	0.77
155.7	3.7	7.6E-07	6.0E+14	0.83
167.5	2.6	8.3E-06	6.0E+15	0.86
168.8	2.1	8.6E-06	6.2E+15	0.89
172.5	1.9	1.8E-05	1.3E+16	0.90
173.5	1.6	1.8E-05	1.2E+16	0.93
174.5	2.5	3.5E-05	2.4E+16	0.85
178.0	1.2	3.2E-05	2.2E+16	0.98
On sodium chloride				
153.3	7.1	7.8E-07	6.3E+14	0.75
154.8	4.3	7.0E-07	5.5E+14	0.82
155.1	3.9	6.7E-07	5.3E+14	0.83
161.3	2.9	2.3E-06	1.7E+15	0.86
161.5	2.5	2.1E-06	1.6E+15	0.88
162.3	4.0	4.0E-06	3.0E+15	0.80
163.0	2.5	2.9E-06	2.2E+15	0.88
165.9	2.3	5.1E-06	3.8E+15	0.88
166.1	2.1	5.0E-06	3.7E+15	0.89
167.5	1.8	5.9E-06	4.3E+15	0.91
169.2	2.1	9.7E-06	7.0E+15	0.89
On sodium perchlorate				
152.3	3.2	2.7E-07	2.2E+14	0.86
153.7	2.7	3.4E-07	2.7E+14	0.88
154.0	3.1	4.1E-07	3.2E+14	0.86
154.6	2.8	4.3E-07	3.4E+14	0.87
156.2	3.0	6.9E-07	5.4E+14	0.86
157.2	2.4	7.2E-07	5.6E+14	0.89
157.6	2.7	8.6E-07	6.7E+14	0.87
158.1	2.2	7.9E-07	6.2E+14	0.90
163.8	1.8	2.5E-06	1.8E+15	0.92
165.2	2.0	3.8E-06	2.8E+15	0.90
166.9	1.8	5.0E-06	3.6E+15	0.92
167.8	1.7	5.8E-06	4.2E+15	0.93
167.9	1.7	5.8E-06	4.2E+15	0.93
171.8	2.6	2.1E-05	1.5E+16	0.85
174.6	1.3	1.9E-05	1.3E+16	0.96
177.0	1.5	3.3E-05	2.3E+16	0.94
177.1	1.3	3.1E-05	2.1E+16	0.96

Table 3.1: Experimental Conditions and Results

ation behaviors for NaCl salt, $NaClO_4$ salt, and the bare silicon wafer. These results suggest that not only may salts play a role as nucleation sites, but that the specific chemical properties of the salt may alter the nucleation behavior.

It is worth noting that while we calculate the vapor pressure of water with respect to hexagonal ice, it is possible that cubic ice or amorphous ice (the later particularly at colder temperatures) may be forming, and would results in different S_{crit} values than shown. Hexagonal ice is the most stable form of ice, and even if ice nucleated as another phase of ice it would later convert to hexagonal ice. If cubic ice formed initially, it could result in an S_{crit} that is ∼.3 less than that of hexagonal ice, while amorphous ice could have an S_{crit} that is ∼1.5 less than that calculated with hexagonal ice (using approximations based on vapor pressure ratios of $exp(\triangle G/RT)$ from *Murphy and Koop* [2005], where $\triangle G$ is the Gibbs energy difference between the different phases of ice). It is not possible to distinguish the phase of ice present in our experiments with the instrumentation used, but variation is data could be attributed to different types of ice forming at different vapor pressures.

3.3.1   Water ice nucleation on sodium chloride

Results for 11 water ice nucleation experiments on NaCl are represented by open circles in Fig. 3.2. We compare our results for NaCl with results from 8 bare silicon experiments, which are shown as small open diamonds. Both NaCl and the silicon control show a strong temperature-dependence, where at colder temperatures nucleation requires a relatively higher saturation ratio. NaCl experimental results show a temperature-dependence of nucleation with $S_{crit} = 1.69E5 {*}e^{-0.068 T_{nucl}}$. For silicon, the temperature-dependent profile is $S_{crit} = 2.32E4 {*}e^{-0.055 T_{nucl}}$. We use exponential fits for both of these temperature-dependent profiles, which is consistent with the functional form of S_{crit} with temperature from *Trainer et al.* [2009]. While some linear fits have been used for nucleation studies in the past, the sub-155 K data points suggest that more extreme cold temperatures require even higher saturation ratios than might be predicted from earlier work. In addition, exponential fits are better supported for

these data, as tested with a maximum likelihood estimation. The exponential fit to Si data has a log-likelihood of -7.63, compared to a log-likelihood of -8.51 for the linear fit. NaCl data is also better explained by an exponential model, with a log-likelihood of -11.88, compared to -13.02 for the linear model. We note that our silicon wafer results showed nucleation at slightly lower S_{crit} values than some other studies, but this was a consistent result within the time of these experimental runs.

Multiple regression indicates no significant difference of NaCl relative to Si (p=0.58), suggesting that NaCl does not significantly facilitate water ice nucleation preferentially in comparison with the control of a bare silicon wafer. As such, it is unknown whether water ice first nucleated onto the NaCl or onto uncovered parts of the wafer that contained the NaCl. Since silicon is chosen as the control substrate because of its tendency to not nucleate easily, our results suggest that NaCl may not facilitate water ice nucleation more than the absence of a substrate.

3.3.2   Water ice nucleation on sodium perchlorate

Results for 17 water ice nucleation experiments on $NaClO_4$ are represented by filled squares in Fig. 3.2. S_{crit} values for nucleation on to $NaClO_4$ were significantly lower at a given temperature than those for the control of bare silicon (p=0.001). $NaClO_4$ has a more shallow and linear temperature dependence than NaCl and silicon substrates. An exponential fit of temperature-dependent nucleation is $S_{crit} = 3.32E2*e^{-0.031\,T_{nucl}}$, which is shown in Fig. 3.2, while a linear fit would have a temperature dependence of S_{crit} = -0.065T_{nucl} + 12.8. Like for NaCl and Si, NaClO4 data are better fit by an exponential model (log-likelihood of -3.56) than by a linear model (log-likelihood of -4.34), although the difference in likelihoods is smaller than for the other substrates. To explore the functional form of our temperature-dependent nucleation behavior, other physical descriptors of the nucleation process are explored.

Our results can be expressed in terms of temperature-dependent contact parameter values, m, shown in Fig. 3.3. The contact parameter $m = \cos\theta$, where θ is the contact angle. A larger contact parameter means that it is energetically easier to nucleate a
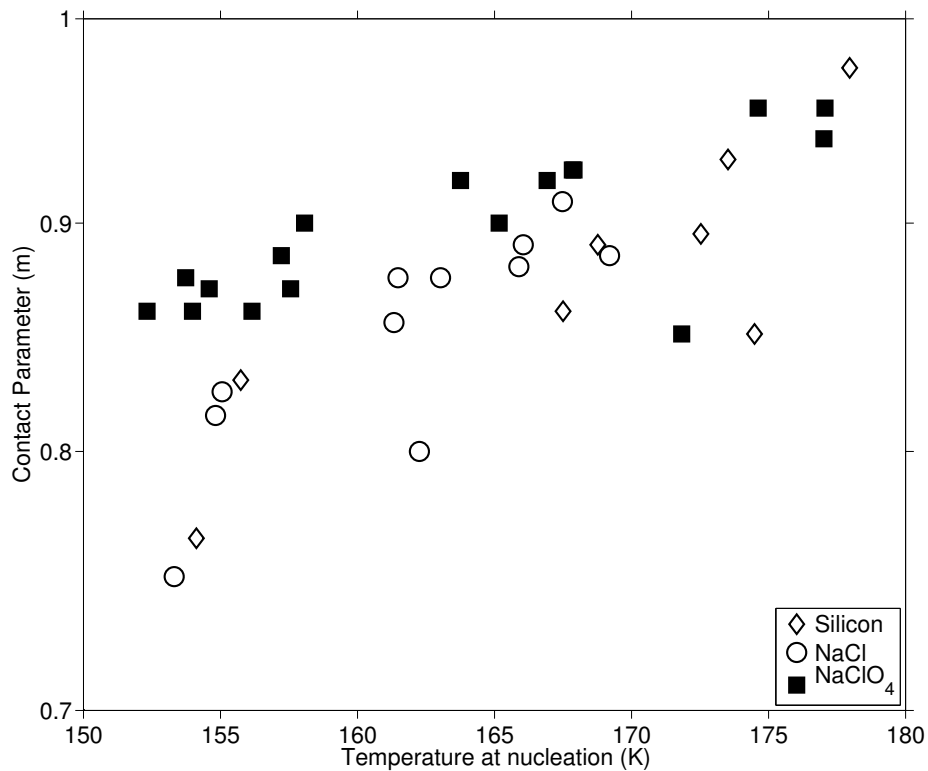
Figure 3.3: Contact parameter for nucleation experiments on salts and a silicon substrate in this study as a function of temperature, compared to a temperature dependent model of contact parameter for bare silicon; y-axis is a log scale. An exponential fit for previous bare silicon experiments provided the best fit for colder temperatures, shown here in blue. [*Määttänen et al.*, 2013].

particle. The contact parameter is a useful term in cloud microphysics models, and has a marked effect on the particle mass distribution size [*Iraci et al.*, 2010]. The functional form of the temperature-dependence of the contact parameter is of prime interest, as discussed in *Määttänen et al.* [2013], due to the application to cloud modeling and the fact that laboratory datasets may have a limited temperature range.

To calculate *m*, a planar approximation was used, as macroscopic particles larger than 8 μm were present in all samples, with a flat surface dominating the particle shape. The contact parameter *m* was identified by solving for the matching function *f*, using equation (9-18) from *Pruppacher and Klett* [1997]:

$$f(m) = \frac{(2+m)(1-m)^2}{4}$$

f was calculated using the equations (2) and (3) from *Fortin et al.* [2003], which were derived from *Pruppacher and Klett* [1997], with:

$$\triangle F = -k T_{nucl} ln(\frac{J}{A})$$

$$f = \frac{3\triangle F(RT_{nucl}\rho ln(S_{crit}))^2}{16\pi M^2 \sigma^3}$$

where is $\triangle F$ is the decrease in Gibb's free energy due to condensation and T_{nucl} and S_{crit} are observed values. Nucleation rate J was set to a constant value of $1 \text{ cm}^{-2}\text{s}^{-1}$, with *m* being insensitive to this value [*Fletcher et al.*, 2011]. The prefactor *A* was calculated using equations (3) and (4) of *Trainer et al.* [2009], which was derived from equation (9-8a) in *Pruppacher and Klett* [1997] and modified for lower temperatures. For matching function *f*, Boltzmann constant k = 1.38 x 10^{-23} J K^{-1}; gas constant R = 8.314 J K^{-1} mol^{-1}; molecular weight of water M= 18.015 g mol^{-1}; hexagonal ice density ρ was calculated from equation (3-2) of *Pruppacher and Klett* [1997] (for temperatures 93-273 K) ; and σ is the temperature-dependent surface tension for hexagonal ice calculated using *Hale and Plummer* [1974]. The prefactor *A*, or "kinetic coefficient", along with contact parameter *m*, are shown in Table 3.1.

Our NaCl and silicon results show a similar exponential pattern for temperature-dependence of contact parameter modeled by [*Määttänen et al.*, 2013], which was the best fit for both silicon and JSC-1 dust, while other dusts (ATD and smectite) were modeled to have a more hyperbolic tangent temperature-dependence for contact parameter . Our NaClO$_4$contact parameter results are less clearly exponential in form. Without extending the data collection range to lower temperatures, it is not possible to distinguish what provides the best fit for NaClO$_4$contact parameter data at this time, but it is possible that sodium perchlorate's contact parameter has a variability in temperature-dependence similar to other substrates, particularly one that nucleates water ice more easily than silicon.

3.4   Conclusions

Airborne NaClO$_4$ is a possible nucleation site for water ice clouds on Mars. NaClO$_4$ supports depositional nucleation at lower saturation ratios than NaCl and a bare silicon control. While NaCl may serve as a nucleation site for water clouds on Earth [*Tang and Munkelwitz*, 1993], under Martian atmospheric conditions it does not facilitate nucleation any more easily than our control.

It is unclear why the two salts studied here behave differently under Martian atmospheric conditions, but looking at other physical properties of the salts may provide context. The relative ease of taking up water between NaCl and NaClO$_4$is a similar pattern to their deliquescence relative humidities, with NaClO$_4$ taking up liquid water more than NaCl. Other research has shown that NaClO$_4$ deliquesces around 43-48% relative humidity (RH) [*Zhao et al.*, 2005; *Lu et al.*, 2008] and NaCl deliquesces around 72-83% RH [*Cziczo et al.*, 1997; *Lu et al.*, 2008; *Davila et al.*, 2010] at room temperature, with some of this variability due to the annealing of the particles [*Lu et al.*, 2008]. The deliquescence RHs for both NaCl and NaClO$_4$ have been shown to increase for decreased temperatures (*Cziczo and Abbatt* 2000and *Gough et al.*, 2011, respectively). At 273 K, the deliquescence RH was found to be 78% for NaCl [*Cziczo and Abbatt*,

2000] and 51% for NaClO$_4$[*Gough et al.*, 2011], while at 253 K, the deliquescence RH was found to be 80% for NaCl [*Cziczo and Abbatt*, 2000] and 56% for NaClO$_4$[*Gough et al.*, 2011]. While deliquescence is not the same process as nucleation, the relative hygroscopicity of the two substances suggests that NaClO$_4$ takes up and holds water molecules more easily than NaCl, perhaps due to the high chlorine oxidation state of NaClO$_4$. NaCl and NaClO$_4$ also have different crystal lattice structures and thermochemical radii [*Johnson*, 1968], which could affect how well water molecules stick to them in order for nucleation to occur.

Our findings have important implications for actual cloud formation patterns on Mars. Recent laboratory work comparing mixes of basalts and salts on Earth with observations from Mars Odyssey suggest the surface could be up to 25% chloride salts in certain regions on Mars [*Glotch et al.*, 2016]. Chlorides may be a precursor to perchlorate on Mars [*Catling et al.*, 2010], providing an substrate that could nucleate at substantially lower saturation levels. For example, at 155 K airborne NaClO$_4$ could nucleate water ice at partial pressures 40% lower than other substrates examined in this study. If clouds could nucleate at lower saturation levels, they may form higher in the atmosphere. Additionally, the presence of salt is very geographically variable [*Osterloo et al.*, 2008; *Hecht et al.*, 2009; *Glotch et al.*, 2010; *Osterloo et al.*, 2010; *Leshin et al.*, 2013; *Glavin et al.*, 2013]. Since salts potentially require lower saturation levels than other, dust substrates reported [*Iraci et al.*, 2010; *Phebus et al.*, 2011], water clouds could be forming more easily than previously thought in areas where salt is uplifted in the atmosphere. Certain areas on Mars could form clouds with lower atmospheric supersaturation if salts are indeed present in the local region.

This work can also be explored with microphysical climate models of Mars. If salt is indeed a component of the atmospheric particulate population on Mars, the temperature-dependent S$_{crit}$ and contact parameters presented here could provide alternative values for Mars climate modelers to use in cloud microphysics schemes. Regional differences in dust population may also be explored with regional climate models with different temperature-dependent S$_{crit}$ values and contact parameters that are most

relevant to the region.

Chapter 4

Temperature-dependent radiative transfer modeling of Martian water ice clouds

4.1 Introduction

The radiative effects of water ice clouds can warm or cool Mars depending on the time of day, cloud location, and cloud thickness [*Wilson et al.*, 2008; *Heavens et al.*, 2010; *Madeleine et al.*, 2012; *Kahre et al.*, 2015]. Radiative transfer modeling of these clouds is highly dependent on the optical parameters input into the models. Previous studies have used optical parameters, specifically the refractive indices, that were obtained from water ice at -7° C (266.25 K) regardless of the temperatures simulated by the model. In this study, we used optical parameters for ice measured at temperatures most relevant to Martian clouds to see the potential impacts on the Martian atmosphere's radiative balance. We use output from a Mars General Circulation Model (MGCM) to examine the instantaneous effects of having different water ice cloud optical parameters on the radiative budget of the planet.

The refractive indices of crystalline water ice, which have a real and imaginary com-

ponent, are intensive properties that are a function of temperature and wavelength. The real component, *n*, is the refractive index for the bulk material and primarily influences scattering. The imaginary component, *k*, is the extinction coefficient, which is representative of absorption by the bulk material. These measured parameters can then used by a light scattering and absorption code to estimate optical properties of atmospheric particles. Climate models utilize these optical properties for computing atmospheric radiative transfer. The majority of the values used for Martian radiative transfer modeling are based on data collected for clouds closer to the atmospheric temperature ranges of Earth.

One of the most widely cited sources for water ice optical constants is *Warren and Brandt* [2008], which compiled and made corrections for optical constant references for water ice for the microwave through ultraviolet region of the spectrum. Ices were assumed to all be hexagonal and the optical constants are assumed to be essentially identical for cubic ice [*Warren*, 1984; *Mastrapa et al.*, 2009]. As previously stated, for the majority of the infrared spectrum, which is what is commonly used in laboratory and orbital spectroscopy of ice, the optical parameters provided and used by others are from ices measured at -7° C (266.25 K). These values have been used in a wide range of Mars climate applications, from comparing orbiter observations to spectral model predictions to providing inputs for full 3D models of the Martian climate (e.g. [*Montmessin et al.*, 2002; *Clancy et al.*, 2003; *Madeleine et al.*, 2012]). Other relevant measurements of hexagonal ice in the infrared were examined by *Toon et al.* [1994], who measured optical constants at 163 K. While these measurements are relevant, the spectral and temperature range are limited.

Clapp et al. [1995] measured the refractive indices of ice in the infrared spectra between 130 and 210 K, at 10 K intervals. This temperature range was studied because of the application to studies of polar stratospheric clouds, but these temperatures are relevant to Mars cloud formation as well. Clouds on Mars have been seen at a range of temperatures. For example, contemporaneous cloud and temperature observations have identified clouds at $\sim$205-215 K [*Whiteway et al.*, 2009] by the Phoenix lander

and ∼160-175 K [*Christensen et al.*, 1998] by MGS TES. *Clancy et al.* [1996] suggest that water ice clouds were likely forming below 140 K, temperatures that are cooler than previously expected. We hypothesize that accounting for the temperature dependence of water ice refractive indices could have a noticeable impact on the simulated radiative behavior of water ice clouds on Mars.

4.2 Methods

We use the NASA Ames MGCM, specifically GCM2.1 v.23, to explore the impact of temperature-dependent optical constants on the energy balance on Mars. We examine the instantaneous effects of changing the optical properties of the water ice clouds in a Martian climate simulation to the radiative fluxes in each layer for the day time and night time. This is done to identify first-order effects of the water ice cloud radiative properties across a wide energy spectrum. The following assumptions are made:

- Radiative fluxes are examined instantaneously at 2 PM and 2 AM local time. 2 PM is chosen because of the large amount of incoming solar radiation to the planet, while 2 AM is chosen to understand the infrared energy behavior at night-time.

- Cloud properties (cloud number, mass, effective radius) and temperature are fixed between cases.

- Feedbacks are not included, though implied effects of changes in radiative fluxes are referred to as warming or cooling as appropriate.

- We only examine the effects on radiative transfer in water ice clouds. CO_2 clouds are not included in this simulation.

We use output from the BASELINE simulation described in Chapter 2, which includes the default microphysics package and the radiative effects of water ice clouds and water

64

vapor. Output from the seventh year of the run is used since the annual atmospheric water cycle has equilibrated. For the solar longitudes (L_s) of 0°, 90°, 180°, and 270° (corresponding to the Northern hemisphere spring equinox, summer solstice, fall equinox, and winter solstice, respectively), we calculate the radiative fluxes for two scenarios at both 2 PM and 2 AM local time: 1) using input for optical properties that were based on optical constants measured at -7 C [Warren 1984], which are the default properties for this model ; and 2) using temperature-dependent optical properties [*Clapp et al.*, 1995]. We shall refer to these cases as the WARREN and CLAPP cases, respectively. Results are averaged from data for two days, ten days apart, about the solar longitude of interest.

Optical properties of the water ice clouds in the model are determined by an input table that is read into the model. This table provides properties for extinction, scattering, and asymmetry in both the visible and infrared. Extinction incorporates absorption and scattering, scattering is when incident energy is reflected upward or downward, and asymmetry determines what fraction of light is scattered upward and what fraction is scattered downward. These properties in turn are used to calculate the radiative fluxes in the atmosphere.

4.2.1 Optical parameter calculations

The key aspect of this study is that the radiative properties of the water ice particles are calculated using different optical parameters for water ice than previously used for Mars cloud studies. Existing work uses values that are based on *Warren* [1984], which were measured at 266.25 K for wavelengths of interest. We use the refractive indices for water ice from *Clapp et al.* [1995], which are from 130-210 K and measured in 10 K intervals. *Clapp et al.* [1995] provided values between 800-4000 cm^{-1} (12.5-2.5 μm); for spectral calculations outside of this range, refractive indices from *Warren* [1984] were used.

The relevant water ice refractive indices for each case were used to generate optical properties for extinction, scattering, and asymmetry using Mie scattering code devel-

oped by *Toon and Ackerman* [1981]. In addition to using the refractive indices of water ice, the optical properties of dust from *Wolff et al.* [2009] are used to account for the dust center of the cloud particles. These calculations assume that energy is distributed via a Planck distribution and scales the parameters accordingly, with the assumption of a black body with an incident solar radiation of 6000 K in the visible and 215 K in the infrared to approximate the global atmospheric temperature.

Tables were thus generated for temperatures between 130 and 210 K that were then accessed by the climate model. For atmospheric temperatures that were below 130 K in the model, the indices at 130 K were used, and for temperatures above 210 K in the model, the 210 K indices were used. Values are tabulated of the optical properties for extinction, scattering, and asymmetry in both the visible and infrared. Each of those six properties are a function of three variables: the cloud core-to-mantle ratio (dust core, water ice mantle), the cross-section weighted size bin of the particle, and the wavelength bin of the particle.

4.2.2 MGCM radiative calculations

For a given timestep, the optical properties for all size bins and wavelength bins are used for calculations, while one core-to-mantle ratio value is used. The first step in the radiative calculations is to use water ice cloud properties (ice core mass, particle number, and water ice mass) to calculate a single cloud core-to-mantle ratio for the layer. There are 15 possible core-to-mantle ratio bins (or indices), ranging from a particle being primarily water to be primarily dust. The representative core-to-mantle ratio index is subsequently used to select the appropriate values for extinction, scattering, and asymmetry. Once this core-to-mantle ratio is calculated and the appropriate index selected, the model calculates a weighting coefficient across the 20 particle size bins. The weighting coefficient is the fraction of cloud particles at a given particle size bin; summing the coefficients across all 20 indices equals 1.

With the representative core-to-mantle ratio index chosen and the weighting coefficient calculated across all size bins, the cloud optical properties, or coefficients, can

now be calculated across all wavelengths. The optical coefficients Q_{ext}, Q_{scat}, and g, representing the extinction efficiency, scattering efficiency, and asymmetry parameter respectively, are calculated for visible and infrared wavelengths. The visible optical efficiencies are integrated over 7 wavelength bins and the infrared optical efficiencies are integrated over 5 wavelength bins. Optical coefficients are calculated with visible or infrared designations since they interact with matter in separate ways within the model.

The key point in this study is that the optical properties, which are calculated offline as described in Section 4.2.1, differ between the CLAPP and WARREN cases, resulting in different optical coefficients. A sample of how the values of optical coefficients are calculated is as follows:

$$Q_{ext(visible)} = \sum surf(i) * qextv(irap, i, iwav)$$

In this case, Q_{ext} for the visible value is summed across 20 particle size and 7 visible wavelength indices, where *surf* is the size bin weighting coefficient, *qextv* is the extinction parameter, *irap* is the selected core-mantle-ratio for cloud at this time step, *i* is the particle size index, and *iwav* is the wavelength index. The end result is that each layer has an extinction efficiency, a scattering efficiency, and an asymmetry parameter in both the visible and infrared wavelengths.

Once these optical coefficients are calculated they are used to determine the optical depth for each layer. The optical depth is also affected by additional factors such as water vapor and dust which remain identical between the WARREN and CLAPP cases. Finally, these values are used to calculate the radiative fluxes at each layer of the atmosphere, including the fluxes at the top of the atmosphere and at the surface. We refer to fluxes as either V for visible wavelengths, IR for infrared wavelengths, and T for the total of visible and infrared wavelength fluxes. Superscripts refer to the location of the flux value (*toa* for the top of atmosphere, *srf* for the surface, and *atm* for the total atmospheric energy budget, unlabeled for layers in the atmosphere) and subscripts referring to the directionality of the flux (*up* for upwards, *dn* for downwards, and *net* for the sum of upward and downward fluxes).

4.3 Results and Discussion

Refractive indices for the CLAPP case (130 K- 210 K) are normalized to the indices for the WARREN case (266 K) for the visible (Fig. 4.1) and infrared (Fig. 4.2) wavelengths. Since *Clapp and Miller* [1993] did not measure refractive indices at as many wavelengths as provided by *Warren* [1984], some indices are the normalized to 1, resulting is several of the bands overlapping at 1.0 on the y-axis. In most cases, indices for the CLAPP case have higher values than the WARREN case, which in general would increase scattering and absorption. The imaginary index values differ the most between the two cases in both the visible and infrared.

To demonstrate the possible magnitude of these differences, we calculate the differences in the absorption efficiency, by subtracting the scattering efficiency from the extinction efficiency, between the WARREN case and two end members of the CLAPP case. We consider a high altitude cloud at 0.5-2.5 mbar and a cloud at the lowest 2 mbar at the surface. We assume an effective cloud particle radius of 3 μm and a core-to-mantle ratio of 0.5, both values that frequently occur in the modeled water ice clouds. With both idealized scenarios, the absorption efficiency coefficient increases in the CLAPP case, with a 15% increase at 130 K and a 10% increase at 210 K, at the 8-12 μm infrared band within the model. As seen in Fig. 4.2, this band infrared band has the largest difference between the WARREN and CLAPP cases, so differences of 10-15% in absorption could be considered an upper limit for cloud particles of this size and composition ratio, but larger particles could have even larger differences in absorption with the CLAPP values.

4.3.1 Global energy budgets

The global radiative fluxes at the top and bottom of the atmosphere, and net changes in the atmospheric energy budget, are calculated for the WARREN and CLAPP cases. Because we are looking at two specific times of day at specific points during the year, we focus on differences between the WARREN and CLAPP cases since the total energy
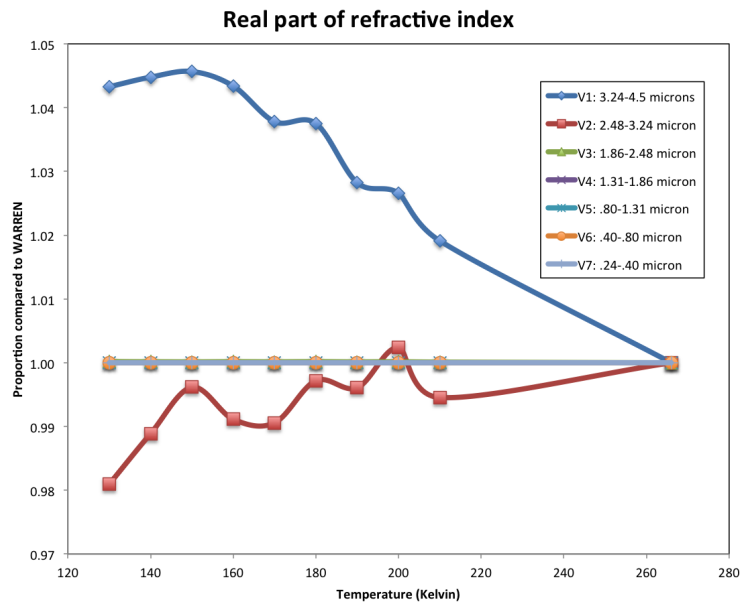
(a)
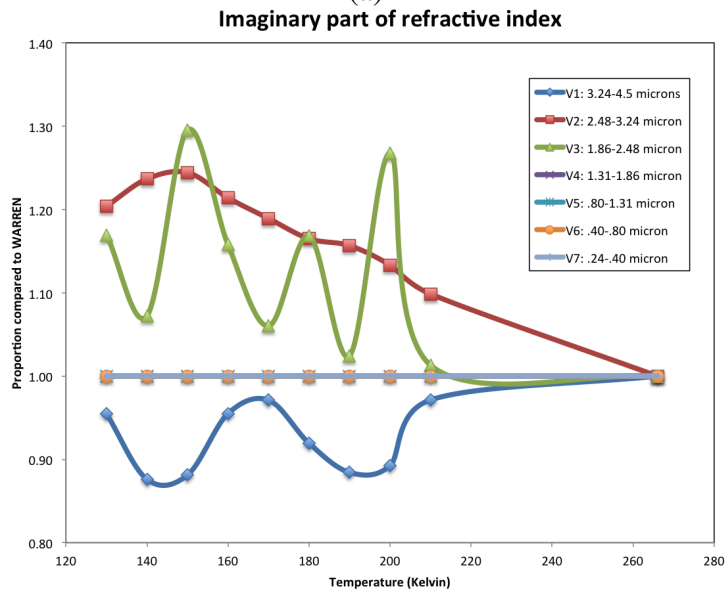
(b)

Figure 4.1: Refractive indices used to calculate optical properties used in the radiative transfer modeling of the water ice clouds. Values are shown for the seven visible wavelength bins used in the model. The WARREN case used the values at 266 K, and the CLAPP case used values at 130 K. Values are divided by the WARREN values for scale. (a) The real part of the refractive index, n, which influences particle scattering. (b) The imaginary part of the refractive index, k, which primarily influences absorption.
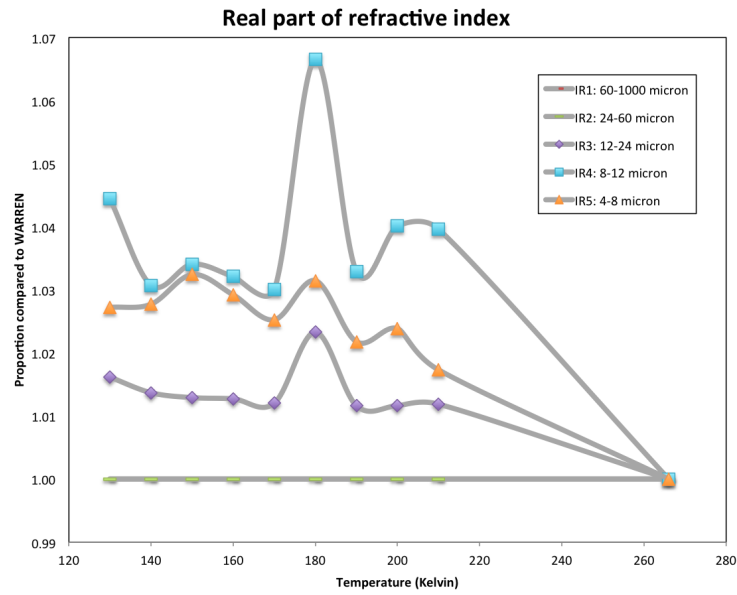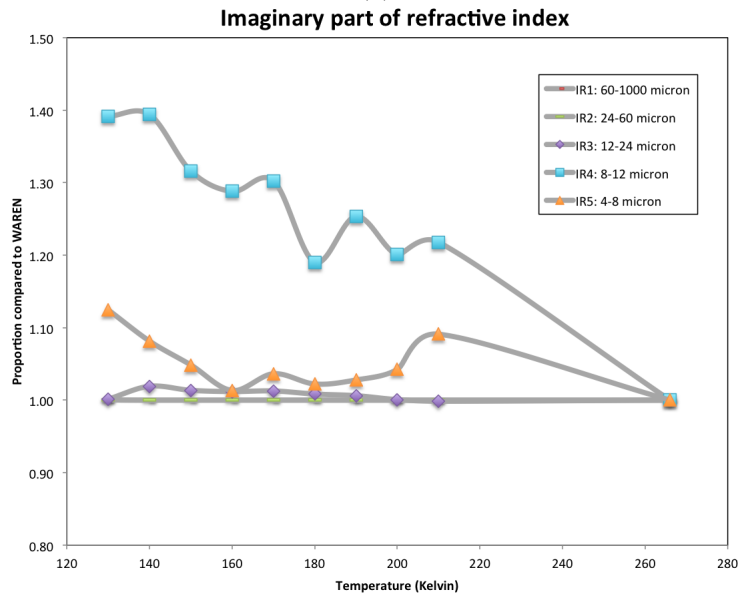
Figure 4.2: Refractive indices used to calculate optical properties used in the radiative transfer modeling of the water ice clouds. Values are shown for the five infrared wavelength bins used in the model. The WARREN case used the values at 266 K, and the CLAPP case used values at 130 K. Values are divided by the WARREN values for scale. (a) The real part of the refractive index, *n*, which influences particle scattering. (b) The imaginary part of the refractive index, *k*, which influences absorption.

budget of the atmosphere changes throughout the day. Differences between the cases at 2 PM are shown in Table 4.1. Fluxes from the model are calculated in Watts per square meter (W/m^2), and global values are calculated by multiplying fluxes for each grid cell by the surface area at that latitude. Differences and percent differences are calculated by subtracting WARREN from CLAPP values and dividing the differences by the absolute values from the WARREN case.

During the day, differences in the globally integrated T_{net}^{atm} between the WARREN and CLAPP cases are less than 1% for each of the four cardinal seasons (Table 4.1). The largest difference occurs at the Northern summer (L_s 90°), where there is a 0.35% increase in T_{net}^{atm} with the CLAPP case as compared to the WARREN case. At the spring and fall equinoxes (L_s 0° and 180°), the CLAPP case is 0.10% and 0.04% greater than WARREN for T_{net}^{atm}, while at the Northern winter solstice (L_s 270°) the CLAPP case is 0.09% lower than WARREN for T_{net}^{atm}.

However, at nighttime the differences in T_{net}^{atm} are much more apparent, as seen in Table 4.2 . The largest difference is seen at L_s 180°, with a 28% increase of energy into the atmosphere. L_s 0° and 90° showed a 23% and 15% increase in atmospheric energy, respectively, and L_s 270° actually had a decrease of energy into the atmosphere with a -2.5% change. The T_{net}^{toa} values at night are also large, with more downward forcing in the CLAPP case and T_{net}^{atm} differences of -2.1%, -1.2% and -2.8% at L_s 0°, 90°, and 180°, respectively. These values are are similar to the anthropogenic forcing attributed to well-mixed greenhouse gases like carbon dioxide on Earth [*Collins et al.*, 2006].

This work focuses on the changes at L_s 90° and 180° because of the larger presence of water ice clouds at these times. At L_s 90°, a large amount of water is sublimated from the North Polar Cap into the atmosphere, and a strong equatorial cloud belt develops [*Clancy et al.*, 2003]. A longitudinal-averaged zonal profile of simulated water ice cloud optical depth at L_s 90° is shown in Fig. 4.3 for 2 PM and indicates substantial water ice cloud formation over the equator and the North Pole. We also look at clouds optical effects at L_s 180° since this is time of year when the North polar hood is at its thickest [*Benson et al.*, 2011]. Because of the distribution of clouds at these seasons,

Global energy fluxes: % difference	Ls 0	Ls90	Ls180	Ls270
Net at surface (T_{NET}^{SRF})	**-0.07%**	**-0.21%**	**-0.10%**	**-0.13%**
Net surface down (T_{DN}^{SRF})	**-0.01%**	**-0.04%**	**-0.02%**	**-0.02%**
Visible Up at Surface (V_{UP}^{SRF})	–	–	–	–
Visible Down at Surface (V_{DN}^{SRF})	–	–	–	–
Infrared Up at Surface (IR_{UP}^{SRF})	–	–	–	–
Infrared Down at Surface (IR_{DN}^{SRF})	0.11%	0.38%	0.15%	0.17%
Net at top of atmosphere (T_{NET}^{TOA})	**-0.08%**	**-0.26%**	**-0.07%**	**-0.04%**
Net at top of atmosphere up (T_{UP}^{TOA})	**-0.03%**	**-0.09%**	**-0.03%**	**-0.01%**
Visible Up Top of Atm. (V_{UP}^{TOA})	0.01%	0.02%	0.02%	–
Infrared Up Top of Atm. (IR_{UP}^{TOA})	-0.05%	-0.13%	-0.05%	-0.02%
Net energy into atmosphere (T_{NET}^{ATM})	**0.10%**	**0.35%**	**0.04%**	**-0.09%**

North Pole energy fluxes: % difference	Ls 0	Ls90	Ls180	Ls270
Net at surface (T_{NET}^{SRF})	**-0.38%**	**-0.39%**	**-1.73%**	**-6.07%**
Net surface down (T_{DN}^{SRF})	**-0.09%**	**-0.16%**	**-0.41%**	**-42.58%**
Visible Up at Surface (V_{UP}^{SRF})	0.01%	0.02%	–	N/A
Visible Down at Surface (V_{DN}^{SRF})	0.01%	0.02%	–	N/A
Infrared Up at Surface (IR_{UP}^{SRF})	–	–	–	0.00%
Infrared Down at Surface (IR_{DN}^{SRF})	0.50%	0.72%	0.83%	42.58%
Net at top of atmosphere (T_{NET}^{TOA})	**1.34%**	**0.16%**	**-2.18%**	**-1.05%**
Net at top of atmosphere up (T_{UP}^{TOA})	**0.02%**	**0.05%**	**-0.11%**	**-1.05%**
Visible Up Top of Atm. (V_{UP}^{TOA})	0.04%	0.07%	0.06%	N/A
Infrared Up Top of Atm. (IR_{UP}^{TOA})	-0.01%	0.01%	-0.35%	-1.05%
Net energy into atmosphere (T_{NET}^{ATM})	**-0.68%**	**-9.45%**	**-1.30%**	**-43.04%**

Equatorial energy fluxes: % difference	Ls 0	Ls90	Ls180	Ls270
Net at surface (T_{NET}^{SRF})	**-0.43%**	**-0.48%**	**-2.06%**	**-5.72%**
Net surface down (T_{DN}^{SRF})	**-0.10%**	**-0.18%**	**-0.41%**	**-39.85%**
Visible Up at Surface (V_{UP}^{SRF})	0.02%	0.03%	0.01%	N/A
Visible Down at Surface (V_{DN}^{SRF})	0.02%	0.03%	0.01%	N/A
Infrared Up at Surface (IR_{UP}^{SRF})	–	–	–	0.00%
Infrared Down at Surface (IR_{DN}^{SRF})	0.53%	0.71%	0.86%	39.85%
Net at top of atmosphere (T_{NET}^{TOA})	**1.71%**	**0.12%**	**-1.61%**	**-1.04%**
Net at top of atmosphere up (T_{UP}^{TOA})	**0.02%**	**0.03%**	**-0.09%**	**-1.04%**
Visible Up Top of Atm. (V_{UP}^{TOA})	0.04%	0.07%	0.08%	N/A
Infrared Up Top of Atm. (IR_{UP}^{TOA})	-0.01%	-0.06%	-0.31%	-1.04%
Net energy into atmosphere (T_{NET}^{ATM})	**-0.74%**	**-5.82%**	**-2.82%**	**-40.41%**

Table 4.1: Differences in radiative fluxes between the WARREN and CLAPP cases at the cardinal seasons for 2 PM local time. North Pole fluxes are for 80°N and poleward. Net values sum visible and infrared sources. Percent differences are calculated by subtracting WARREN from CLAPP values and dividing the differences by the absolute values of the WARREN case. Dashed symbols indicate values that are below 0.01%.

Global energy fluxes: % difference	Ls 0	Ls90	Ls180	Ls270
Net at surface (T_{NET}^{SRF})	15.31%	8.17%	-21.72%	-2.64%
Net surface down (T_{DN}^{SRF})	21.19%	11.03%	25.21%	-2.58%
Visible Up at Surface (V_{UP}^{SRF})	–	–	–	–
Visible Down at Surface (V_{DN}^{SRF})	–	–	–	–
Infrared Up at Surface (IR_{UP}^{SRF})	–	–	–	–
Infrared Down at Surface (IR_{DN}^{SRF})	-21.19%	-12.15%	-25.21%	2.86%
Net at top of atmosphere (T_{NET}^{TOA})	-2.07%	-1.24%	-2.76%	0.04%
Net at top of atmosphere up (T_{UP}^{TOA})	-2.07%	-1.13%	-2.76%	0.03%
Visible Up Top of Atm. (V_{UP}^{TOA})	N/A	0.06%	N/A	–
Infrared Up Top of Atm. (IR_{UP}^{TOA})	-2.07%	-1.19%	-2.76%	0.03%
Net energy into atmosphere (T_{NET}^{ATM})	22.51%	14.57%	28.07%	-2.50%

North Pole energy fluxes: % difference	Ls 0	Ls90	Ls180	Ls270
Net at surface (T_{NET}^{SRF})	-2.93%	-0.78%	-0.53%	-11.81%
Net surface down (T_{DN}^{SRF})	-7.78%	-0.24%	-0.30%	-82.09%
Visible Up at Surface (V_{UP}^{SRF})	N/A	0.02%	N/A	N/A
Visible Down at Surface (V_{DN}^{SRF})	N/A	0.02%	N/A	N/A
Infrared Up at Surface (IR_{UP}^{SRF})	–	–	–	–
Infrared Down at Surface (IR_{DN}^{SRF})	7.78%	0.65%	0.30%	82.09%
Net at top of atmosphere (T_{NET}^{TOA})	-0.09%	1.41%	-0.30%	-1.91%
Net at top of atmosphere up (T_{UP}^{TOA})	-0.09%	0.07%	-0.30%	-1.91%
Visible Up Top of Atm. (V_{UP}^{TOA})	N/A	0.07%	N/A	N/A
Infrared Up Top of Atm. (IR_{UP}^{TOA})	-0.09%	0.05%	-0.30%	-1.91%
Net energy into atmosphere (T_{NET}^{ATM})	-7.40%	-1.43%	0.10%	-86.12%

Equatorial energy fluxes: % difference	Ls 0	Ls90	Ls180	Ls270
Net at surface (T_{NET}^{SRF})	-1.52%	-0.99%	-0.54%	-12.06%
Net surface down (T_{DN}^{SRF})	-4.27%	-0.31%	-0.23%	-82.37%
Visible Up at Surface (V_{UP}^{SRF})	N/A	0.02%	N/A	N/A
Visible Down at Surface (V_{DN}^{SRF})	N/A	0.01%	N/A	N/A
Infrared Up at Surface (IR_{UP}^{SRF})	–	–	–	–
Infrared Down at Surface (IR_{DN}^{SRF})	4.27%	0.79%	0.23%	82.37%
Net at top of atmosphere (T_{NET}^{TOA})	-0.07%	0.23%	-0.31%	-1.89%
Net at top of atmosphere up (T_{UP}^{TOA})	-0.07%	0.01%	-0.31%	-1.89%
Visible Up Top of Atm. (V_{UP}^{TOA})	N/A	0.07%	N/A	N/A
Infrared Up Top of Atm. (IR_{UP}^{TOA})	-0.07%	-0.11%	-0.31%	-1.89%
Net energy into atmosphere (T_{NET}^{ATM})	-3.93%	-1.25%	0.17%	-89.26%

Table 4.2: Differences in radiative fluxes between the WARREN and CLAPP cases at the cardinal seasons for 2 AM local time. North Pole fluxes are for 80°N and poleward. Net values sum visible and infrared sources. Percent differences are calculated by subtracting WARREN from CLAPP values and dividing the differences by the absolute values of the WARREN case. Dashed symbols indicate values that are below 0.01%.
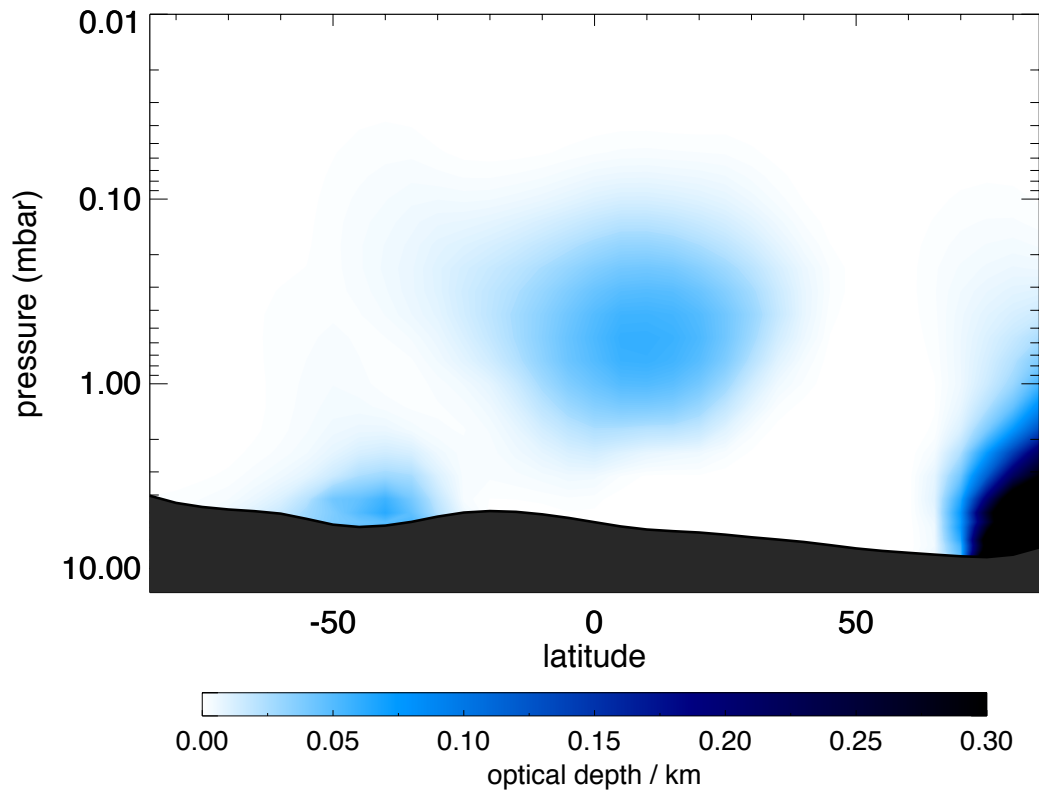
Figure 4.3: Longitudinally-averaged water ice cloud optical depth for the simulated climate of Mars at L_s 90°. The optical depth is calculated at the .4-.8 μm band, which is the wavelength interval at which there is peak solar emission.

we will focus on clouds at the equator (0°) and at the North Pole (85°).

A few key principles are illustrated throughout these results. Water ice clouds are Mars are generally optically thin [*Pearl et al.*, 2001]. Changes in cloud scattering properties can affect the redistribution of the energy upwards or downwards, but does not affect temperature in the atmosphere directly. Changes in the energy budget of the atmosphere itself must be due to absorption. The largest differences between the CLAPP and WARREN cases are seen in the infrared (Tables 4.1 and 4.2), particularly at night, emphasizing the importance in the temperature of clouds and at the surface in comparing the two cases. In the case of warm clouds over a cool surface, the clouds will lead to more radiation emitted toward the surface. Clouds that are cold relative to the atmosphere, a scenario particularly present with clouds that are higher in the atmosphere, are more likely to warm from surface emissions. We see both of these scenarios in the clouds we examine, and the CLAPP case serves to exacerbate already existing emissivity patterns. This is due to the higher values of the imaginary portion of the refractive index in the thermal infrared for CLAPP, which would result in more absorption, and thus also more emission, by water ice in the CLAPP case.

Looking at the changes in the energy balance at the atmospheric boundaries illustrates that scattering and absorption both play a role in the differences between the two cases. Fig. 4.4 shows the longitudinally-averaged differences between WARREN and CLAPP cases at 2 PM for T_{net}^{srf} and T_{net}^{toa} at L_s 90° and 180° at 2 PM, and Fig. 4.5 shows these differences at 2 AM. T_{net}^{srf} and T_{net}^{toa} are calculated by summing fluxes due to both visible and infrared sources. We use the sign convention of upward fluxes (towards the top of the atmosphere) having a positive value and downward fluxes (towards the surface) having a negative value. Thus a negative T^{toa} means the planet is gaining energy, and a negative T^{srf} means that the surface is warming. Differences between T_{net}^{srf} and T_{net}^{toa} in Figs. 4.4 and 4.5 for a given season are assumed to be due to differences in absorption, since the scattering differences between the two cases would equally impact the surface and top of atmosphere. During the day (Fig. 4.4), the differences in T_{net}^{srf} show mainly negative differences, indicating more energy is gained by the surface

Figure 4.4: Longitudinally-averaged differences between the WARREN and CLAPP cases at 2 PM, with the WARREN values subtracted from the CLAPP values. (a) Differences for T_{net}^{toa} at L_s 90°. (b) Differences for T_{net}^{srf} at L_s 90°. (c) Differences for T_{net}^{toa} at L_s 180°. (d) Differences for T_{net}^{srf} at L_s 180°.
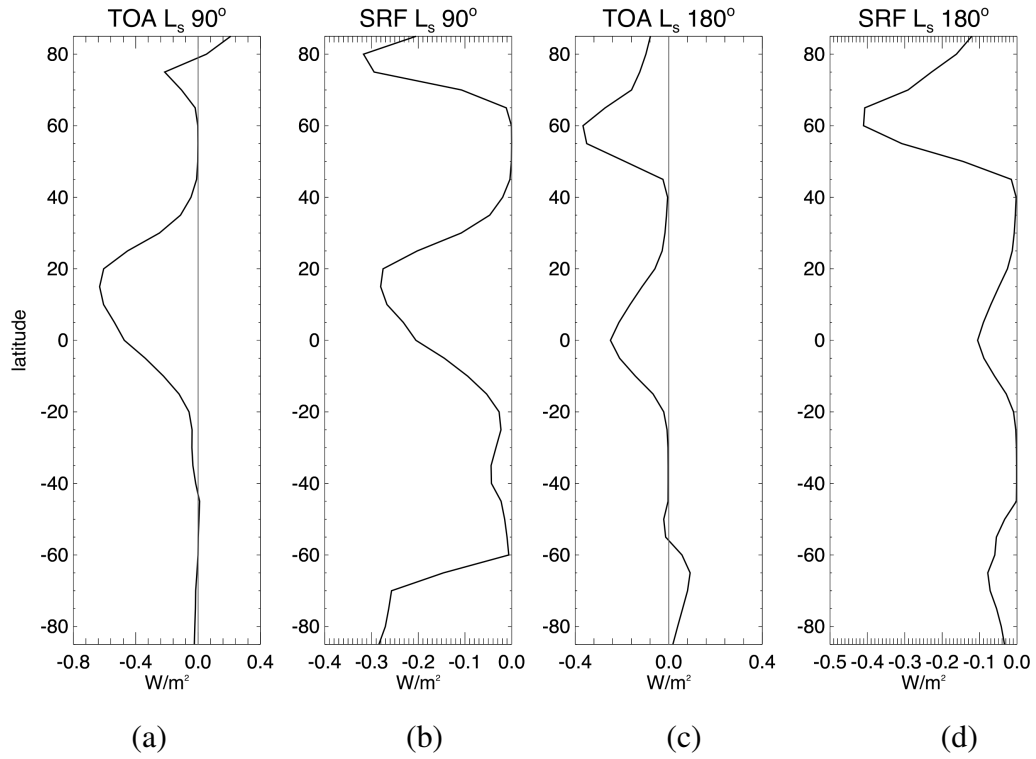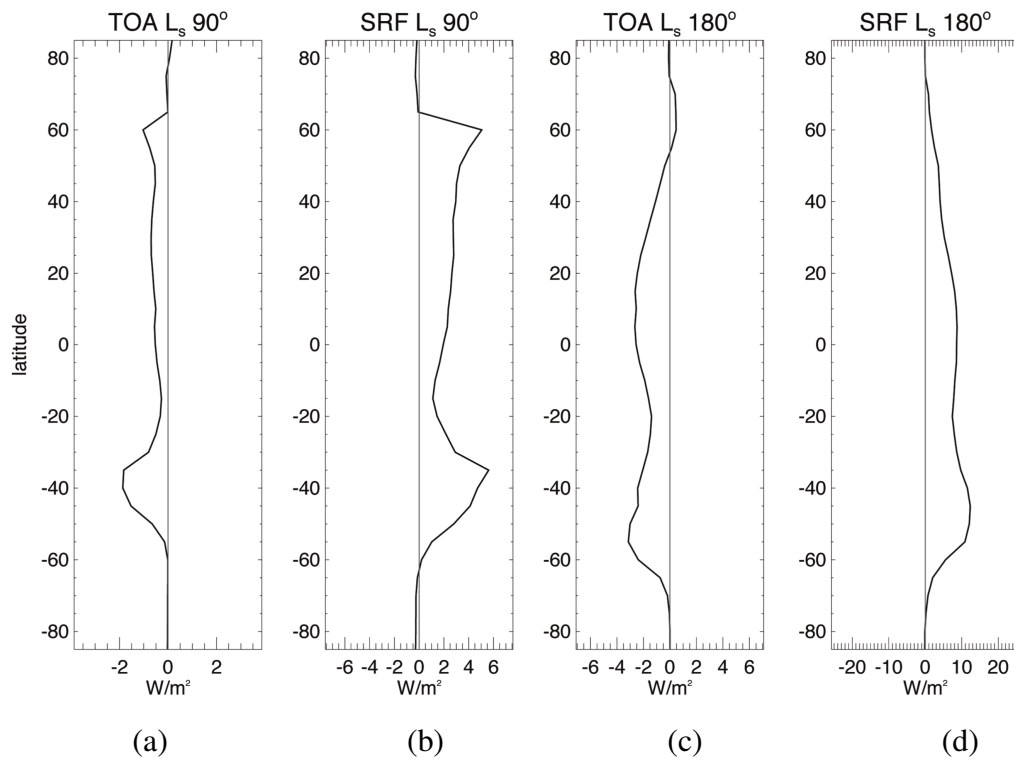
Figure 4.5: Longitudinally-averaged differences between the WARREN and CLAPP cases at 2 AM, with the WARREN values subtracted from the CLAPP values. (a) Differences for T_{net}^{toa} at L_s 90°. (b) Differences for T_{net}^{srf} at L_s 90°. (c) Differences for T_{net}^{toa} at L_s 180°. (d) Differences for T_{net}^{srf} at L_s 180°.

77

in the CLAPP case. Most differences are due to scattering as opposed to absorption, since the differences are similar between the boundaries of the atmosphere, but absorption does play a role since there is a discrepancy in the difference values between T_{net}^{srf} and T_{net}^{toa} at the equator for both L_s 90° and 180°. At night (Fig. 4.5), the differences between T_{net}^{srf} and T_{net}^{toa} for both seasons are much more noticeable, suggesting strong absorption of infrared energy by the clouds is much greater in the CLAPP case, as demonstrated by the 15% and 28% increases in atmospheric energy at L_s 90° and 180° respectively. While differences are seen at the South Pole, we do not examine those in detail since there are very few water ice clouds at this location and we do not believe that the differences seen in the model are physically realistic.

We examine the global differences between the two cases at L_s 90° in further detail. Changes in T_{net}^{atm} are found by subtracting T_{net}^{toa} from T_{net}^{srf}, with a net positive value reflecting an increase of energy into the atmosphere and a net negative value reflecting a loss of energy from the atmosphere. Looking at the 2 PM global differences in T_{net}^{atm} between the two cases at L_s 90°, in Fig. 4.6, using the more relevant temperature-dependent optical inputs of CLAPP results in amplification of warming at the equator and cooling at the poles. Similar global patterns are seen at the other cardinal seasons (not shown). At 2 AM for L_s 90°, these changes are larger by an order of magnitude, as shown in Fig. 4.7, with atmospheric warming concentrated to the transitional climate zones.

During the daytime, both visible and infrared radiative flux patterns differ between the WARREN and CLAPP cases, with the infrared changes playing a stronger role. Differences in V_{net}^{atm} and IR_{net}^{atm} between the two cases at 2 PM are shown in Fig. 4.8. The CLAPP clouds show an increased V_{net}^{toa}, particularly at the North Pole, and overall results in less visible light energy remaining in the atmosphere as seen in Fig. 4.8(a). These data suggest that the CLAPP clouds may be more reflective than the WARREN clouds. Differences between the CLAPP and WARREN cases are even more pronounced when looking at the differences in IR_{net}^{atm}, as seen in Fig. 4.8(b). The CLAPP case strengthens the existing warming in the equatorial region of the atmo-
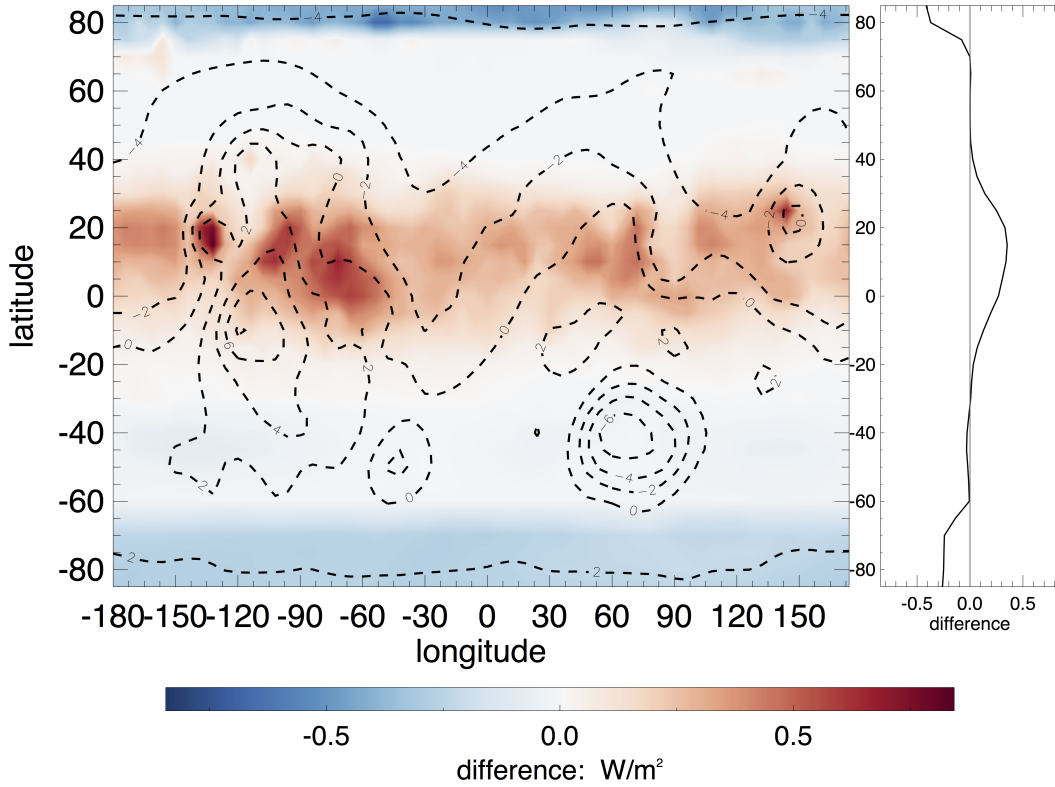
Figure 4.6: (Left) Global map of the differences in net changes to the atmospheric energy budget between the CLAPP and WARREN cases at L_s 90°. The dashed lines in both panes represent MOLA topography in km. Values are for instantaneous fluxes at 2PM local time, averaged over two days about L_s 90°. Positive values indicate more net warming of the atmosphere in the CLAPP case and negative values indicate more net cooling of the atmosphere in the CLAPP case. (Right) Longitudinally averaged differences.
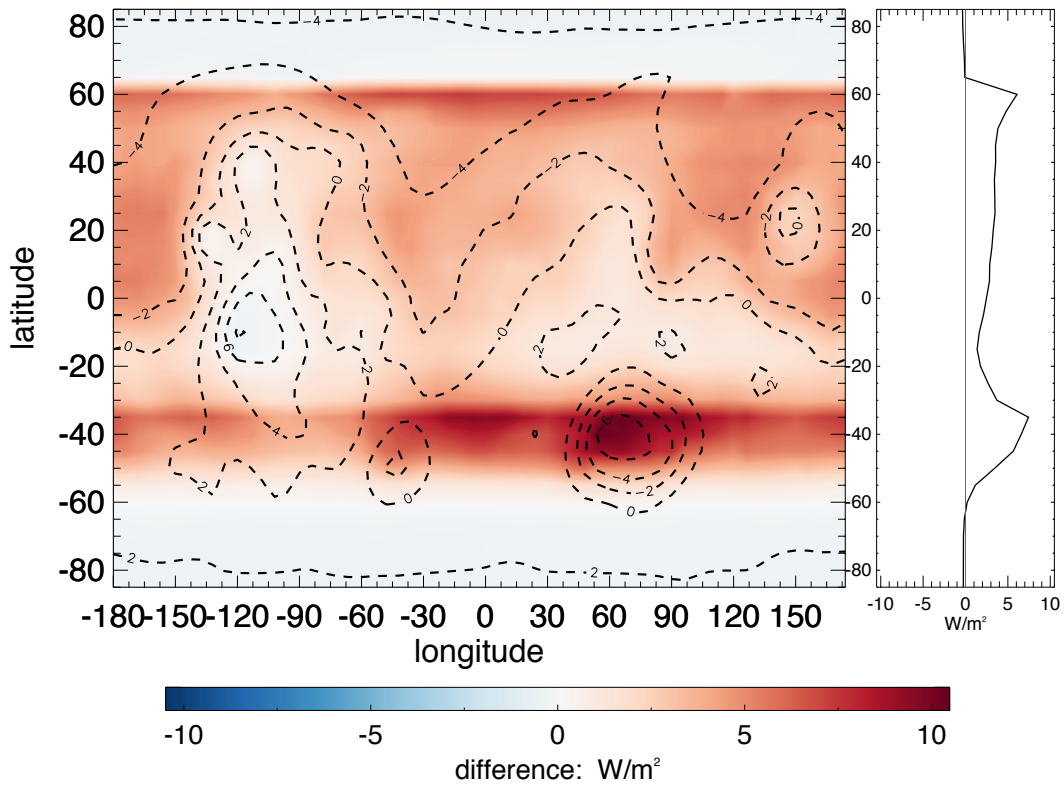
Figure 4.7: (Left) Global map of the differences in net changes to the atmospheric energy budget between the CLAPP and WARREN cases at L_s 90°. The dashed lines in both panes represent MOLA topography in km. Values are for instantaneous fluxes at 2AM local time, averaged over two days about L_s 90°. Positive values indicate more net warming of the atmosphere in the CLAPP case and negative values indicate more net cooling of the atmosphere in the CLAPP case. (Right) Longitudinally averaged differences.
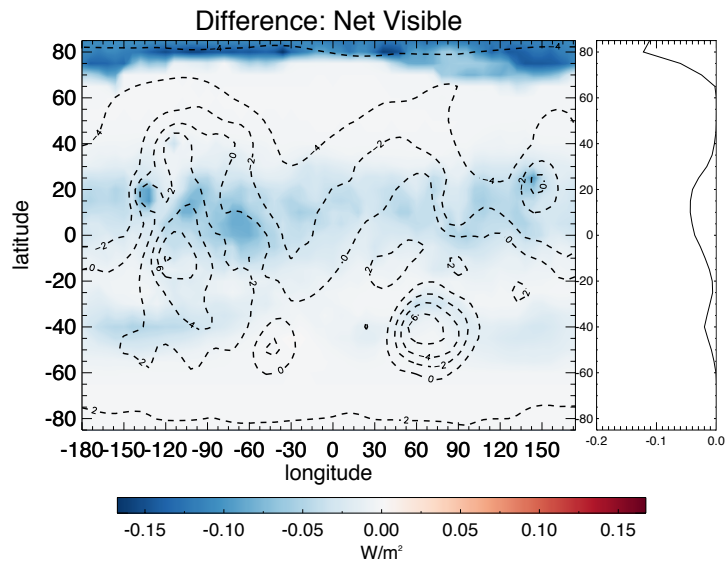
(a)
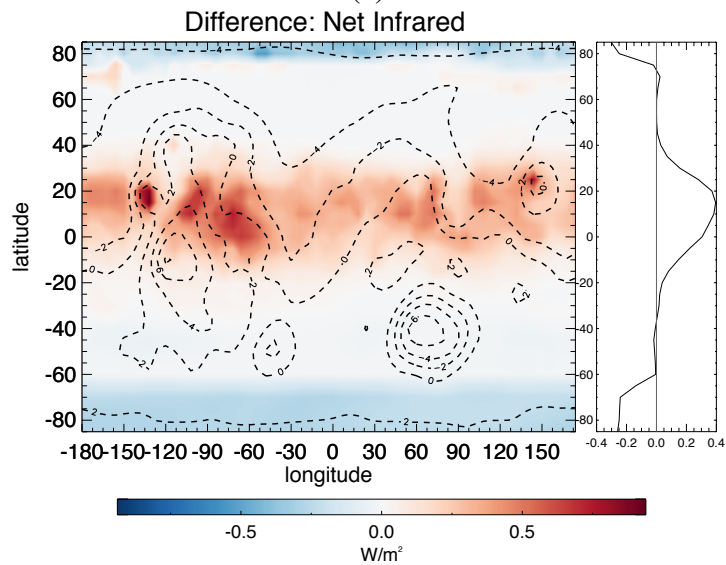
(b)

Figure 4.8: Global map of the differences in net changes of energy into the Martian atmosphere at L_s 90° between the CLAPP and WARREN cases, with WARREN values subtracted from the CLAPP values. Dashed lines represent MOLA topography in km. Values are for instantaneous fluxes at 2PM local time, averaged over two days about L_s 90°. Positive values indicate more energy into the atmosphere in the CLAPP case and negative values indicate less energy into the atmosphere in the CLAPP case. (a) Differences in the visible wavelengths, with zonally (longitudinally) averaged values on the right. (Right) (b) Differences in the infrared wavelengths, with zonally (longitudinally) averaged values on the right.

81

sphere by increasing the amount of infrared radiation retained by the atmosphere. Over most of the planet, the CLAPP case results in less infrared radiation being lost at the top of the atmosphere as compared to the WARREN case, while at the North Pole the CLAPP case loses slightly less infrared radiation than the WARREN case. At the surface, the CLAPP case has a larger negative IR_{net}^{srf}, meaning that clouds in the CLAPP case emit more energy into the surface than the WARREN case. This would result in surface warming and mean that the CLAPP clouds emit larger amounts of energy in the infrared. Fig. 4.2 shows that the CLAPP infrared indices are either equal to or greater than the WARREN indices, suggesting greater scattering and absorption occurs in the infrared. Overall, at 2 PM the CLAPP case loses more visible and infrared light energy compared to WARREN at the poles, but has increased energy at the equator, showing that the atmospheric energy gain is magnified at the equator in the CLAPP case. At 2 AM, differences in V_{net}^{atm} are negligible considering visible light only reaches the atmosphere in very small amounts at the North Pole, and differences in IR_{net}^{atm} show a similar geographic pattern as daytime IR_{net}^{atm} (not shown). We next examine the geographic differences in cloud radiative properties in more detail.

4.3.2 North Polar Cap

Differences in radiative fluxes between the WARREN and CLAPP cases at 80°N and poleward are shown in Tables 4.1 and 4.2. As with the global energy distribution patterns, both cases have similar overall patterns for radiative fluxes at the North Pole. At all times of year the energy differences between the CLAPP and WARREN cases at the North Pole are greater than the differences observed for the planet as a whole, emphasizing the sensitivity of the climate's energy budget to water ice clouds over the North Polar water ice cap. Nighttime differences in radiative fluxes are even greater than daytime fluxes. The largest difference in T_{net}^{atm} at the North Pole is at L_s 270°, with the CLAPP case having 86% less energy stay in the atmosphere in comparison with the WARREN case during the day and 43% less energy at night. However, since L_s 90° is the beginning of the peak of the water cycle, we focus on that season to examine the

82

impacts to the water cycle.

At the summer solstice, the CLAPP case loses -9.5% more energy from the atmosphere than does the WARREN case during the day; nighttime atmospheric energy loss is only -1.43%, but the T_{dn}^{srf} grows to a 0.78% change in downward flux which could hinder water deposition back onto the surface at night in the CLAPP case. The T_{dn}^{srf} (entirely IR) during the night actually increases by 82% in the CLAPP case, but most of that energy is re-emitted back into the atmosphere. The overall flux of energy into the surface is greatest during the daytime, due to increases of both V_{dn}^{srf}. and IR_{dn}^{srf}, with a larger IR_{dn}^{srf}, dominating the signal. We estimate the possible impact of this increase of T_{dn}^{srf}, assuming water ice clouds with the radiative properties of the CLAPP case. 4.6×10^{11} additional Watts (or J/s) of energy are assumed to fall onto a water ice surface for this area 80 and poleward in the CLAPP case. The amount of water that could be liberated with this excess of energy would be $\sim 1.4 \times 10^6$ kg of water per second. The CLAPP case would thus result in increasing the sublimation flux by 0.4% at the North Pole, a small direct perturbation to the global atmospheric water budget.

We look at atmospheric profiles of radiative fluxes for the CLAPP and WARREN cases to understand how the water ice clouds in both cases are influencing the energy budgets at the boundary layers. For atmospheric profiles, data is for the given latitude averaged over $\pm 5°$ of the designated latitude, in accordance with the model resolution. As with the global surface and top of atmosphere radiative flux distributions, both CLAPP and WARREN have similar overall patterns in the distribution of energy. A sample of what the overall energy flux patterns look like during the day is seen in Fig. 4.9, which shows the fluxes in the atmosphere at L_s 90° at 85° N for the CLAPP case at 2 PM; the WARREN case is very similar at the scales shown and not shown here. Solid lines show downward fluxes, which are negative, and dashed lines represent upward fluxes, which are positive. The solid black line shows the net change in atmospheric fluxes. We also calculate differences in projected atmospheric heating rates between the CLAPP and WARREN cases using the radiative flux profiles.

The differences in fluxes and projected atmospheric heating rates at 2 PM between
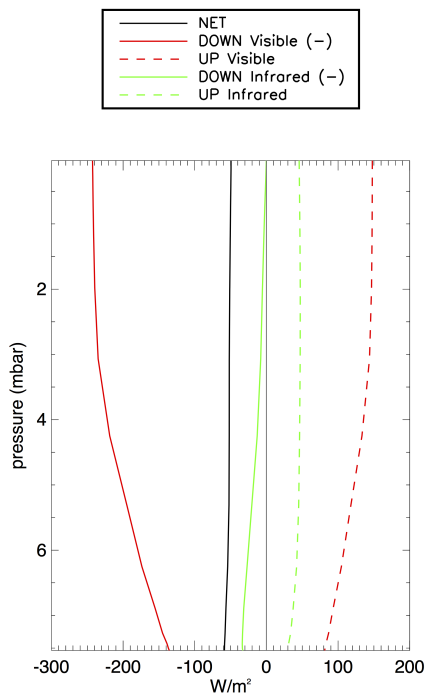
Figure 4.9: The zonally averaged radiative fluxes in the atmosphere for the CLAPP case at 85N at L_s 90. The WARREN case has very similar flux patterns, with the differences shown in Fig. 4.10(c). Upward fluxes have positive values and downward values have negative values. The light grey line represents zero for clarity.

the CLAPP and WARREN cases at L_s 90° at the North Pole are seen in Fig. 4.10, along with cloud properties and the atmospheric temperature profile. Nighttime values are extremely similar and not shown. The cloud is most dense near to the surface, with cloud particle radii of $\sim$3 μm, and the atmospheric temperature at the clouds is warmer than at the surface. Net negative differences indicate increased radiative flux downwards near the surface in the CLAPP case, and an increased flux upwards higher in the atmosphere, also seen in Fig. 4.4a and b. The CLAPP case has a slightly larger V_{dn} compared to WARREN, and a larger V_{up} as compared to WARREN, suggesting that the CLAPP optical parameters lead to clouds that are reflecting more visible light or that less visible light is absorbed and emitted in the infrared. In fact, the largest difference between the CLAPP and WARREN cases is in the infrared: The CLAPP case greatly increases the (negative) IR_{dn}, particularly at lower altitudes where water ice clouds may form. The relatively warm clouds close to the surface emit infrared radiation to the surface and also increase backscatter of infrared toward the surface, with this effect exacerbated in the CLAPP case. This is seen by the -0.39% change in T_{net}^{srf} at 2 PM and -0.78% change in T_{net}^{srf} at 2 AM (Tables 4.1 and 4.2), with the negative values indicating more energy going downward toward the surface in the CLAPP case. The CLAPP case would result in a relative warming of the surface, as well a decrease the heating rate of the atmosphere above the surface. Overall, during the Northern hemisphere summer solstice, the CLAPP case would lead to increased atmospheric cooling within low altitude clouds at the North Pole. While the negative heating rate change is not very large, it could result in positive feedbacks on cloud formation. If the CLAPP case results in cooler clouds, the vapor pressure would decrease, which would increase the cloud nucleation and growth rates.

The daytime differences in fluxes and projected atmospheric heating rates between the CLAPP and WARREN cases at L_s 180° at the North Pole are seen in Fig. 4.11; nighttime values are extremely similar and are not shown. Both 2 PM and 2 AM atmospheric temperature profiles do not have large gradients, aside from some warming nearing the surface. The clouds are thickest near the surface and have particle radii near-

85
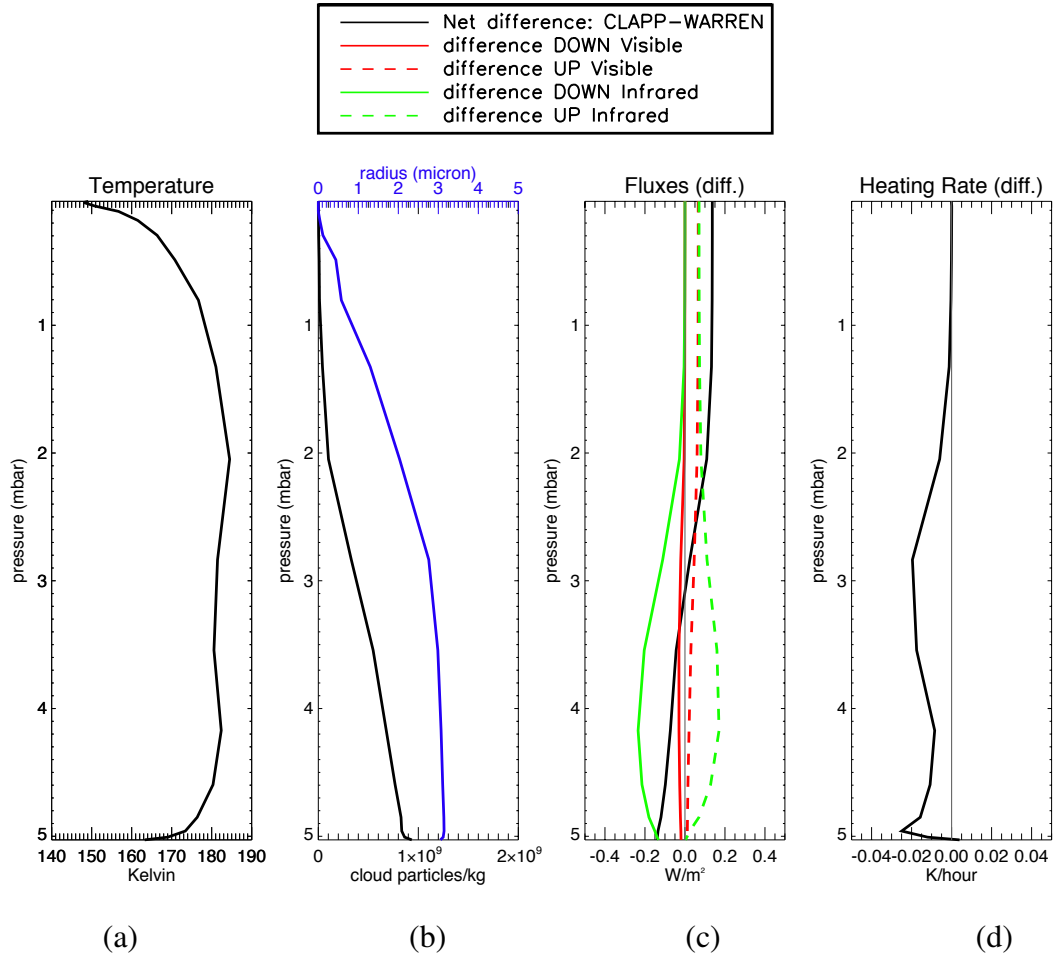
Figure 4.10: Atmospheric properties as a function of pressure at 2PM at 85N at L_s 90. (a) Atmospheric temperature profile, both cases have identical values for a given time and location. (b) The number of cloud particles/kg atmosphere and the effective radius of the cloud particles (μm), which are identical between cases. (c) Differences in the radiative fluxes in the atmosphere between the CLAPP and WARREN cases, with the WARREN case subtracted from the CLAPP case. The net difference is seen in black, and the light grey line represents zero for clarity. (d) The difference in heating rate between the CLAPP and WARREN cases, showing an increase in cooling with the CLAPP case.
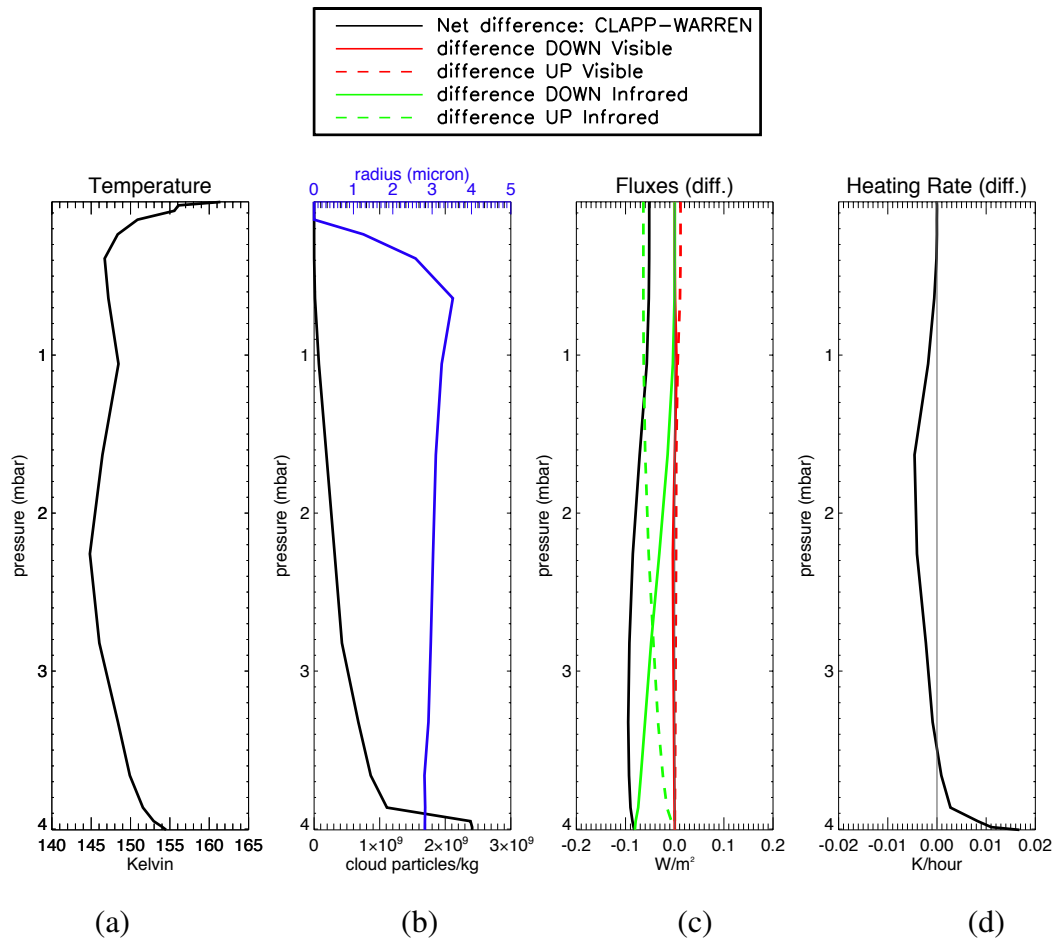
Figure 4.11: Same as Fig. 4.10, but at 85N at L_s 180 at 2 PM.

ing 4 μm for both times of time. At this time of year, the CLAPP case shows minimal differences at 2PM in visible fluxes up or down as compared to the WARREN case, but does show a larger difference in the infrared fluxes. CLAPPS's IR_{dn} become increasingly stronger than WARREN's near the surface, while IR_{up} for CLAPP is stronger up towards the top of the atmosphere. Overall, CLAPP has a larger T_{dn} than the WARREN case during both day and night, which would result in slight cooling in most of the atmosphere when compared to WARREN, except for very close to the surface.

4.3.3 Equatorial Cloud Belt

At both L_s 90° and 180° at 2PM, the CLAPP case has a larger negative T_{net}^{toa} than T_{net}^{srf} at the equator (Fig. 4.4), indicating that absorption plays a stronger role in equatorial cloud behavior in the CLAPP case during the day. This is apparent when looking at atmospheric profile data at the equator for both of these seasons. The 2 AM T_{net}^{toa} and T_{net}^{srf} values (Fig. 4.5) also lead to increases in energy of the atmosphere of even greater magnitudes, but the peak changes in energy are not over the equator and are between the tropics and the poles.

The daytime differences in fluxes and projected atmospheric heating rates between the two cases at L_s 90° for the equator are seen in Fig. 4.12. The daytime clouds are at a higher altitude and cooler than the clouds at the North Pole at this time of year, and the surface is warmer than the clouds, a scenario where the clouds would net gain energy from the surface. The particles are slightly larger than at the North Pole, with larger effective radii $\sim$3.5 μm. The CLAPP case results in less IR_{up} in the upper atmosphere, showing an increase in the radiative warming at the aphelion cloud belt and suggesting increased absorption at these high altitude clouds. This would lead to minimal differences in heating at the surface between the CLAPP and WARREN case. Nighttime fluxes are seen in Fig. 4.13. While the clouds are thinner at higher altitudes, there is some level of cloud throughout the column, which results in warming near the surface an order of magnitude larger than with the daytime case. Fig. 4.14 shows the heating rates and differences between the two cases at 2 AM, and shows warming
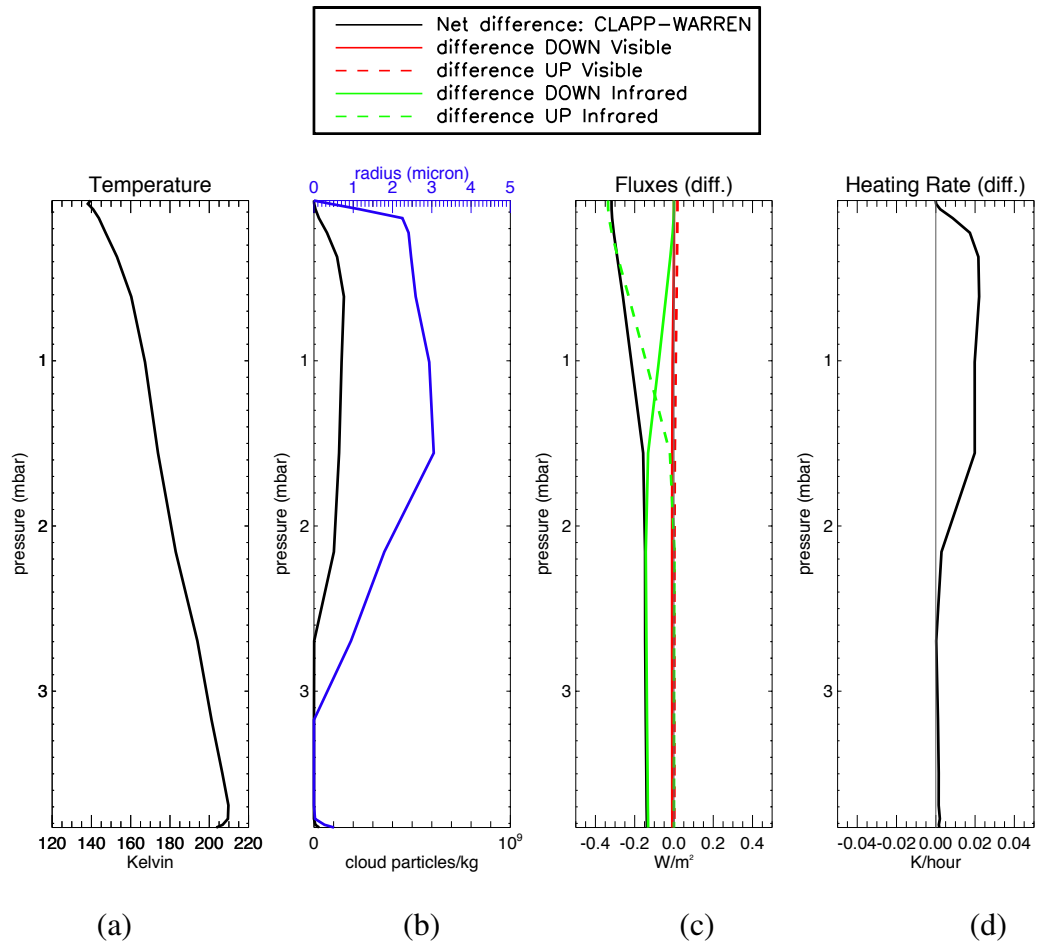
Figure 4.12: Same as Fig. 4.10, but at the equator at L_s 90 at 2 PM.
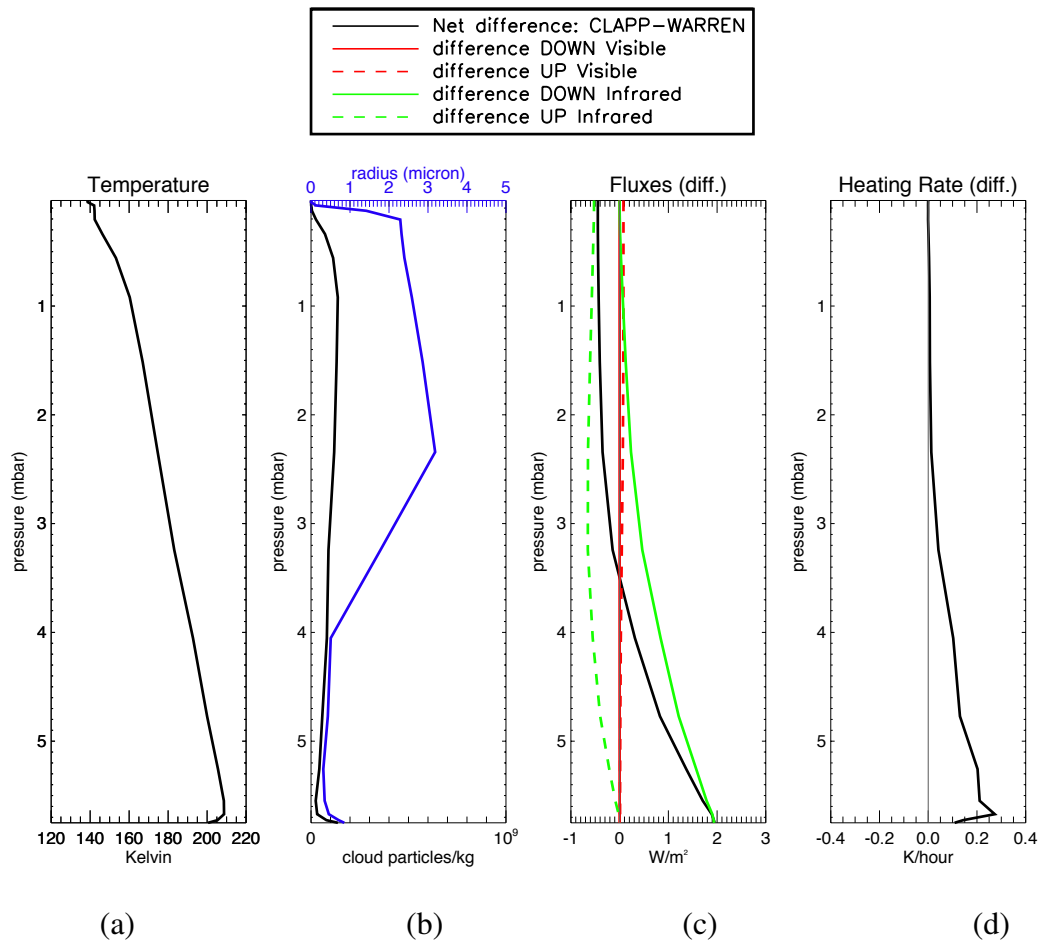
Figure 4.13: Same as Fig. 4.10, but at the equator at L_s 90 at 2 AM.

Figure 4.14: Heating rates and difference at 2 AM for L_s 90° for the equator. (a) WAR-REN heating rate. (b) CLAPP heating rate. (c) Difference in heating rate, calculated by subtracting WARREN from CLAPP and dividing by the absolute value of WARREN.
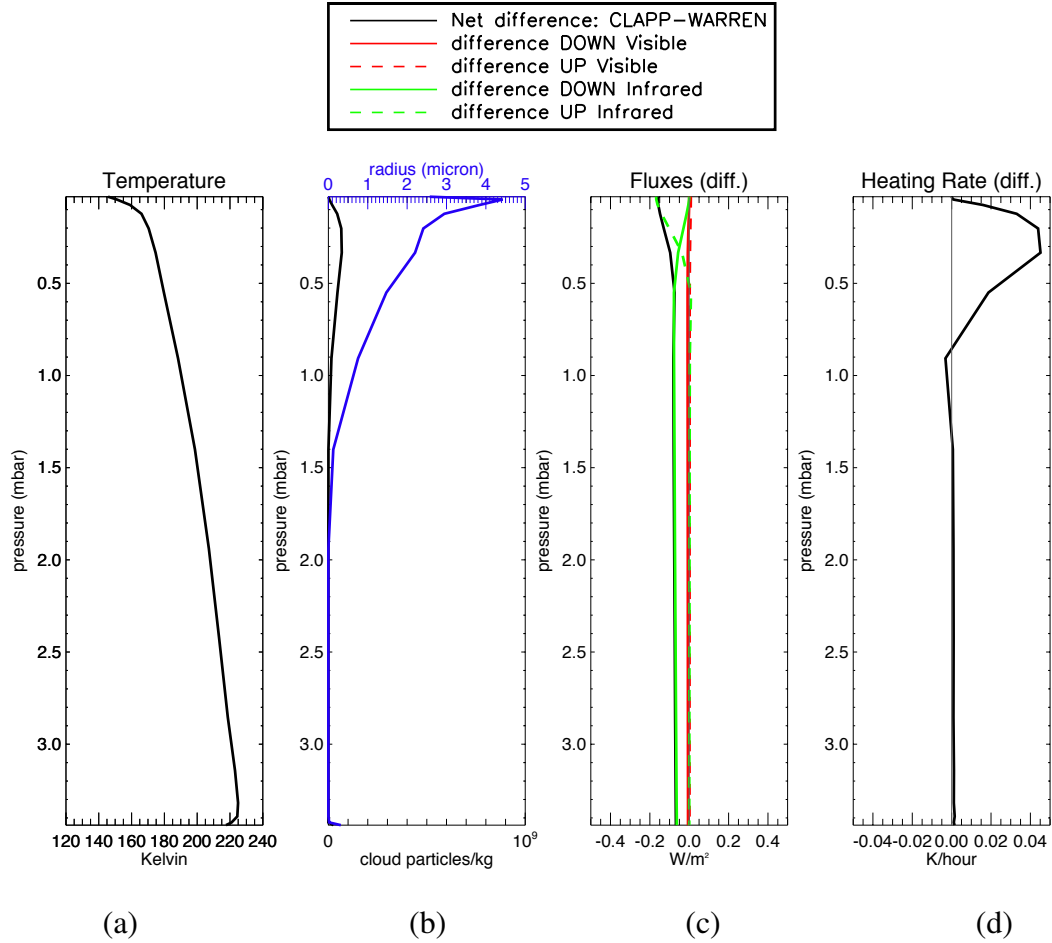
Figure 4.15: Same as Fig. 4.10, but at the equator at L_s 180 at 2 PM.

near the surface increased up to 5% in the CLAPP case. Overall, during the Northern hemisphere summer solstice, the CLAPP case would lead to increased atmospheric warming within the aphelion cloud belt during the day over the equator and warming near the surface during the night over the equator.

Differences in fluxes and projected atmospheric heating rates between the two cases at L_s 180° at the equator are seen in Fig. 4.15 for 2 PM and in Fig. 4.16. As with the equatorial clouds at L_s 90°, the atmosphere cools linearly with height and cloud increase in thickness near the top of the atmosphere for both day and night. While the clouds
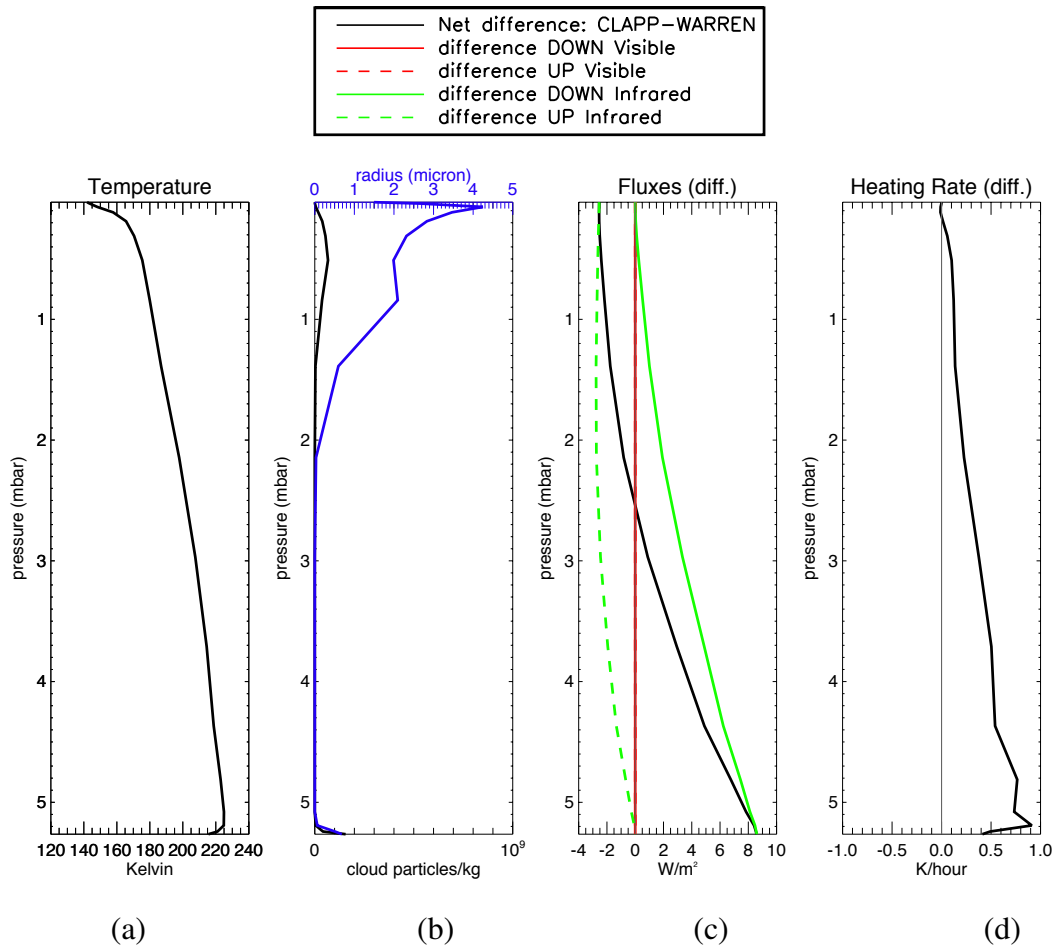
Figure 4.16: Same as Fig. 4.10, but at the equator at L_s 180 at 2 AM.

are less dense than other times and locations examined, the particle sizes are slightly larger at around 4.5 μm at the top of the atmosphere. During the day, the CLAPP and WARREN cases mainly differ in the upper atmosphere in the infrared, where clouds in the CLAPP case have less IR_{up} in the atmosphere, which results in the CLAPP clouds having a higher heating rate in the upper atmosphere. This pattern is similar to the aphelion cloud effects seen at L_s 90°. The nighttime effect is similar to the aphelion cloud effects seen at L_s 90°, as well. Infrared emissions from the surface dominate the signature at night, with warming near the surface up to 1 K/hour; within a few hours, a heating rate like this could drive new convective patterns. The differences in heating between CLAPP and WARREN at night, shown in Fig. 4.17, show that heating rates could increase by up to 45% in the lower middle half of the atmosphere with the CLAPP case.

4.4   Conclusions

Using temperature-dependent refractive indices relevant to the temperatures of water ice clouds on Mars results in the amplification of existing radiative flux trends that would affect both surface and atmospheric temperatures. Changes in both the visible and infrared wavelengths occur, with infrared changes dominating the differences seen between the CLAPP and WARREN cases. Globally, infrared atmospheric warming would be amplified by using the more temperature-appropriate CLAPP optical parameters, except during perihelion. At the North Pole, the atmosphere would generally emit more infrared radiation with the CLAPP case, though some of this energy would result in a larger flux downward at the surface.

Using more appropriate temperature-dependent refractive indices for water ice cloud optical parameters affects the radiative transfer of the clouds by changing both scattering and absorption. This work suggests that radiatively active water ice clouds may have more scattering than previously thought, which could warm or cool the surface depending on the location and thickness of the cloud. At the highly reflective North
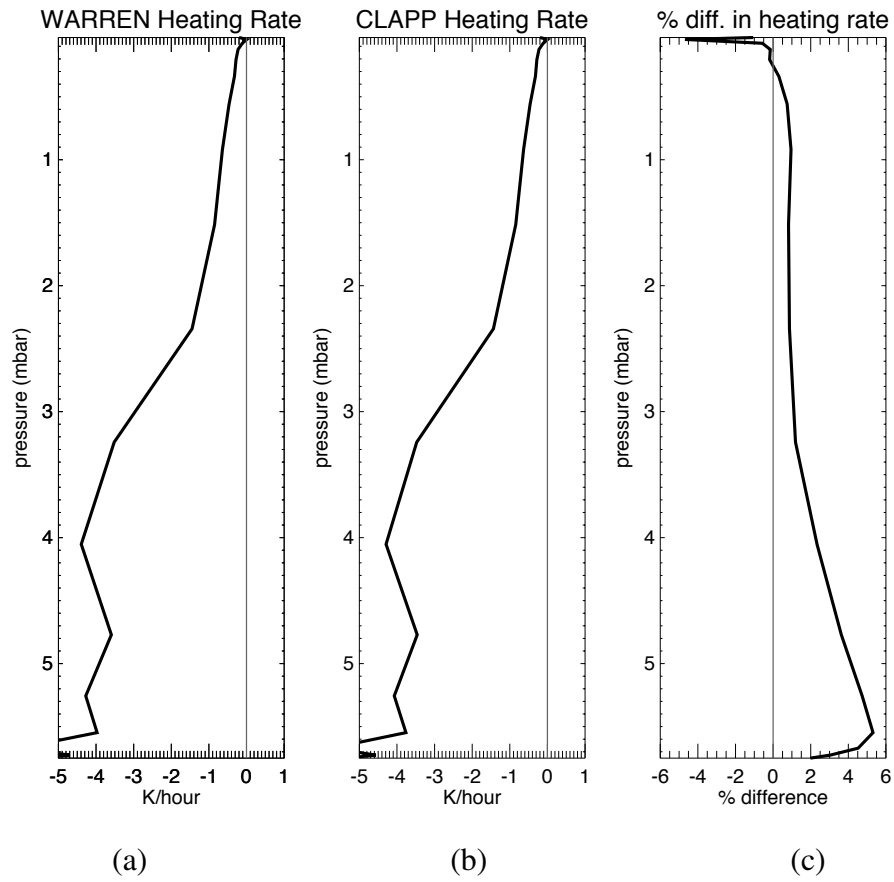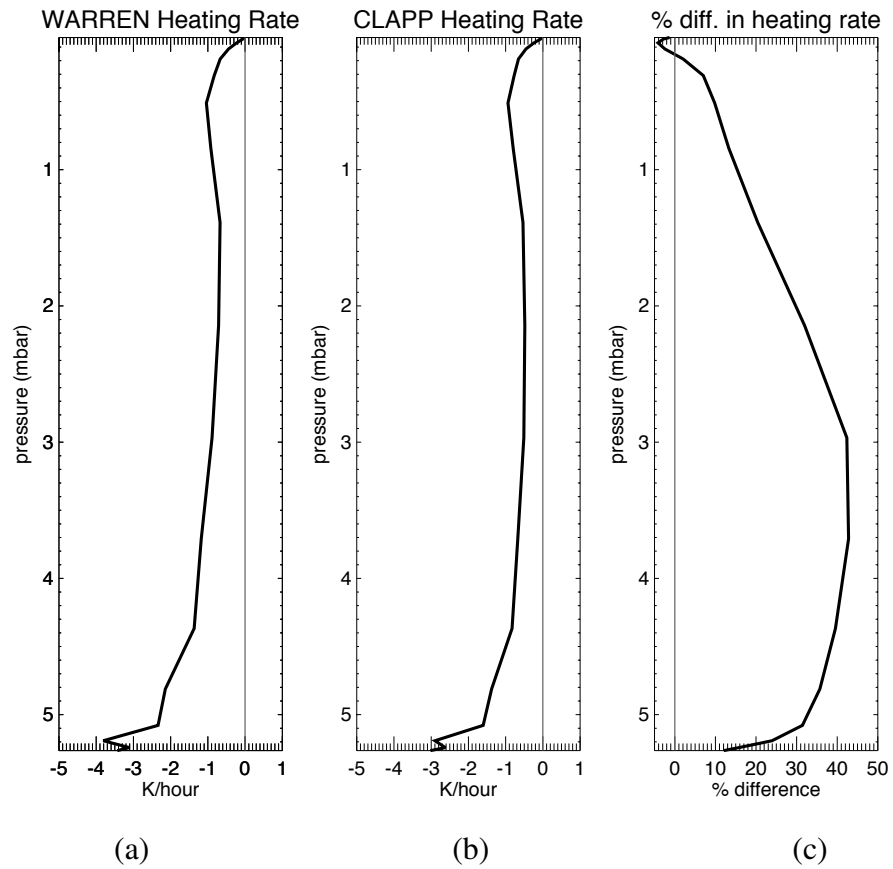
Figure 4.17: Heating rates and difference at 2 AM for L_s 180° for the equator. (a) WAR-REN heating rate. (b) CLAPP heating rate. (c) Difference in heating rate, calculated by subtracting WARREN from CLAPP and dividing by the absolute value of WARREN.

Polar Cap, clouds could warm the surface by backscattering energy reflected from the high albedo surface that would normally pass through the clouds and out of the planet. These polar clouds in the CLAPP case may scatter light more effectively back toward the surface, which would lead to increased energy uptake at the surface and cooling of the atmosphere. A positive feedback on the cloud radiative effects could occur. The aphelion cloud belt has larger particles which may forward scatter more effectively [*Clancy et al.*, 2003]. This work suggests that scattering in the infrared by these larger cloud particles, as well as increased absorption using CLAPP optical parameters, could lead to increased warming in those equatorial clouds. While warming would occur where clouds form during the day to achieve a stabilizing effect, the differences in heating rate between WARREN and CLAPP are most pronounced during the night at the equator, when increases of warming up to 45% can occur at L_s 180° in the lower half of the atmosphere. The warming closer to the surface at night could lead to increased atmospheric instabilities at the equator, which could lead to changes in cloudiness and thus in the climate.

Future work should examine how the changes in the CLAPP case would affect cloud evolution and the climate in a full 3D climate simulation. Clouds over the cap could lead to more atmospheric cooling and surface warming, which together could increase cloud formation and further amplify the effects of the CLAPP case. Changes in atmospheric dynamics at the equator will also require additional examination with new temperature-dependent optical properties, as the differences in how daytime and nighttime temperatures change along the atmospheric column could alter the temperature structure of the atmosphere at the equator.

Chapter 5

Summary

The research presented in this dissertation furthers the understanding of the formation and impacts of water ice clouds on Mars. This work closely examines two important topics related to the Martian water ice clouds, namely, cloud formation and radiative effects. Chapters 2 and 3 examine the initiation of water ice clouds on Mars, a process that varies depending on cloud type and nucleation source material, while Chapter 4 tests the variability of the modeled radiative effects of these clouds with temperature. The atmospheric water cycle on Mars is very sensitive to water ice clouds, and this work demonstrates that small changes in how water ice clouds form and behave optically can have a significant impact on these clouds and in turn, their impact on overall climate.

This work is accomplished through a combination of modeling and laboratory experiments. Climate modeling is an important tool in furthering our understanding of Martian climate because of the stochastic nature of climate as well as our relatively limited ability to observe it compared to Earth, despite a plethora of mission data. Additionally, modeling allows us to directly probe the underlying physics and characterize the consequences of altering different parameters. In Chapters 2 and 4, 3D climate modeling is used to explore cloud formation, evolution, and radiative effects. Laboratory experiments are essential for elucidating some the fundamental concepts of cloud

microphysics. They provide the foundation for understanding theory and observations and often are the primary source for the parameterization of physical properties. In Chapter 3, experiments build upon earlier research used to extrapolate water ice nucleation patterns into lower pressure and temperature ranges that are more relevant to Mars. Additionally, this work identifies salts, specifically perchlorates as a promising substrate for water ice nucleation.

The work in Chapter 2 identifies that the specific nucleation mechanisms at the polar caps and at the equator are distinct and either require different nucleation schemes or additional levels of control in order for nucleation to initiate within the model. While some of the differences in cloud formation between these locations cannot be discerned with current observations, one large discrepancy can be explored by looking to Earth cloud research. Better understanding the difference between nucleation behavior in convective versus stratiform clouds on Earth can contribute to further understanding how these different types of clouds form on Mars.

In Chapter 3, sodium perchlorate is identified as a substrate that nucleates water ice at substantially lower levels of water vapor than other substrates. A major implication of this is that water ice cloud formation could vary greatly depending on location and what surface materials are lofted into the atmosphere. Water ice clouds could form in drier regions of the atmosphere than we currently project if sodium perchlorate is present. Future work can assess the relative ease of nucleation of sodium perchlorate in comparison to other substrates on Mars, as well as use the calculated contact parameters in climate models to determine the impact of the presence of sodium perchlorate on water ice nucleation patterns. Differences in substrate contact parameters are currently absent in climate models, and a long term goal of this work would be to introduce them and evaluate their effects on the Martian water cycle.

Chapter 4 explores how the introduction of more physically-realistic temperature-dependent optical parameters suggests that the radiative effects of water ice clouds on Mars are largely misrepresented in climate models. Infrared differences dominate the changes seen with the updated optical parameters, with either warming or cooling

effects in the atmosphere depending on cloud altitude and temperature relative to the surface. At the equator, nighttime atmospheric heating rate changes of up to 1 K/ hour are projected; changes of this magnitude could lead to altered dynamics. At the pole, increased energy fluxes would lead to surface warming. The atmospheric energy budget changes at night could be very large, with the new optical parameters leading to a 15% and 28% increase of atmospheric energy at L_s 90° and 180°, respectively. Future work shall incorporate the optical parameters for colder water ice into a full 3D climate model and include feedbacks, which will more appropriately warm or cool the atmosphere and surface and allow for a better understanding of the energy balance of the Martian atmosphere. This is expected to enhance atmospheric instability in some places, while stabilizing the atmosphere elsewhere. Over the North Pole, cloud formation would be expected to increase with cooler temperatures and the optical effects would increase.

This thesis builds on a substantial body of knowledge about water ice clouds on Mars, and isolates processes that impact cloud formation as well as the overall climate of the planet. This work also combines different bodies of knowledge, such as Earth water cloud processes and modeled Martian climate, as well as Martian surface mineralogy with nucleation processes, to bring new approaches to existing scientific problems. Much work remains in the realm of understanding water ice clouds on Mars, in both the laboratory and in modeled space, and water ice clouds remain a familiar yet enigmatic presence on the planet.

Bibliography

Albee, A. L., F. Palluconi, and R. Arvidson, Mars global surveyor mission: overview and status, *Science*, *279*(5357), 1671–1672, 1998.

Allen, C., K. Jager, R. Morris, D. Lindstrom, M. Lindstrom, and J. Lockwood, JSC Mars-1: A Martian soil simulant, in *SPACE 98*, edited by Galloway, RG and Lokaj, S, pp. 469–476, 6th International Conference and Exposition on Engineering, Construction, and Operations in Space (Space 98), Albuquerque, NM, APR 26-30, 1998, 1998.

Allen, C. C., R. V. Morris, D. J. Lindstrom, M. M. Lindstrom, and J. P. Lockwood, JSC Mars-1 - Martian regolith simulant, in *Lunar and Planetary Science Conference*, *Lunar and Planetary Inst. Technical Report*, vol. 28, 1997.

Angus, S., B. Armstrong, and K. de Reuck, Iupac international thermodynamic tables of the fluid state, in *Carbon Dioxide*, vol. 3, Pergamon Press New York, 1976.

Arvidson, R. E., et al., Overview of the spirit mars exploration rover mission to gusev crater: Landing site to backstay rock in the columbia hills, *Journal of Geophysical Research: Planets*, *111*(E2), doi:10.1029/2005je002499, 2006.

Baker, V., Water and the martian landscape, *Nature*, *412*(6843), 228–236, doi:10.1038/35084172, 2001.

Beck, P., A. Pommerol, B. Schmitt, and O. Brissaud, Kinetics of water adsorption on

minerals and the breathing of the Martian regolith, *Journal of Geophysical Research: Planets*, *115*, doi:{10.1029/2009JE003539}, 2010.

Benson, J. L., D. M. Kass, and A. Kleinböhl, Mars' north polar hood as observed by the mars climate sounder, *Journal of Geophysical Research: Planets*, *116*(E3), 2011.

Bibring, J., et al., Perennial water ice identified in the south polar cap of Mars, *Nature*, *428*(6983), 627–630, doi:10.1038/nature02461, 2004.

Boxe, C. S., K. P. Hand, K. H. Nealson, Y. L. Yung, A. S. Yen, and A. Saiz-Lopez, Adsorbed water and thin liquid films on Mars, *International Journal of Astrobiology*, *11*(3), 169–175, doi:10.1017/S1473550412000080, 2012.

Carr, M. H., and J. W. Head, III, Geologic history of Mars, *Earth and Planetary Science Letters*, *294*(3-4, SI), 185–203, doi:10.1016/j.epsl.2009.06.042, 2010.

Catling, D. C., M. W. Claire, K. J. Zahnle, R. C. Quinn, B. C. Clark, M. H. Hecht, and S. Kounaves, Atmospheric origins of perchlorate on Mars and in the Atacama, *Journal of Geophysical Research: Planets*, *115*, doi:10.1029/2009JE003425, 2010.

Chapman, M., *The Geology of Mars: Evidence from Earth-Based Analogs*, Cambridge Planetary Science, Cambridge University Press, 2007.

Chevrier, V., D. W. Sears, J. D. Chittenden, L. A. Roe, R. Ulrich, K. Bryson, L. Billingsley, and J. Hanley, Sublimation rate of ice under simulated mars conditions and the effect of layers of mock regolith jsc mars-1, *Geophysical Research Letters*, *34*(2), 2007.

Chevrier, V., D. R. Ostrowski, and D. W. Sears, Experimental study of the sublimation of ice through an unconsolidated clay layer: Implications for the stability of ice on mars and the possible diurnal variations in atmospheric water, *Icarus*, *196*(2), 459–476, 2008.

Chevrier, V., J. Hanley, and T. Altheide, Stability of perchlorate hydrates and their liquid solutions at the phoenix landing site, mars (vol 36, art no 110202, 2009), *Geophysical Research Letters*, *36*, L18,204, doi:10.1029/2009GL040523, 2009.

Chicarro, A., P. Martin, and R. Trautner, The Mars Express mission: an overview, in *Mars Express: the Scientific Payload*, *ESA Special Publication*, vol. 1240, edited by A. Wilson and A. Chicarro, pp. 3–13, 2004.

Christensen, P., et al., Results from the mars global surveyor thermal emission spectrometer, *Science*, *279*(5357), 1692–1698, 1998.

Clancy, R., A. Grossman, M. Wolff, P. James, D. Rudy, Y. Billawala, B. Sandor, S. Lee, and D. Muhleman, Water vapor saturation at low altitudes around mars aphelion: A key to mars climate?, *Icarus*, *122*(1), 36 – 62, doi:http://dx.doi.org/10.1006/icar.1996.0108, 1996.

Clancy, R., M. Wolff, and P. Christensen, Mars aerosol studies with the MGS TES emission phase function observations: Optical depths, particle sizes, and ice cloud types versus latitude and solar longitude, *Journal of Geophysical Research: Planets*, *108*(E9), doi:10.1029/2003JE002058, 2003.

Clapp, M., and R. Miller, Shape effects in the infrared spectrum of ammonia aerosols, *Icarus*, *105*(2), 529 – 536, doi:http://dx.doi.org/10.1006/icar.1993.1146, 1993.

Clapp, M., R. Miller, and D. Worsnop, Frequency-Dependent Optical Constants of Water Ice Obtained Directly from Aerosol Extinction Spectra, *Journal of Physical Chemistry*, *99*(17), 6317–6326, doi:10.1021/j100017a010, 1995.

Colaprete, A., and O. Toon, The radiative effects of Martian water ice clouds on the local atmospheric temperature profile, *Icarus*, *145*(2), 524–532, doi:10.1006/icar.2000.6364, 2000.

Collins, W., et al., Radiative forcing by well-mixed greenhouse gases: Estimates from climate models in the intergovernmental panel on climate change (ipcc) fourth assessment report (ar4), *Journal of Geophysical Research: Atmospheres*, *111*(D14), 2006.

Conrath, B., J. Pearl, M. Smith, W. Maguire, P. Christensen, S. Dason, and M. Kaelberer, Mars Global Surveyor Thermal Emission Spectrometer (TES) observations: Atmospheric temperatures during aerobraking and science phasing, *Journal of Geophysical Research: Planets*, *105*(E4), 9509–9519, doi:10.1029/1999JE001095, 2000.

Curran, R. J., B. J. Conrath, R. A. Hanel, V. G. Kunde, and J. C. Rearl, Mars: Mariner 9 spectroscopic evidence for h2o ice clouds, *Tech. rep.*, NASA Goddard Space Flight Center, 1973.

Curry, J., W. Rossow, D. Randall, and J. Schramm, Overview of Arctic cloud and radiation characteristics, *Journal of Climate*, *9*(8), 1731–1764, doi:10.1175/1520-0442(1996)009<1731:OOACAR>2.0.CO;2, 1996.

Cziczo, D., and J. Abbatt, Infrared observations of the response of NaCl, MgCl2, NH4HSO4, and NH4NO3 aerosols to changes in relative humidity from 298 to 238 K, *Journal of Physical Chemistry A*, *104*(10), 2038–2047, doi:10.1021/jp9931408, 2000.

Cziczo, D., J. Nowak, J. Hu, and J. Abbatt, Infrared spectroscopy of model tropospheric aerosols as a function of relative humidity: Observation of deliquescence and crystallization, *Journal of Geophysical Research: Atmospheres*, *102*(D15), 18,843–18,850, doi:10.1029/97JD01361, 1997.

Cziczo, D. J., S. Garimella, M. Raddatz, K. Hoehler, M. Schnaiter, H. Saathoff, O. Moehler, J. P. D. Abbatt, and L. A. Ladino, Ice nucleation by surrogates of Martian mineral dust: What can we learn about Mars without leaving Earth?, *Journal of Geophysical Research: Planets*, *118*(9), 1945–1954, doi:10.1002/jgre.20155, 2013.

Davila, A. F., et al., Hygroscopic salts and the potential for life on mars, *Astrobiology*, *10*(6), 617–628, 2010.

Farmer, C. B., D. W. Davies, and D. D. Laporte, Mars: Northern summer ice cap–water vapor observations from viking 2, *Science*, *194*(4271), 1339–1341, doi:10.1126/science.194.4271.1339, 1976.

Fletcher, N. H., E. Bowen, P. Squires, et al., *The Physics of Rainclouds*, Cambridge University Press, 2011.

Fortin, T., K. Drdla, L. Iraci, and M. Tolbert, Ice condensation on sulfuric acid tetrahydrate: Implications for polar stratospheric ice clouds, *Atmospheric Chemistry and Physics*, *3*, 987–997, 2003.

Gates, W. L., E. Batten, A. B. Kahle, and A. B. Nelson, A documentation of the mintz-arakawa two-level atmospheric general circulation model, *Tech. rep.*, DTIC Document, 1971.

Glavin, D. P., et al., Evidence for perchlorates and the origin of chlorinated hydrocarbons detected by SAM at the Rocknest aeolian deposit in Gale Crater, *Journal of Geophysical Research: Planets*, *118*(10), 1955–1973, doi:10.1002/jgre.20144, 2013.

Glotch, T., J. Bandfield, M. Wolff, and J. Arnold, Chloride salt deposits on mars Ñ no longer "putative", in *Lunar and Planetary Science Conference*, *Lunar and Planetary Science Conference*, vol. 44, p. 1549, 2013.

Glotch, T. D., J. L. Bandfield, M. J. Wolff, J. A. Arnold, and C. Che, Constraints on the composition and particle size of chloride salt-bearing deposits on mars, *Journal of Geophysical Research: Planets*, 2016.

Glotch, T. D., J. L. Bandfield, L. L. Tornabene, H. B. Jensen, and F. P. Seelos, Distribution and formation of chlorides and phyllosilicates in Terra Sirenum, Mars, *Geophysical Research Letters*, *37*, doi:10.1029/2010GL044557, 2010.

Goetz, W., et al., Indication of drier periods on mars from the chemistry and mineralogy of atmospheric dust, *Nature*, *436*(7047), 62–65, 2005.

Golombek, M. P., Overview of the mars pathfinder mission and assessment of landing site predictions, *Science*, *278*(5344), 1743–1748, doi:10.1126/science.278.5344. 1743, 1997.

Gooding, J. L., Martian dust particles as condensation nuclei: A preliminary assessment of mineralogical factors, *Icarus*, *66*(1), 56–74, doi:10.1016/0019-1035(86)90006-0, 1986.

Gough, R. V., V. F. Chevrier, K. J. Baustian, M. E. Wise, and M. A. Tolbert, Laboratory studies of perchlorate phase transitions: Support for metastable aqueous perchlorate solutions on mars, *Earth and Planetary Science Letters*, *312*(3-4), 371–377, doi: 10.1016/j.epsl.2011.10.026, 2011.

Grotzinger, J. P., et al., Mars science laboratory mission and science investigation, *Space Science Reviews*, *170*(1-4), 5–56, doi:10.1007/s11214-012-9892-2, 2012.

Guildner, L. A., D. P. Johnson, and F. E. Jones, Vapor pressure of water at its triple point, *Tech. rep.*, National Institute of Standards and Technology, 1976.

Haberle, R., et al., General circulation model simulations of the Mars Pathfinder atmospheric structure investigation/meteorology data, *Journal of Geophysical Research: Planets*, *104*(E4), 8957–8974, doi:10.1029/1998JE900040, 1999.

Haberle, R., J. Murphy, and J. Schaeffer, Orbital change experiments with a Mars general circulation model, *Icarus*, *161*(1), 66–89, doi:10.1016/S0019-1035(02)00017-9, 2003.

Haberle, R. M., Estimating the power of Mars' greenhouse effect, *Icarus*, *223*(1), 619–620, doi:10.1016/j.icarus.2012.12.022, 2013.

Haberle, R. M., J. B. Pollack, J. R. Barnes, R. W. Zurek, C. B. Leovy, J. R. Murphy, H. Lee, and J. Schaeffer, Mars atmospheric dynamics as simulated by the nasa ames general circulation model: 1. the zonal-mean circulation, *Journal of Geophysical Research: Planets*, *98*(E2), 3093–3123, 1993.

Haberle, R. M., F. Forget, A. Colaprete, J. Schaeffer, W. V. Boynton, N. J. Kelly, and M. A. Chamberlain, The effect of ground ice on the Martian seasonal CO2 cycle, *Planetary and Space Science*, *56*(2), 251–255, doi:10.1016/j.pss.2007.08.006, 2008.

Hale, B. N., and P. L. M. Plummer, Molecular model for ice clusters in a supersaturated vapor, *The Journal of Chemical Physics*, *61*(10), 4012–4019, doi:http://dx.doi.org/10.1063/1.1681694, 1974.

Hamilton, V. E., H. Y. McSween, and B. Hapke, Mineralogy of martian atmospheric dust inferred from thermal infrared spectra of aerosols, *Journal of Geophysical Research-planets*, *110*(E12), E12,006, doi:10.1029/2005JE002501, 2005.

Hanel, R., et al., Investigation of the martian environment by infrared spectroscopy on mariner 9, *Icarus*, *17*(2), 423–442, 1972.

Harri, A.-M., et al., Pressure observations by the curiosity rover: Initial results, *Journal of Geophysical Research: Planets*, *119*(1), 82–92, doi:10.1002/2013je004423, 2014.

Harrington, J., and P. Olsson, A method for the parameterization of cloud optical properties in bulk and bin microphysical models. Implications for arctic cloudy boundary layers, *Atmospheric Research*, *57*(1), 51–80, doi:10.1016/S0169-8095(00)00068-5, 2001.

Harrington, J., T. Reisin, W. Cotton, and S. Kreidenweis, Cloud resolving simulations of Arctic stratus - Part II: Transition-season clouds, *Atmospheric Research*, *51*(1), 45–75, doi:10.1016/S0169-8095(98)00098-2, 1999.

Hartmann, W. K., and G. Neukum, Cratering chronology and the evolution of mars, in *Space Sciences Series of ISSI*, pp. 165–194, Springer Netherlands, 2001.

Heavens, N., D. McCleese, M. Richardson, D. Kass, A. Kleinböhl, and J. Schofield, Structure and dynamics of the martian lower and middle atmosphere as observed by the mars climate sounder: 2. implications of the thermal structure and aerosol distributions for the mean meridional circulation, *Journal of Geophysical Research: Planets*, *116*(E1), 2011.

Heavens, N. G., et al., Water ice clouds over the Martian tropics during northern summer, *Geophysical Research Letters*, *37*, doi:10.1029/2010GL044610, 2010.

Hecht, M. H., et al., Detection of perchlorate and the soluble chemistry of martian soil at the phoenix lander site, *Science*, *325*(5936), 64–67, doi:10.1126/science.1172466, 2009.

Hourdin, F., P. L. Van, F. Forget, and O. Talagrand, Meteorological variability and the annual surface pressure cycle on mars, *Journal of the Atmospheric Sciences*, *50*(21), 3625–3640, doi:10.1175/1520-0469(1993)050<3625:mvatas>2.0.co;2, 1993.

Iraci, L. T., B. D. Phebus, B. M. Stone, and A. Colaprete, Water ice cloud formation on Mars is more difficult than presumed: Laboratory studies of ice nucleation on surrogate materials, *Icarus*, *210*(2), 985–991, doi:10.1016/j.icarus.2010.07.020, 2010.

Iwasaki, K., Y. Saito, and T. Akabane, Behavior of the martian north polar cap, 1975–1978, *J. Geophys. Res.*, *84*(B14), 8311, doi:10.1029/jb084ib14p08311, 1979.

Jakosky, B. M., and M. H. Carr, Possible precipitation of ice at low latitudes of mars during periods of high obliquity, *Nature*, *315*(6020), 559–561, 1985.

Jakosky, B. M., et al., The mars atmosphere and volatile evolution (MAVEN) mission, *Space Science Reviews*, *195*(1-4), 3–48, doi:10.1007/s11214-015-0139-x, 2015.

James, P. B., R. Clancy, S. W. Lee, L. J. Martin, R. B. Singer, E. Smith, R. A. Kahn, and R. W. Zurek, Monitoring mars with the hubble space telescope: 1990-1991 observations, *Icarus*, *109*(1), 79–101, doi:10.1006/icar.1994.1078, 1994.

Jensen, H. B., and T. D. Glotch, Investigation of the near-infrared spectral character of putative martian chloride deposits, *Journal of Geophysical Research-planets*, *116*, E00J03, doi:10.1029/2011JE003887, 2011.

Johnson, D., The standard free energies of solution of anhydrous salts in water, *J. Chem. Educ*, *45*(4), 236, 1968.

Kahre, M., J. Hollingsworth, R. Haberle, and R. Wilson, Coupling the mars dust and water cycles: The importance of radiative-dynamic feedbacks during northern hemisphere summer, *Icarus*, *260*, 477 – 480, doi:http://dx.doi.org/10.1016/j.icarus.2014.07.017, 2015.

Kahre, M., J. Murphy, and R. Haberle, Modeling the Martian dust cycle and surface dust reservoirs with the NASA Ames general circulation model, *Journal of Geophysical Research: Planets*, *111*(E6), doi:10.1029/2005JE002588, 2006.

Kahre, M. A., J. L. Hollingsworth, R. M. Haberle, and J. R. Murphy, Investigations of the variability of dust particle sizes in the martian atmosphere using the NASA Ames General Circulation Model, *Icarus*, *195*(2), 576–597, doi:{10.1016/j.icarus.2008.01.023}, 2008.

Kieffer, H. H., and T. N. Titus, Tes mapping of mars' north seasonal cap, *Icarus*, *154*(1), 162–180, 2001.

Kieffer, H. H., S. C. Chase, T. Z. Martin, E. D. Miner, and F. D. Palluconi, Martian north pole summer temperatures: Dirty water ice, *Science*, *194*(4271), 1341–1344, doi:10.1126/science.194.4271.1341, 1976.

Lacis, A. A., and V. Oinas, A description of the correlated k distribution method for modeling nongray gaseous absorption, thermal emission, and multiple scattering in vertically inhomogeneous atmospheres, *Journal of Geophysical Research: Atmospheres*, *96*(D5), 9027–9063, 1991.

Ladino, L. A., and J. P. D. Abbatt, Laboratory investigation of martian water ice cloud formation using dust aerosol stimulants, *Journal of Geophysical Research-planets*, *118*(1), doi:10.1029/2012JE004238, 2013.

Laskar, J., B. Levrard, and J. F. Mustard, Orbital forcing of the martian polar layered deposits, *Nature*, *419*(6905), 375–377, 2002.

Lemmon, M., et al., Atmospheric imaging results from the mars exploration rovers: Spirit and opportunity, *Science*, *306*(5702), 1753–1756, 2004.

Leovy, C. B., J. E. Tillman, and J. Barnes, *Interannual Variability of Martian Weather*, 1985.

Leshin, L. A., et al., Volatile, Isotope, and Organic Analysis of Martian Fines with the Mars Curiosity Rover, *Science*, *341*(6153), doi:10.1126/science.1238937, 2013.

Lu, P.-D., T. He, and Y.-H. Zhang, Relative humidity anneal effect on hygroscopicity of aerosol particles studied by rapid-scan FTIR-ATR spectroscopy, *Geophysical Research Letters*, *35*(20), doi:10.1029/2008GL035302, 2008.

Määttänen, A., K. Pérot, F. Montmessin, and A. Hauchecorne, *Mesospheric Clouds on Mars and on Earth*, pp. 393–413, doi:10.2458/azu_uapress_9780816530595-ch16, 2013.

Madeleine, J. B., F. Forget, E. Millour, T. Navarro, and A. Spiga, The influence of radiatively active water ice clouds on the Martian climate, *Geophysical Research Letters*, *39*, doi:10.1029/2012GL053564, 2012.

Mahaffy, P. R., et al., Abundance and isotopic composition of gases in the martian atmosphere from the curiosity rover, *Science*, *341*(6143), 263–266, 2013.

Maltagliati, L., F. Montmessin, A. Fedorova, O. Korablev, F. Forget, and J. L. Bertaux, Evidence of Water Vapor in Excess of Saturation in the Atmosphere of Mars, *Science*, *333*(6051), 1868–1871, doi:10.1126/science.1207957, 2011.

Martin-Torres, F. J., et al., Transient liquid water and water activity at gale crater on mars, *Nature Geosci*, *8*(5), 357–361, 2015.

Mastrapa, R. M., S. A. Sandford, T. L. Roush, D. P. Cruikshank, and C. M. D. Ore, Optical Constants of Amorphous and Crystaline H2O-Ice: 2.5-22 mu m (4000-455 cm(-1)) Optical Constants OF H2O-ICE, *Astrophysical Journal*, *701*(2), 1347–1356, doi:10.1088/0004-637X/701/2/1347, 2009.

McCleese, D. J., et al., Structure and dynamics of the Martian lower and middle atmosphere as observed by the Mars Climate Sounder: Seasonal variations in zonal mean temperature, dust, and water ice aerosols, *Journal of Geophysical Research: Planets*, *115*, doi:10.1029/2010JE003677, 2010.

Milkovich, S. M., and J. W. Head, North polar cap of mars: Polar layered deposit characterization and identification of a fundamental climate signal, *Journal of Geophysical Research: Planets*, *110*(E1), 2005.

Montmessin, F., P. Rannou, and M. Cabane, New insights into martian dust distribution and water-ice cloud microphysics, *J. Geophys. Res.*, *107*(E6), 5037–, 2002.

Montmessin, F., F. Forget, P. Rannou, M. Cabane, and R. M. Haberle, Origin and role of water ice clouds in the martian water cycle as inferred from a general circulation model, *J. Geophys. Res.*, *109*(E10), E10,004–, 2004.

Murphy, D., and T. Koop, Review of the vapour pressures of ice and supercooled water for atmospheric applications, *Quarterly Journal of the Royal Meteorological Society*, *131*(608), 1539–1565, 2005.

Navarro, T., J.-B. Madeleine, F. Forget, A. Spiga, E. Millour, F. Montmessin, and A. Määttänen, Global climate modeling of the martian water cycle with improved microphysics and radiatively active water ice clouds, *Journal of Geophysical Research: Planets*, *119*(7), 1479–1495, 2014.

Nelli, S. M., J. R. Murphy, W. C. Feldman, and J. R. Schaeffer, Characterization of the nighttime low-latitude water ice deposits in the NASA Ames Mars General Circulation Model 2.1 under present-day atmospheric conditions, *Journal of Geophysical Research: Planets*, *114*, doi:10.1029/2008JE003289, 2009.

Nelli, S. M., N. O. Renno, J. R. Murphy, W. C. Feldman, and S. W. Bougher, Simulations of atmospheric phenomena at the Phoenix landing site with the Ames General Circulation Model, *Journal of Geophysical Research: Planets*, *115*, doi:10.1029/2010JE003568, 2010.

Ojha, L., M. B. Wilhelm, S. L. Murchie, A. S. McEwen, J. J. Wray, J. Hanley, M. Masse, and M. Chojnacki, Spectral evidence for hydrated salts in recurring slope lineae on mars (vol 8, pg 829, 2015), *Nature Geoscience*, *8*(11), 2015.

Osterloo, M. M., V. E. Hamilton, J. L. Bandfield, T. D. Glotch, A. M. Baldridge, P. R. Christensen, L. L. Tornabene, and F. S. Anderson, Chloride-bearing materials in the southern highlands of mars, *Science*, *319*(5870), 1651–1654, doi:10.1126/science.1150690, 2008.

Osterloo, M. M., F. S. Anderson, V. E. Hamilton, and B. M. Hynek, Geologic context of proposed chloride-bearing materials on mars, *Journal of Geophysical Research-planets*, *115*, E10,012, doi:10.1029/2010JE003613, 2010.

Owen, T., K. Biemann, D. R. Rushneck, J. E. Biller, D. W. Howarth, and A. L. Lafleur, The composition of the atmosphere at the surface of mars, *Journal of Geophysical Research*, *82*(28), 4635–4639, doi:10.1029/js082i028p04635, 1977.

Pearl, J. C., M. D. Smith, B. J. Conrath, J. L. Bandfield, and P. R. Christensen, Observations of martian ice clouds by the mars global surveyor thermal emission spectrometer: the first martian year, *Journal of Geophysical Research: Planets*, *106*(E6), 12,325–12,338, 2001.

Peters, G. H., W. Abbey, G. H. Bearman, G. S. Mungas, J. A. Smith, R. C. Anderson, S. Douglas, and L. W. Beegle, Mojave mars simulant - characterization of a new geologic mars analog, *Icarus*, *197*(2), 470–479, doi:10.1016/j.icarus.2008.05.004, 2008.

Phebus, B. D., A. V. Johnson, B. Mar, B. M. Stone, A. Colaprete, and L. T. Iraci, Water ice nucleation characteristics of JSC Mars-1 regolith simulant under simulated Martian atmospheric conditions, *Journal of Geophysical Research: Planets*, *116*, doi:10.1029/2010JE003699, 2011.

Pilorget, C., and F. Forget, Formation of gullies on mars by debris flows triggered by CO2 sublimation, *Nature Geoscience*, *9*(1), 65–69, doi:10.1038/ngeo2619, 2015.

Pommerol, A., B. Schmitt, P. Beck, and O. Brissaud, Water sorption on martian regolith analogs: Thermodynamics and near-infrared reflectance spectroscopy, *Icarus*, *204*(1), 114–136, doi:10.1016/j.icarus.2009.06.013, 2009.

Pruppacher, H. R., and J. D. Klett, *Microphysics of clouds and precipitation*, Kluwer Academic, Dordrecht [etc., bibliogr. : p. 874-934. Index, 1997.

Sagan, C., and P. Fox, The canals of mars: An assessment after mariner 9, *Icarus*, *25*(4), 602–612, doi:10.1016/0019-1035(75)90042-1, 1975.

Saunders, R. S., et al., 2001 mars odyssey mission summary, in *2001 Mars Odyssey*, pp. 1–36, Springer Science, 2004.

Schorghofer, N., and O. Aharonson, Stability and exchange of subsurface ice on Mars, *Journal of Geophysical Research: Planets*, *110*(E5), doi:10.1029/2004JE002350, 2005.

Sednev, I., S. Menon, and G. McFarquhar, Simulating mixed-phase Arctic stratus clouds: sensitivity to ice initiation mechanisms, *Atmospheric Chemistry and Physics*, *9*(14), 4747–4773, 2009.

Siegler, M., O. Aharonson, E. Carey, M. Choukroun, T. Hudson, N. Schorghofer, and S. Xu, Measurements of thermal properties of icy Mars regolith analogs, *Journal of Geophysical Research: Planets*, *117*, doi:10.1029/2011JE003938, 2012.

Smith, D. E., Seasonal variations of snow depth on mars, *Science*, *294*(5549), 2141–2146, doi:10.1126/science.1066556, 2001.

Smith, M., Interannual variability in TES atmospheric observations of Mars during 1999-2003, *Icarus*, *167*(1), 148–165, doi:10.1016/j.icarus.2003.09.010, 2004.

Smith, M. D., The annual cycle of water vapor on mars as observed by the thermal emission spectrometer, *J. Geophys. Res.*, *107*(E11), 5115–, 2002.

Smith, M. D., Spacecraft observations of the Martian atmosphere, *Annual Review of Earth and Planetary Sciences*, *36*, 191–219, doi:10.1146/annurev.earth.36.031207.124335, 2008.

Smith, M. D., THEMIS observations of Mars aerosol optical depth from 2002-2008, *Icarus*, *202*(2), 444–452, doi:10.1016/j.icarus.2009.03.027, 2009.

Smith, M. D., M. J. Wolff, R. T. Clancy, A. Kleinboehl, and S. L. Murchie, Vertical distribution of dust and water ice aerosols from CRISM limb-geometry observations, *Journal of Geophysical Research: Planets*, *118*(2), 321–334, doi:10.1002/jgre.20047, 2013.

Soffen, G. A., and A. T. Young, The viking missions to mars, *Icarus*, *16*(1), 1–16, doi:10.1016/0019-1035(72)90133-9, 1972.

Squyres, S. W., et al., Overview of the opportunity mars exploration rover mission to meridiani planum: Eagle crater to purgatory ripple, *Journal of Geophysical Research: Planets*, *111*(E12), n/a–n/a, doi:10.1029/2006je002771, 2006.

Steinbacher, R. H., Mariner 9 Mission, in *Bulletin of the American Astronomical Society*, vol. 4, p. 356, 1972.

Stillman, D. E., and R. E. Grimm, Dielectric signatures of adsorbed and salty liquid water at the Phoenix landing site, Mars, *Journal of Geophysical Research: Planets*, *116*, doi:10.1029/2011JE003838, 2011.

Tang, I., and H. Munkelwitz, Composition and temperature dependence of the deliquescence properties of hygroscopic aerosols, *Atmospheric Environment. Part A. General Topics*, *27*(4), 467–473, doi:{10.1016/0960-1686(93)90204-C}, 1993.

Tang, I., and H. Munkelwitz, Aerosol phase transformation and growth in the atmosphere, *Journal of Applied Meteorology*, *33*(7), 791–796, 1994.

Taylor, J., *Introduction to Error Analysis, the Study of Uncertainties in Physical Measurements, 2nd Edition*, University Science Books, 1997.

Titus, T., H. Kieffer, and P. Christensen, Exposed water ice discovered near the south pole of Mars, *Science*, *299*(5609), 1048–1051, doi:10.1126/science.1080497, 2003.

Toner, J., D. Catling, and B. Light, The formation of supercooled brines, viscous liquids, and low-temperature perchlorate glasses in aqueous solutions relevant to mars, *Icarus*, *233*, 36–47, 2014.

Toon, O. B., and T. Ackerman, Algorithms for the calculation of scattering by stratified spheres, *Applied Optics*, *20*(20), 3657–3660, 1981.

Toon, O. B., M. A. Tolbert, B. G. Koehler, A. M. Middlebrook, and J. Jordan, Infrared optical constants of h2o ice, amorphous nitric acid solutions, and nitric acid hydrates, *Journal of Geophysical Research*, *99*, 25,631, 1994.

Trainer, M. G., O. B. Toon, and M. A. Tolbert, Measurements of Depositional Ice Nucleation on Insoluble Substrates at Low Temperatures: Implications for Earth and Mars, *Journal of Physical Chemistry C*, *113*(6), 2036–2040, doi:10.1021/jp805140p, 2009.

Wang, H., and A. Ingersoll, Martian clouds observed by Mars Global Surveyor Mars Orbiter Camera, *Journal of Geophysical Research: Planets*, *107*(E10), doi:10.1029/2001JE001815, 2002.

Warren, S., Optical constants of ice from the ultraviolet to the microwave, *Applied Optics*, *23*(8), 1206–1225, 1984.

Warren, S. G., and R. E. Brandt, Optical constants of ice from the ultraviolet to the microwave: A revised compilation, *Journal of Geophysical Research-atmospheres*, *113*(D14), D14,220, doi:10.1029/2007JD009744, 2008.

Whiteway, J. A., et al., Mars Water-Ice Clouds and Precipitation, *Science*, *325*(5936), 68–70, doi:10.1126/science.1172344, 2009.

Wilson, R. J., S. R. Lewis, L. Montabone, and M. D. Smith, Influence of water ice clouds on martian tropical atmospheric temperatures, *Geophysical Research Letters*, *35*(7), 2008.

Wolff, M. J., M. D. Smith, R. T. Clancy, R. Arvidson, M. Kahre, F. Seelos, S. Murchie, and H. Savijärvi, Wavelength dependence of dust aerosol single scattering albedo as observed by the compact reconnaissance imaging spectrometer, *J. Geophys. Res.*, *114*(E2), n/a–n/a, 2009.

Zent, A., and R. Quinn, Measurement of H2O adsorption under Mars-like conditions: Effects of adsorbent heterogeneity, *Journal of Geophysical Research: Planets*, *102*(E4), 9085–9095, doi:10.1029/96JE03420, 1997.

Zent, A. P., M. H. Hecht, D. R. Cobos, S. E. Wood, T. L. Hudson, S. M. Milkovich, L. P. DeFlores, and M. T. Mellon, Initial results from the thermal and electrical conductivity probe (TECP) on Phoenix, *Journal of Geophysical Research: Planets*, *115*, doi:10.1029/2009JE003420, 2010.

Zhao, L., Y. Zhang, L. Wang, Y. Hu, and F. Ding, FTIR spectroscopic investigations of supersaturated NaClO4 aerosols, *Physical Chemistry Chemical Physics*, *7*(14), 2723–2730, doi:10.1039/b505605e, 2005.

Zurek, R. W., and S. E. Smrekar, An overview of the mars reconnaissance orbiter (MRO) science mission, *Journal of Geophysical Research*, *112*(E5), doi:10.1029/2006je002701, 2007.